MECHANICS AND DESIGN OF POLYMERIC METAMATERIAL STRUCTURES FOR SHOCK ABSORPTION APPLICATIONS

A Dissertation

Submitted to the Faculty

of

Purdue University

by

Amin Joodaky

In Partial Fulfillment of the

Requirements for the Degree

of

Doctor of Philosophy

August 2020

Purdue University

West Lafayette, Indiana

THE PURDUE UNIVERSITY GRADUATE SCHOOL
STATEMENT OF DISSERTATION APPROVAL

Dr. James M. Gibert, Chair

School of Mechanical Engineering

Dr. Jeffrey F. Rhoads

School of Mechanical Engineering

Dr. Anil K. Bajaj

School of Mechanical Engineering

Dr. Patricia Davies

School of Mechanical Engineering

Dr. Tyler Tallman

School of Aeronautics and Astronautics

Approved by:

Nicole Key

Head of the School Graduate Program

To my parents and siblings

ACKNOWLEDGMENTS

There are many people I should thank from my family and friends to school teachers and advisors. I apologize that I cannot mention them all here. First of all, I sincerely thank my advisor Dr. James Gibert for his great technical directions during these years. He has provided excellent mentorship for both my professional and personal life. I appreciate the friendly, inclusive, diverse, and professional environment he provides for his students.

I highly appreciate the insights and guidance provided by my PhD advisory committee: Dr. Patricia Davies, Dr. Jeff Rhoads, Dr. Anil Bajaj, and Dr. Tyler Tallman. I also would like to thank the instructors of the courses I took at Purdue, in addition to class content, I experienced practical effective methods of teaching.

I would like to thank Dr. Gregory Batt from Clemson University for his collaboration and support on my research. He is also a great leader and friend.

I thank the staff and colleagues at Herrick Labs and the School of Mechanical Engineering at Purdue. I thank my lab mates in ADAMS lab especially Hongcheng Tao.

I am grateful for a Teaching and Learning certificate I received from the School of Engineering Education at Purdue. Thanks to Dr. Audeen Fentiman, Dr. Ruth Streveler, Dr. Karl Smith, and Dr. Kerrie Douglas for their friendly cooperative active learning classes and for developing this certificate.

I appreciate the financial supports from ISTA (International Safe Transit Association) and Purdue Research Foundation. I thank ISTA Forum of TransPack TempPack, 2019, Denver, that invited me as a speaker to share my challenges in multi axis vibrations of packages. I learned a lot from the presenters and was able to network with representatives from many packaging companies and institutes.

I thank all of my friends who have been supportive and sharing fun moments with me to facilitate this journey. I thank my musical instruments especially my Piano. I enjoyed playing basketball at COREC.

I wish to express my deepest gratitude to my parents and siblings who have been my best fans and supporters for my whole life. I can never thank them enough for their love, sacrifice, and devotion.

TABLE OF CONTENTS

Page

LIST OF TABLES

LIST OF FIGURES

Figure Page

Figure Page

Figure Page

ABBREVIATIONS

ASTM	American Society for Testing and Materials
SRS	Shock Response Spectrum
DBC	Damage Boundary Curve
FEM	Finite Element Method
EPS	Expanded Polystyrene
QZM	Quasi-Zero Modulus
QZS	Quasi-Zero Stiffness
PLA	Polylactic Acid
TPU	Thermoplastic Polyurethane
FFF	Fused Filament Fabrication

ABSTRACT

Joodaky, Amin Ph.D., Purdue University, August 2020. Mechanics and Design of Polymeric Metamaterial Structures for Shock Absorption Applications. Major Professor: James Gibert, School of Mechanical Engineering.

This body of work examines analytical and numerical models to simulate the response of structures in shock absorption applications. Specifically, the work examines the prediction of cushion curves of polymer foams, and a topological examination of a χ shape unit cell found in architected mechanical elastomeric metamaterials. The χ unit cell exhibits the same effective stress-strain relationship as a closed cell polymer foam. Polymer foams are commonly used in the protective packaging of fragile products. Cushion curves are used within the packaging industry to characterize a foam's impact performance. These curves are two-dimensional representations of the deceleration of an impacting mass versus static stress. The main drawback with cushion curves is that they are currently generated from an exhaustive set of experimental test data. This work examines modeling the shock response using a continuous rod approximation with a given impact velocity in order to generate cushion curves without the need of extensive testing. In examining the χ unit cell, this work focuses on the effects of topological changes on constitutive behavior and shock absorbing performance. Particular emphasis is placed on developing models to predict the onset of regions of quasi-zero-modulus (QZM), the length of the QZM region and the cushion curve produced by impacting the unit cell. The unit cell's topology is reduced to examining a characteristic angle, defining the internal geometry with the cell, and examining the effects of changing this angle. However, the characteristic angle cannot be increased without tradeoffs; the cell's effective constitutive behavior evolves from long regions to shortened regions of quasi-zero modulus. Finally, this work shows that the basic χ unit cell can be tessellated to produce a nearly equivalent force deflection

relationship in two directions. The analysis and results in this work can be viewed as new framework in analyzing programmable elastomeric metamaterials that exhibit this type of nonlinear behavior for shock absorption.

1. INTRODUCTION

Mechanical shock resulting from phenomenon such as impact, drop, or earthquake are a sudden (a transient physical excitation) acceleration or deceleration in a structure's motion or deformation [1]. While beneficial to applications such as energy harvesting, shock phenomena is mostly a hazard to structures. Structures that experience sudden or drastic increase in loading are designed to be shock resistant. An example of this shock resistant are braced frames that are designed to enhance the resistance of building structures against seismic earthquakes [2]. However, designs for fortifying structures face limitations. Along with strengthening structures, shock absorbers, that are placed between the source of loading and a structure, are designed to reduce the transmitted shock energy to the structure. For example, researchers have long studied structures and materials for shoe soles to attenuate the impact shock transmitted to a person in athletic activities such as running and jumping to lower biomechanical human body damages [3]. Over the years, several tests and metrics have been developed to measure shock absorption capacity of a structure in impact events including cushion curves, efficiency and ideality, shock response spectrum, damage boundary curve, and other alternative methods.

From handling to transportation, packaged products are susceptible to damage due to impacts [4]. Mainly made of polymer, closed or open cell foams have been applied in packaging design to protect products from impacts [5, 6]. These foams are also applied in the auto industry for car seat and helmet designs for protection and comfort applications [7,8]. Mechanical metamaterials are also used as shock absorbing structures. These materials and structures whose properties are not commonly found in nature [9], use complex internal structure to effect material behavior. Researchers have taken advantage of uncanny properties of metamaterials in many areas such as electromagnetics, optics, and acoustics [10]. Recently, metamaterials are designed and studied for shock absorption applications [11].

The present work has two interwoven focuses: 1) providing mechanics based prediction of shock pulses including nonlinear dynamics and higher-order modal interactions, to predict cushion curves for polymer foams, and 2) proposing, manufacturing, and parameter tuning of a χ shape architected structure for enhancing ideality which is a shock absorption metric. The analytical and numerical models for both works are validated with experimental results. In this chapter, a background and literature review is provided for 1) shock absorption metrics, and 2) the shock absorption and current mechanics models of cellular foams and metamaterials.

1.1 Shock Absorption Metrics

The function of a protective foam or a cushion is two fold: 1) absorb maximum energy during impact and 2) transmit a force or acceleration to the object that it is protecting that is below a critical acceleration (g) level that would result in damage. Over the years, several tests and metrics have been developed to characterize the shock and vibration transmissibility of cushioning systems. The next section provides a brief overview of these procedures and/or quantities.

1.1.1 Shock Spectrum

The shock response spectrum (SRS) is a graphical representation of a transient acceleration pulses' potential to damage a structure. SRS was designed to characterize shock events on general linear systems. However, later it was applied to systems that exhibit nonlinearities approximated as piecewise functions [12]. The spectrum was first conceived by Dr. Maurice Biot in his 1932 PhD thesis [13]. He defined the SRS as the maximum acceleration response from a set of single-degree-of-freedom oscillators each with a modal frequency over a predetermined range. It can be visualized as an array of single-degree-of-freedom oscillators attached to a rigid base. In its original conception, Biot assumed that the motion of the oscillators did not affect the base. A transient shock is applied to base and the maximum acceleration response of each oscillator is recorded. The shock spectrum is constructed by plotting the maximum acceleration response of the array of oscillators with their corresponding modal frequency.

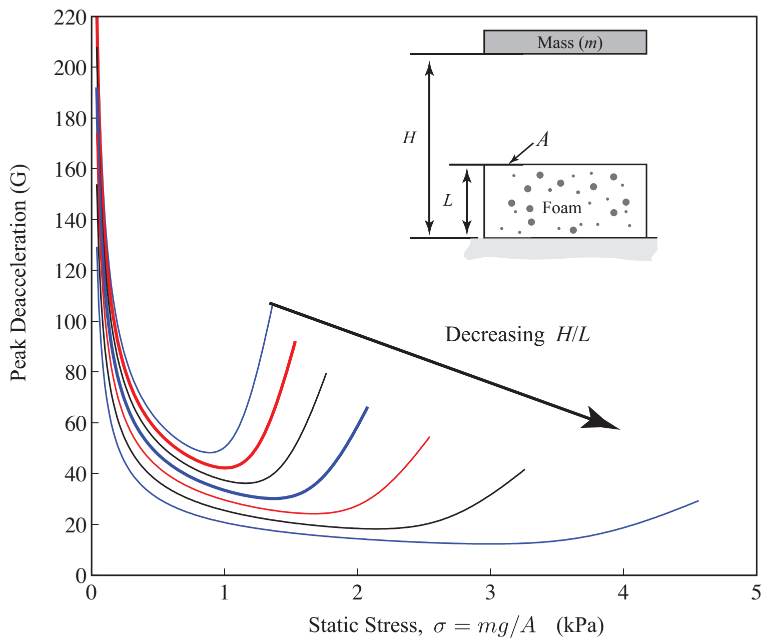

Figure 1.1. Cushion curves for a hypothetical foam at various drop heights.

1.1.2 Cushion Curve

Cushion curves are determined using the standard ASTM D1596 [14]. In this test a platten of mass, m, is dropped from a drop height, h, on a sample of a cushioning material of area A. The main aim is to determine the effect of the static load and the drop height on the level of shock to which the mass is subjected. Various static loads σ_s can be obtained by varying either the mass m or contact area A. The static load is defined as $\sigma_s = mg/A$. The shock-absorbing characteristics of the material is represented as a family of cushion curves, Fig. 1.1. Each individual curve is composed of the peak accelerations during impacts for a range of static loads for a given drop height. The size and material composition of the foam used for a given application is determined by finding the static stress that minimizes the rebound shock pulse within a predetermined bound. In order to construct a family of curves, it can require over 10,500 drops and 175 hours for a single material [15].

1.1.3 Damage Boundary Curve

Damage boundary curves (DBC) like cushion curves are determined using ASTM 3332 [16]. Damage boundary and cushion curves differ significantly in implementation and in the information that they convey. Specifically, the drop test determines the combinations of peak deceleration and shock duration that will produce damage in the product. While cushion curves are based on a controlled drop, damage boundary curves are generated from a vertical shock table that drops the package from a known height. The damage boundary curve has the underlying assumption the packaged product can be modeled as a linear spring-mass-damper. Typically, the shock table is used to excite the packaged product to provide a step change in velocity or acceleration depending on the duration and magnitude of the shock event. Step changes in velocity and acceleration at the onset of damage are used to draw a boundary curve.

1.1.4 Efficiency and Ideality

Milton and Gruenham [17] examined foams whose constitutive relationship is strain rate independent or is minimally dependent on strain rate. They proposed two measures of shock absorption that can be determined from a quasi-static compression test, ideality (I) and efficiency (E). These metrics are based on the assumption that the ideal foam transmits a constant force when compressed through its thickness. The two measures can be formally written as

$$I = \int_0^{\epsilon_m} \frac{\sigma}{\sigma_m \epsilon_m} d\epsilon \quad \text{and} \quad E = \int_0^{\epsilon_m} \frac{\sigma}{\sigma_m} d\epsilon, \tag{1.1}$$

where ϵ_m is the maximum strain the foam is compressed, and σ_m is the corresponding maximum stress. The two measures differ by a factor of $\frac{1}{\epsilon_m}$. Each quantity depends on the maximum strain rate at impact and can vary when mapped to the quasi-static stress-strain curve. Both metrics are ratios of energy, I is the ratio of energy absorbed between a real foam to an ideal foam at the same level of strain and transmitting constant force, E is the ratio representing the efficiency of energy absorption of the compressed foam to an ideal foam that is fully compressed that transmits an equivalent constant force/stress to the product.

It is useful to review the constitutive behavior of a typical polymer foam to better understand the two metrics. The constitutive behavior characterized by three regions: at low strains from 0.0 to ≈ 0.06 a linear or slightly parabolic elastic region, from 0.06 to 0.6, 2) a region of deformation at near constant stress, and 3) an approximately linear response with a high tangent modulus for strains greater than 0.7, see Fig. 1.2. The material behavior in the first region is controlled by cell wall bending and cell face stretching. At the apex of this region, the collapse of cell walls is due to elastic buckling. In the second region, cell wall buckling occurs causing large deflection due to small increases in force. The third region occurs past the plateau and is known as the densification region; the foam's cell walls further collapse on themselves and contact each other when compressed. Ideality is maximized for strains and stresses in the second region of the constitutive behavior, in regions where the stress is nearly constant over a range of strains. Efficiency is maximized in the overlap between the second and third regions, where there is a transition from nearly constant stress to a rapid change in stress over a finite range of strain.

1.1.5 Alternative Metrics

Suhir [18] for designing shock absorbing systems for microelectronic devices theorized that the ideal shock absorber is a device or material that provides a constant declaration below the critical value in which product damage could occur. In addi-

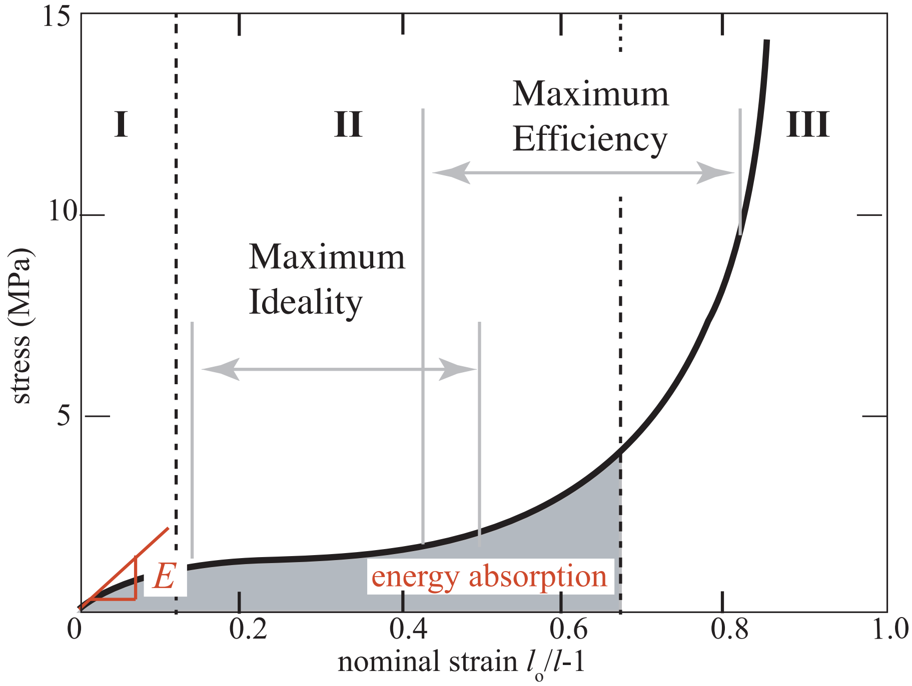

Figure 1.2. Stress-strain curves for a hypothetical foam showing regions of maximum ideality and efficiency. The grey area under the curve indicates the energy absorbed by the foam at the indicated strain.

tion, they added the constraint that this deceleration must occur within a minimum stopping distance during the entire time of breaking. Furthermore, they formulated a metric to calculate the effectiveness of a shock absorber as the product of the maximum acceleration and the maximum compression distance

$$R = x_{max}\ddot{x}_{max}. \tag{1.2}$$

Assuming the acceleration is constant, the metric becomes $R = -gH$, where g is the acceleration due to gravity and H is the drop height, is the upper limit on performance. Comparing Suhir work to Milton and Gruenham [17], one realizes that the metric captures both ideality and efficiency. The metric measures ideality by penalizing non-constant acceleration; and it captures efficiency by requiring a minimal stopping distance. The minimal stopping distance is directly correlated to a foam absorbing maximum energy at a given maximum strain level.

1.2 Foams and Architected Structures for Shock Absorption

In this section, cellular foams and metamaterials are briefly introduced. The following paragraphs provide a survey of literature on the mechanics based models of foams and the use of architected metamaterials for shock absorption.

1.2.1 Foam Structure

This discussion of the structure of foam is based on descriptions found in Gibson and Ashby [5]. "A cellular solid is one made up of an interconnected network of solid struts or plates which form the edges and faces of cells. The cells are polyhedra which pack in three dimensions to fill space; we call such three-dimensional cellular materials *foams*. If the solid of which the foam is made is contained in the cell edges only (so that the cells connect through open faces), the foam is said to be open-celled. If the faces are solid too, so that each cell is sealed off from its neighbors, it is said to be closed-celled; and of course, some of foams are partly open and partly closed".

Foam is commonly used packaging material for a package to be effective it must absorb the energy of impacts or of forces generated by deceleration, without subjecting the contents to damaging stresses. It should be noted that foams are particularly well suited for this task. The strength of a foam can be adjusted over a wide range through changes in its relative density. Furthermore, foams can experience large compressive strains on the order of 0.7 or more, at almost constant stress. This has the consequence that large amounts of energy can be absorbed by the foam without generating high stresses.

The deformation behavior of elastomeric, elastic-plastic, and elastic-brittle foams are shown as compressive stress-strain curve in Fig. 1.3. It was noted earlier that each stress-strain curve of foams has three distinct regions. While the previous discussion applied to polymer foams the regions are found in other types of foams. The first region is linear elastic and it is controlled by cell wall bending in open cell foams and by cell face stretching if the foam is composed of closed walls. The region has a Young's modulus, E^*, i.e., the initial slope of the stress-strain curve. When loading is compressive the second region depends on the foam: 1) a plateau is associated with collapse of the cells by elastic buckling in elastomeric foam, 2) plastic hinges occur in a foam which yields (such as a metal); and 3) brittle crushing occurs in a brittle foam (such as a ceramic). In the third region the cells have almost completely collapsed. The opposing cell walls touch, and further strain compresses the solid portions of the cell. This compression results in densification, the final region of rapidly increasing stress.

1.2.2 Literature Review of Foams and Cushion Curves

The previous discussion was focused on the quasi-static compressive behavior of a foam. This section focuses on the dynamic behavior due to impacts. The shock attenuation properties of a cushion material are experimentally determined using ASTM D1596 *Standard Test Method for Shocking Absorbing Characteristics of Package Cushioning Materials* [14]. In the test, a mass M is dropped from a height H on a sample cushioning material of area A. The goal of the test is to study the effect of the static stress $\sigma_s = Mg/A$ and drop height on the peak deacceleration of the mass, as the foam is compressed. The results are represented as cushion curves that plot peak acceleration during impact versus static stress.

Mathematical models of impact response of packaging systems originated in the 1990's. Initially, the mathematical predictions were based on an energy balance during impact. A popular approach was a forced vibration system with foam as a nonlinear spring and damping, and static weight of dropped mass as the force [19, 20]. Based on a dynamic stress-strain curve method, Burgess [21, 22] consolidated all cushion curves into a single relationship. The method is simple and takes only one data of a

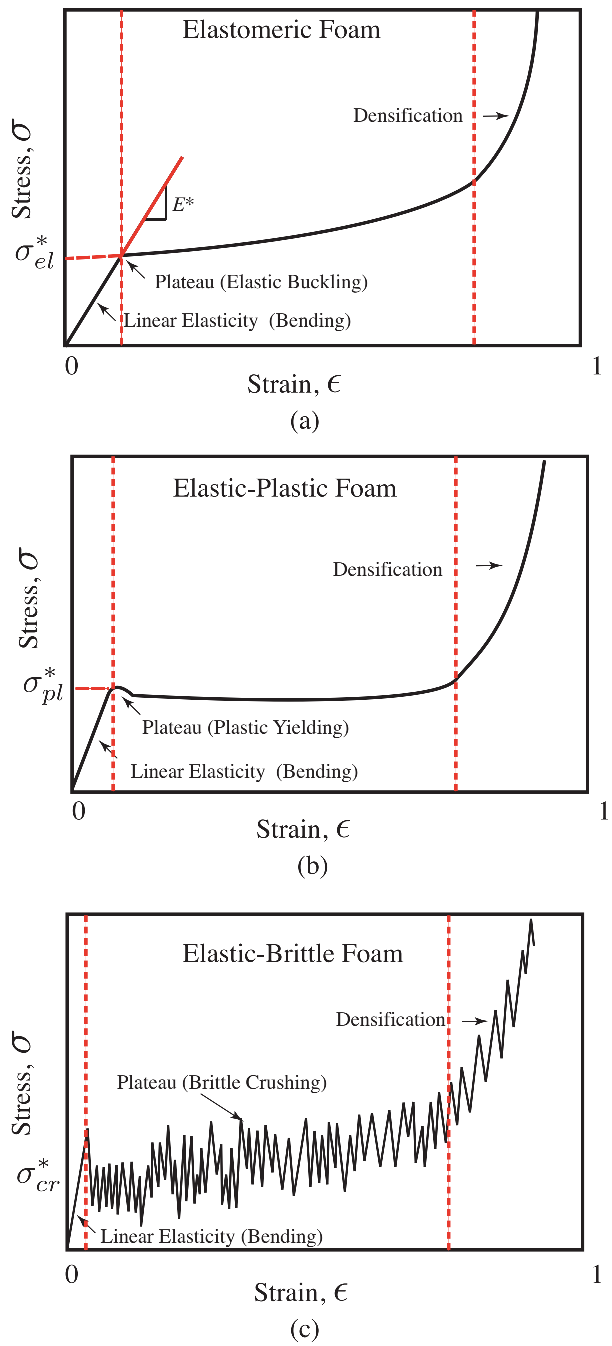

Figure 1.3. Examples of stess-strain curves for (a) elastomeric (b) elastic-plastic, (c) elastic-brittle foams, reinterpreted from [5].

G (acceleration pulse divided by g, the acceleration of gravity vs. static loading in a cushion curve as input. Burgess [23] extended his work by studying the multiple impact effects on shock absorption of closed-cell foams. The results show transmitted shock is increased due to cell-wall fatigue and rupture. These modeling efforts significantly reduced the necessary time to determine cushion curves from the experimental procedures outlined in ASTM D1596 [14]. Dynamic stress from impact events is added to static analysis in a study by Li et al. [24]. For various parameters in compression, a series of dynamic factor functions were generated. The predicted cushion curves were in agreement with those from ASTM D1596 [14].

The models evolved to both analytical solutions and numerical simulations of the impact. Sek et al. [25] used a computational model based a single degree of freedom to characterize cushion materials. A vibration model with integrated nonlinear spring and viscous damping were studied for cushions under impacts [26]. To obtain maximum accelerations for linearized local strains, velocity was equaled to zero. Including damping in the model reduced rigid impact to a certain level.

The compressive impact response of expanded polystyrene (EPS) foams with complex shapes were numerically predicted using finite element method (FEM) [27]. Multiple cycles of loading and unloading in finite element simulations of EPS foams were studied by Ozturk and Anlas [28]. Cushion curves were better predicted for single loading compared to multiple loading cases. Piatkowski et al. [29] proposed a method of dynamic stress-strain curves determination that assumes the energy density of foam collisions is obtained from the area under the stress-strain curve. The method processes the input data for FEM simulations that is helpful in case of limited access to experimental cushion curves.

With the exception of finite element simulations, these efforts were based on a lumped parameter approximation of the cushioning foam and impacting mass. The key to these modeling efforts is to capture both the dissipative and quasi-static stress-strain behavior of the material. In open-cell foams that are used in car seats, Azizi et al. [30] developed a single-degree-of-freedom foam-mass system with damping and nonlinear viscoelastic properties. In order to find steady-state response for the base excited system the incremental harmonic balance method was applied. In another similar study, viscoelastic models [31] were developed.

1.2.3 Brief Introduction to Metamaterials

A meta-material is any architected or engineered material or structure that shows a property that is not found in natural materials [32]. For example, electrical permittivity ϵ and magnetic permeability μ are negative for meta-materials that let waves flow in a backward fashion. Wegener [10] discussed the application of meta-materials beyond optics. For example, in pentamode metamaterials, the effective shear modulus is relatively small comparing to bulk modulus, that makes the complexities of waves propagation simpler. Wegener mentioned "Metamaterial unit cells could be constructed that break or buckle to dissipate mechanical shock energy. We also could work toward active mechanical metamaterials, integrating miniature energy sources together with sensors, actuators, and feedback loops into the individual unit cells. Nonlinear and active mechanical metamaterials are wide open for innovation." The focus of this work is to establish the use of these artificial materials in impact applications.

1.2.4 Literature Review of Metamaterials for Shock Absorption

In energy absorption applications, honeycomb structures have long been studied [33, 34]. In modern manufacturing methods such as 3D printing, the design of honeycomb structures is highly facilitated. In order to present the potential of 3D printed hyperelastic honeycombs as energy absorbing metamaterials, Bates et al. [35] manufactured flexible cellular structures by 3D printing thermoplastic polyurethanes (TPUs) using fused filament fabrication (FFF). The parametric study shows the advantages of the suggested FFF 3D manufacturing. Namely, these advantages are: 1) the energy absorption is a function of cell orientation and strain rate, 2) the structure was compressed repeatedly without failure, and 3) no obvious defects are observed in the structures.

Chen et al. [36] studied "new type of hierarchical honeycomb structure that exhibits a nearly linear relation between stiffness and relative density." The results showed enhanced energy absorption capability and recoverability. "The hierarchical honeycombs structures are fabricated using commercially available 3D printers and a brittle plastic polymer." Most of studies about honeycomb structures are limited to hexagonal cells. Habib et al. [37] designed nine types of honeycombs with different cell shapes to study the shape effect on in-plane response and energy absorption. Using finite element method, they showed the deformation of some honeycombs are dominated by bending of cell edges, while the others' response was dominated by plastic buckling.

Inspired from classic Kelvin 1887 model, Ge et al. [38] printed engineered cellular thermoplastic polyurethane cubes. The test indicated the cubes experienced the Mullins effect, a cyclic softening, was evident on the stress-strain curve. The presence of the Mullins effect was indicative of viscoelastic behavior. Comparing to rubber, the 3D printed foam has a much lower density, which is important in high-performance cushion materials.

Viscoelastic inks are 3D printed to create porous elastomeric architectures with ordered arrangement of struts, as potential replacements for shock absorbers, such as foams [39]. Directionally dependent load response including negative stiffness was exhibited by these structures.

Song et al. [40,41] optimized the geometry of structures with a square cross-section to provide broadband damping effects for vibration, acoustic and impact. These structures rely on beam buckling to shape their response. Furthermore, the structures are analyzed using the finite element method, and the samples are tested on an electrodynamic shaker. "With impact experiments, it is seen that the tapered internal geometry design leads to a greater instantaneous acceleration amplitude immediately after impact while more rapidly attenuating the energy when compared to the solid elastomer mass."

Square internal geometries are not the only topologies considered to capture impact energy. Using finite element analysis and experimental test, Li et al. [42], studied energy absorption enhancement of 3D printed auxetics (material with negative Poisson's ratio) reinforced composites. A parametric study was conducted to show the effect of Poisson's ratio and volume fraction of the auxetic structure.

Recent work by Vuyk et al. [43] on metamaterials has identified the origins of their shocks absorption capability; it originates from a combination of local and macroscopic deformations. The macroscopic deformation of the material is a product of localized non-affine buckling response of its local members. This mechanism has been known for years as the basis of the shock absorption properties of open cell polymer foams. It has also been noted that the buckling causes the effective damping to go to infinity, while the effective natural frequency of the structure goes to zero. Digital image correlation (DIC) was applied to present the integration of elastic buckling with microscopic and macroscopic deformations in elastomeric mechanical meta-materials. The results were validated with FEM. They emphasized the necessity of interdisciplinary studies of structural and material engineering for such structures. The study correlates energy dissipations with deformation behaviors.

Controlling the deformation behavior of the cells in meta-materials is a challenge. Bertoldi et al. [44] studied the deformation behavior of periodically patterned elastomeric materials. They investigated the effect of periodic pore shapes in elastomeric matrix on the deformation response. They showed that by changing the shape, the features of the structure, such as stiffness could be controlled for a desired expectation [45].

In a topical review, Hu et al. [46] discussed harnessing buckling and post-buckling behavior in smart structures. By combining numerous bistable elastic beams in a tilted direction and using 3D printing ink writing method, absorbed energy by the structure is trapped in the deformed beams to protect a package or person from impact loads [47]. Meaud and Che [48] studied wave propagation in bistable cells. Their numerical approach shows that the thickness to height of a beam in bistable structures is a critical parameter in tunability of wave propagation. Controlling instabilities in architected cellular structures can be applied in auxetic material design, energy absorption, and controlling elastic wave propagation [49]. If the cell's dimensions in a periodic cellular structure are identical, the buckling sequence is not predictable directly. However, by small variation of the cell size a deterministic deformation sequence is achieved [50]. An analytical and finite element simulation were developed. The FEM and experimental results were in agreement when a viscoelastic property was considered in the FEM model.

Cui and Harne [51] developed an analytical approach to study the relation between viscoelasticity and nonlinear behavior of engineered elastomeric structures, and their dynamic macroscopic behavior. The results were validated with experiments.

Quasi-zero stiffness (QZS) plays several roles in structures that absorb energy. Niu et al. [52] studied the advances in quasi-zero stiffness isolation systems that are applied in geodynamics, precision machines, etc. For example, in disk springs with a conical shape, the restoring force is a cubic function of displacement. QZS can be achieved by having two positive and negative stiffness springs in parallel.

1.3 Motivation and Research Questions

Cushion curves as a shock absorption metric, is a performance index in the most common designing methods for protective packaging [53]. Researchers developed numerical/analytical models for capturing cushion curves to save costs on exhaustive thousands experimental drop tests outlined in ASTM D1596 [14]. Except for finite element method models, current analytical/numerical models of foams in shock events are based on lumped parameter approximations. Assumption of lumped parameter model simplifies the analysis. However, the validity of lumped parameters models in providing a highly accurate prediction of cushion curves and other essential information such as the effect of higher-order modal effects on response has not been considered. This lack of knowledge leads to several open research questions:

1. *What are the effects of higher order modes of vibration on the rebound acceleration of an object impacting a cushion?*

2. *What are the effects of damping on the rebound acceleration?*

3. *Using this multimodal analysis, what are the dominant constitutive properties of foam for shock response?*

4. *Using this multimodal analysis, can a quasi-static compressive test be used to determine the acceleration pulse?*

Answering these questions are the initial focus of this dissertation in the examination of the shock response of foam.

The second part of this work utilizes the answers to the aforementioned research questions to guide the study of an architected material. In particular, the work is limited to studying the unit cell of one particular geometry, the χ structure. A complete description of this unit cell is found in Chapter 2. Analyzing the architected materials requires one to address the following questions:

5. *What geometry effectively mimics the quasi-static compression and shock absorption of an elastic closed cell foam?*

6. *Can the quasi-static compressive behavior of the architected material be modeled using FEA?*

7. *Can the elastic buckling of the structure be modeled analytically?*

8. *Can the geometry be tessellated to provide bi-directional tunable quasi-static compressive behavior?*

The developed analytical and numerical tools extend the horizon of understanding deformation of these structures. Many shock absorption applications such as car seats and packaging will benefit from this analysis.

1.4 Layout of Dissertation:

The remainder of this dissertation is organized as follows. Chapter 2 focuses on the prediction of shock response of a cushioned material using a nonlinear continuous model of a rod to represent the foam. The materials used in this study are an expanded polystyrene foam EPS20 [28], Styropor® [54] (BASF), and a polyethylene foam, Ethafoam® 150 (Nova Chemicals). Chapter 3 introduces the extended χ unit cell; it exhibits large regions of quasi-zero-modulus (QZM). The unit cells contains a network of beams arranged in a geometric configuration of two opposing triangles attached at their respective apexes to a vertical neck of finite length. In particular the chapter details the fabrication and finite element modeling of the structure. The unit cell's force-displacement relationship is recast into examining an effective stress and strain. Using these new metrics the unit cell constitutive behavior mimics that of the polymer foams in Chapter 2. The chapter introduces the effect of topology has on the effect on this constitutive relationship. Chapter 4 develops a semi-analytical model to predict the onset of the region of QZM. The model is based on the stiffness matrix of a beam-column where equilibrium conditions are imposed at each joint. In this chapter the topology is described by a characteristic angle. The buckling modes of the extended χ unit cell are predicted and compared to those obtained by a finite element analysis. The section concludes with a discussion of the effects of changing the characteristic angle effects length of the region of QZM. Chapter 5 examines the shock absorption characteristics of the extended χ unit cell. It does this by first examining the theoretical cushion curves the unit cell would yield if impacted using a lumper parameter model of the structure and concepts introduced in Chapter 2. Then finite element models are used to examine the effect of the characteristic angle and leg thickness on the absorbed energy of the structure and the length of the QZM region. Chapter 6 discusses tessellating the extended χ structure in two dimensions to provide multi-directional protection. The chapter presents the fabrication, characterization and modeling of the structure as well as discussion of its limitations. Chapter 7 is the final chapter and it discusses how the work addressed the research question laid out in this chapter. In addition, it provides a roadmap for improving upon the existing work and extending the concepts presented into new avenues of inquiry.

2. PREDICTION OF CUSHION CURVES OF POLYMER FOAMS USING A NONLINEAR DISTRIBUTED PARAMETER MODEL

The following subsections are reprinted, in part, from Joodaky, A., Batt, G. S., & Gibert, J. M. (2020). Prediction of cushion curves of polymer foams using a nonlinear distributed parameter model. Packaging Technology and Science, 33(1), 3-14 [55].

2.1 Introduction

This chapter aims to provide a rigorous analysis beyond the lumped parameter paradigm on the prediction of shock response of cushioned materials. The materials used in this study are an expanded polystyrene foam EPS20 [28], Styropor® [54] (BASF), and a polyethylene foam, Ethafoam® 150 (Nova Chemicals). Like other expanded polymer foams, they demonstrate complex stress-strain relationship characterized by viscoelasticity and elastic nonlinearities. In this work, we explore the effects of approximating the behavior: 1) with a polynomial stress-strain relationship and a linear viscous damping term, and 2) and expand upon previous analytical and numerical models of packaging foams by deriving the equations of motion based on an analysis of the foam as a continuous body [56]. The simplification of the material behavior as hyperelastic and viscous allows the determination of the material constants in the model using a single drop test and a single compression test.

The remainder of the chapter is organized as follows: Section 2.2 presents a phenomenological model previously developed to capture the nonlinear elasticity of the closed cell foam. Section 2.3 derives the equations of motion of the mass impacting a hyperelastic rod used to approximate the ASTM tests. Section 2.4 covers the study of the analytical solution behavior for varying drop heights and static stresses. Section 2.5 presents a discussion on model implication and limitations. Section 2.6 presents concluding remarks.

2.2 Constitutive Relationships

Previous models of closed cell foams have captured material behavior by assuming the deformation can be isothermal compression of trapped air in a deformable volume [23,57], or by a nonlinear deformation [58]. In developing a model for the material behavior of the foam; if we consider a nonlinear hyperelastic compression Ogden model of deformation [59], the constitutive relation of a polymer can be written as

$$\sigma(t) = F(\tilde{e}(t), \dot{\tilde{e}}(t)), \tag{2.1}$$

where $\tilde{e}$ is the finite strain. In one dimensional problems, $\tilde{e}$ is defined as

$$\tilde{e} = \frac{\partial u}{\partial x} + \frac{1}{2}\left(\frac{\partial u}{\partial x}\right)^2 = \epsilon + \frac{1}{2}\epsilon^2. \tag{2.2}$$

The infinitesimal strain of linear elasticity is $\epsilon = \frac{\partial u}{\partial x}$, or length ratio $\lambda = 1 + \tilde{e}$ [58]. Banks et al. [60] noted that since finite strains are themselves nonlinear functions of the infinitesimal strains ϵ, Eqn. (2.1) can be written in terms ϵ. Furthermore, the stress-strain relationship can be decomposed as a sum of hyperelastic (σ_{HE}) and viscoelastic ($\sigma_{VE}(t)$) components where the hyperelastic terms can be represented as a polynomial and the viscoelastic term in terms of a hereditary integral [31,61]. Here, we represent the complete stress in the material as a polynomial (σ_p) representing the stress at a quasi-static state and a viscous loss component using a Kelvin Voigt model of damping (σ_v):

$$\sigma(t) = f\left(\frac{\partial u}{\partial x}, \frac{\partial^2 u}{\partial t \partial x}\right) = E_1\left(\frac{\partial u}{\partial x}\right) + \sum_{k=2}^{K} E_1 E_k \left(\frac{\partial u}{\partial x}\right)^k + C_D \frac{\partial^2 u}{\partial t \partial x}, \tag{2.3}$$

where the constant E_1 is the linear elastic modulus, E_k are the relative nonlinear moduli, and C_D is the damping constant, $\sigma_p = E_1\left(\frac{\partial u}{\partial x}\right) + \sum_{k=2}^{K} E_1 E_k \left(\frac{\partial u}{\partial x}\right)^k$, and $\sigma_v(t) = C_D \frac{\partial^2 u}{\partial t \partial x}$. The effective damping constant C_D is not determined from material characterization, and will be determined directly from one point on the drop test.

Figure 2.1 (a) is a plot of the quasi-static stress-strain curve of the expanded polystyrene (EPS20) foam with density $\rho = 20$ kg/m^3, that was compressed at a rate of 100 mm/min using a Zwick universal testing machine at room temperature [28]. The quasi-static region can be divided into three distinct regions; Region I, Region II,

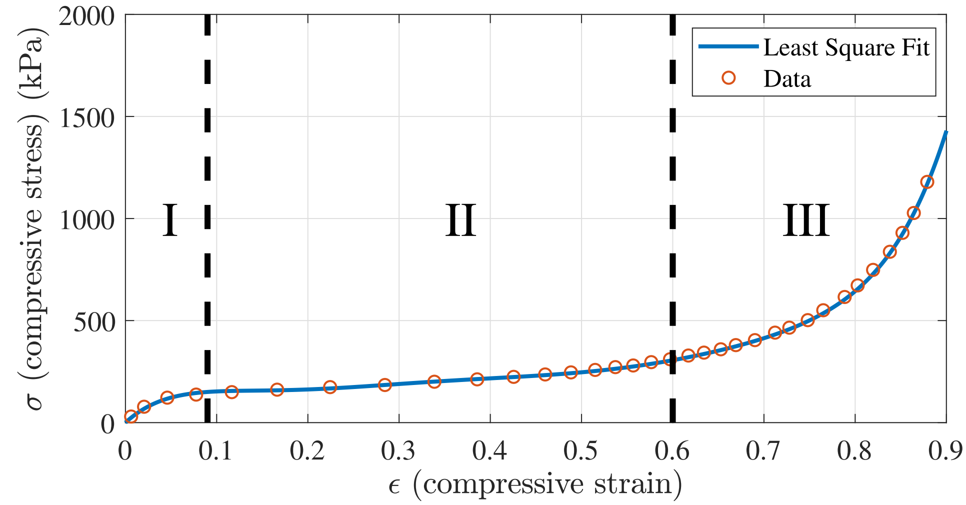

(a)

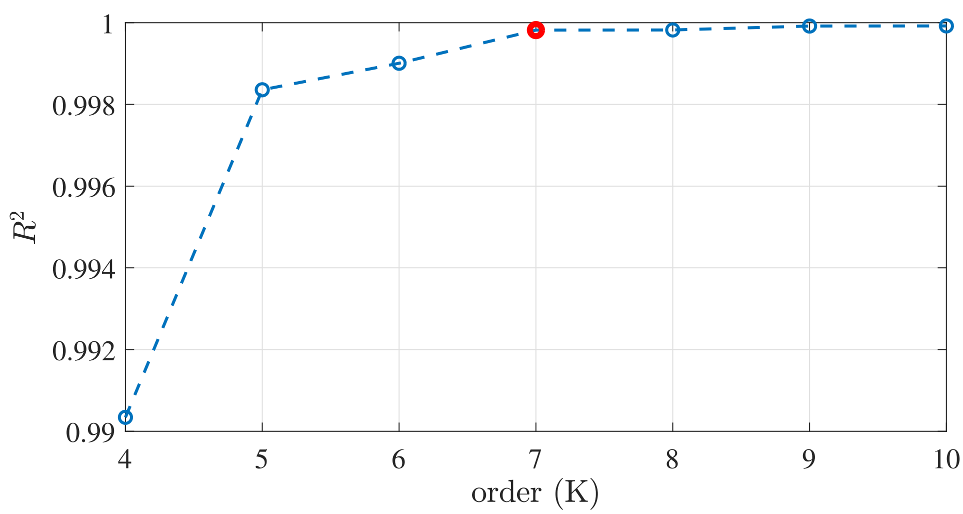

(b)

Figure 2.1. Quasi-static stress strain curve of expanded polystyrene: (a) Static compression curve of EPS20 [28] and (b) R^2 values for least square curve fits where polynomial order, K, ranges from 4 to 10. Region I is due to linear elastic deformation. Region II is due to buckling of cell walls. Region III is due to contacting of collapsed cell walls.

and Region III [5,62] . Region I occurs between 5-8% nominal strain; the foam deforms elastically, controlled by cell wall bending and cell face stretching. At the apex of this region, the collapse of cells walls is due to elastic buckling. The plateau region, Region II, is between 10-60% strain. In this region, cell wall buckling occurs causing large deflection due to small increases in force. Region III occurs past the plateau and is known as the densification region; the foam's cells collapse on themselves, and the material compacts under increasing compression.

2.2.1 Polynomial Approximation of Hyperelastic Constitutive Parameter Identification

The quasi-static, hyperelastic behavior can be modeled as a polynomial using a least squares fit [63]. For obtaining a highly accurate polynomial fit, the number of terms in the approximation is equal to seven ($K = 7$); the coefficients for the fit are given in Table 2.1. In Fig. 2.1 (a), the experimental data is illustrated with red circular dots, and the curve fit with a blue line. The seventh order polynomial captures the stress in the three regions of deformation. Figure 2.1 (b) shows R^2 values for polynomial fits with orders ranging from 4 to 10.

Table 2.1. Modulus and relative moduli for uniaxial compression polynomial model of EPS20 [28].

E_1	4.12 MPa	E_5	252.70 MPa/MPa
E_2	-10.53 MPa/MPa	E_6	-206.06 MPa/MPa
E_3	56.12 MPa/MPa	E_7	68.34 MPa/MPa
E_4	-16.54 MPa/MPa		

2.3 Nonlinear Distributed Parameter Model

A schematic of the drop test is illustrated in Fig. 2.2 (a), while the distributed parameter model used in this study is represented by Fig. 2.2 (b). The distributed parameter model is a one-dimensional rod with a lumped mass, M, attached to one end and the other end attached to a rigid surface. The rod represents the foam, while the mass represents the weight used in the drop test. The impact is treated as an initial value problem, where the velocity of the weight just prior to impact is the initial velocity of the system. Finally, the model assumes that the Poisson's ratio of the foam is zero, i.e., there is no change in the cross section as the foam is compressed or stretched. The equation of motion describing the longitudinal motion of the rod can be written as the damped nonlinear wave equation:

$$\frac{\partial^2 u}{\partial t^2} = \frac{C_D}{\rho}\frac{\partial^3 u}{\partial t \partial x^2} + \frac{\partial}{\partial x}\left(c^2\left(\frac{\partial u}{\partial x} + \sum_{k=2}^{K} E_k\left(\frac{\partial u}{\partial x}\right)^k\right)\right), \tag{2.4}$$

where $u(x,t)$ is the displacement of the foam and is taken as positive downward from the top of the foam, $c = \sqrt{(E_1/\rho)}$ is the elastic wave speed, ρ is the apparent density of the uncompressed foam, C_D is loss coefficient assuming Kelvin Voight damping, E_1 is the absolute linear modulus of the material, E_k is the relative nonlinear modulus of the foam, A is the cross-section area, and L is the thickness of the foam. Neglecting damping, the boundary conditions of zero displacement at the fixed end and stress continuity at the free end can be written as

$$\begin{aligned} &u(L,t) = 0 \quad \text{and} \\ &M\left.\frac{\partial^2 u}{\partial t^2}\right|_{x=0} = E_1 A\left(\frac{\partial u}{\partial x} + \sum_{k=2}^{K} E_k\left(\frac{\partial u}{\partial x}\right)^k\right)\Bigg|_{x=0} + Mg, \end{aligned} \tag{2.5}$$

with initial conditions

$$u(x,0) = u_s(x), \qquad \frac{\partial u(x,0)}{\partial t} = \sqrt{2gH}, \tag{2.6}$$

where g is gravitational constant, M is the mass of the platten, H is the drop height, and $u_s(x)$ is an unknown function due to the static deflection. The stress continuity

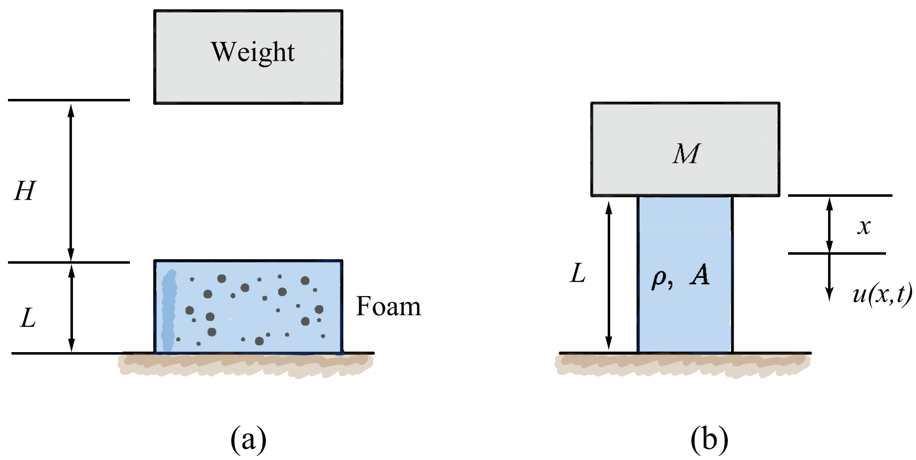

Figure 2.2. Representation of drop test: (a) schematic of drop test and (b) equivalent model using a continuous rod approximation.

boundary condition can be rewritten in terms of the static stress by noting that the mass can be written as function of the static stress, σ_s, as $M = \sigma_s A/g$, to yield

$$\frac{\sigma_s}{E_1 g}\frac{\partial^2 u}{\partial t^2}\bigg|_{x=0} = \left(\frac{\partial u}{\partial x} + \sum_{k=2}^{K} E_k \left(\frac{\partial u}{\partial x}\right)^k\right)\bigg|_{x=0} + \frac{\sigma_s}{E_1}. \tag{2.7}$$

2.3.1 Static Analysis

In order to solve Eqn. (2.4), the displacement, $u(x,t)$, can be written in terms of a static equilibrium position, $u_s(x)$, and a time dependent perturbation displacement, $\hat{u}(x,t)$, such that

$$u(x,t) = \hat{u}(x,t) + u_s(x). \tag{2.8}$$

The partial differential equation (PDE) and its boundary conditions are expanded about the static equilibrium shape, $u_s(x)$, which is determined by setting the time-dependent terms to zero, leaving the following boundary value problem

$$\frac{\partial}{\partial x}\left(c^2\left(\frac{\partial u_s}{\partial x} + \sum_{k=2}^{K} E_k \left(\frac{\partial u_s}{\partial x}\right)^k\right)\right) = 0. \tag{2.9}$$

The corresponding static boundary conditions are

$$u_s(L) = 0 \quad \text{and} \quad \left(\frac{\partial u_s}{\partial x} + \sum_{k=2}^{K} E_k \left(\frac{\partial u_s}{\partial x} \right)^k \right) \Bigg|_{x=0} + \frac{\sigma_s}{E_1} = 0. \tag{2.10}$$

Finally, the boundary value problem in Eqn. (2.9) can be written as

$$c^2 \frac{\partial^2 u_s}{\partial x^2} \left(1 + \sum_{k=2}^{K} k E_k \left(\frac{\partial u_s}{\partial x} \right)^{k-1} \right) = 0. \tag{2.11}$$

Examining the boundary value problem reveals that either $\partial^2 u_s / \partial x^2$ or $1 + \sum_{k=2}^{K} k E_k \left(\frac{\partial u_s}{\partial x} \right)^{k-1}$ must be zero. The latter condition is of the same order the boundary condition and cannot be the governing equation of motion. Thus a solution to Eqn. (2.11) is also a solution to the linear problem $\partial^2 u_s / \partial x^2 = 0$ [63–65] and can be written as

$$u_s(x) = \epsilon_s (x - L), \tag{2.12}$$

where ϵ_s is the nonlinear static strain and root of

$$\epsilon_s + \sum_{k=2}^{K} E_k \epsilon_s^k + \frac{\sigma_s}{E_1} = 0. \tag{2.13}$$

Having determined the static deformation of the rod, the nonlinear equation of motion around the static deformation can be written as

$$\begin{aligned} \frac{\partial^2 \hat{u}}{\partial t^2} &= \frac{C_D}{\rho} \frac{\partial^3 \hat{u}}{\partial t \partial x^2} + c^2 \frac{\partial^2 \hat{u}}{\partial x^2} \left(1 + \sum_{k=2}^{K} k E_k \left(\frac{\partial \hat{u}}{\partial x} + \epsilon_s \right)^{k-1} \right), \\ &= \frac{C_D}{\rho} \frac{\partial^3 \hat{u}}{\partial t \partial x^2} + c^2 \frac{\partial^2 \hat{u}}{\partial x^2} \left(1 + \sum_{k=2}^{K} k E_k \sum_{j=0}^{k-1} \left(\binom{k-1}{j} \left(\frac{\partial \hat{u}}{\partial x} \right)^{k-1-j} \epsilon_s^j \right) \right). \end{aligned} \tag{2.14}$$

According to the binomial expansion formula,

$$\left(\frac{\partial \hat{u}}{\partial x} + \epsilon_s \right)^{k-1} = \sum_{j=0}^{k-1} \left(\binom{k-1}{j} \left(\frac{\partial \hat{u}}{\partial x} \right)^{k-1-j} \epsilon_s^j \right), \tag{2.15}$$

where $\binom{k-1}{j} = \frac{(k-1)!}{(j)!(k-1-j)!}$, and the symbol $(n)!$ denotes the factorial, and $n = j$, or $(k-1)$. The associated initial conditions can be written as

$$\hat{u}(x,0) = 0 \quad \text{and} \quad \frac{\partial \hat{u}(x,0)}{\partial t} = \sqrt{2gH}, \tag{2.16}$$

and the boundary conditions can be written as

$$\hat{u}(L,t) = 0, \quad \text{and} \quad \left(\frac{\partial \hat{u}}{\partial x} + \epsilon_s + \sum_{k=2}^{K} E_k \left(\frac{\partial \hat{u}}{\partial x} + \epsilon_s \right)^k \right) \Bigg|_{x=0} + \frac{\sigma_s}{E_1} = \frac{\sigma_s}{E_1 g} \frac{\partial^2 u}{\partial t^2} \Bigg|_{x=0}. \tag{2.17}$$

Again, utilizing the binomial expansion

$$\left(\frac{\partial \hat{u}}{\partial x} + \epsilon_s \right)^k = \sum_{j=0}^{k} \left(\binom{k}{j} \left(\frac{\partial \hat{u}}{\partial x} \right)^{k-j} \epsilon_s^j \right) = \sum_{j=0}^{k-1} \left(\binom{k}{j} \left(\frac{\partial \hat{u}}{\partial x} \right)^{k-j} \epsilon_s^j + \epsilon^k \right) \tag{2.18}$$

where $\binom{k}{j} = \frac{(k)!}{(j)!(k-j)!}$, the stress boundary condition can be written as

$$\left(\frac{\partial \hat{u}}{\partial x} + \epsilon_s + \sum_{k=2}^{K} E_k \left(\sum_{j=0}^{k-1} \left(\binom{k}{j} \left(\frac{\partial \hat{u}}{\partial x} \right)^{k-j} \epsilon_s^j \right) + \epsilon_s^k \right) \right) \Bigg|_{x=0} + \frac{\sigma_s}{E_1} = \frac{\sigma_s}{E_1 g} \frac{\partial^2 u}{\partial t^2} \Bigg|_{x=0}, \tag{2.19}$$

using Eqn.(2.13) the boundary condition simplifies to

$$\left(\frac{\partial \hat{u}}{\partial x} + \sum_{k=2}^{K} E_k \left(\sum_{j=0}^{k-1} \binom{k}{j} \left(\frac{\partial \hat{u}}{\partial x} \right)^{k-j} \epsilon_s^j \right) \right) \Bigg|_{x=0} = \frac{\sigma_s}{E_1 g} \frac{\partial^2 u}{\partial t^2} \Bigg|_{x=0}. \tag{2.20}$$

2.3.2 Linear Analysis

In performing a linear analysis around the static deflection one can obtain both an analytical expression for the shock response and determine candidate admissible spatial functions of the displacement that can be used to perform a Galerkin expansion to discretize the nonlinear partial differential equation of motion

$$\frac{\partial^2 \hat{u}}{\partial t^2} = c_{eff}^2 \frac{\partial^2 \hat{u}}{\partial x^2}, \tag{2.21}$$

where $c_{eff}^2 = c^2 \left(1 + \sum_{k=2}^{K} k E_k \epsilon_s^{k-1}\right)$ with initial conditions of Eqn. (2.16) and boundary conditions

$$\hat{u}(L,t) = 0, \quad \text{and} \quad \left.\frac{\partial \hat{u}}{\partial x}\right|_{x=0} = \frac{\sigma_s}{E_{1,eff}\, g} \left.\frac{\partial^2 u}{\partial t^2}\right|_{x=0}, \tag{2.22}$$

where $E_{1,eff} = E_1 \left(1 + \sum_{k=2}^{K} k E_k \epsilon_s^{k-1}\right)$. We assume a separable spatial and temporal solution that can be written as

$$\hat{u}(x,t) = \hat{U}(x) q(t). \tag{2.23}$$

Plugging in Eqn. (2.23) into the expressions of Eqn. (2.22), eliminating the temporal coordinate leads to the characteristic equation

$$\alpha \tan \alpha = \beta, \tag{2.24}$$

where $\beta = \rho g L/\sigma_s$ represents the ratio of foam's weight per unit length to static stress. Note that this equation is transcendental and can be solved for α_n, where $n = 1, 2 \ldots \infty$. The eigenvalues α_n can be related to modal frequencies by $\alpha_n = \omega_n L/c_{eff}$. The temporal equations can be written as

$$\ddot{q}_n(t) + \omega_n^2 q_n(t) = 0. \tag{2.25}$$

The displacement of the foam can be written as

$$\hat{u}(x,t) = \sum_{n=1}^{\infty} C_n \left(-\frac{\beta}{\alpha_n} \cos\left(\frac{\alpha_n x}{L}\right) + \sin\left(\frac{\alpha_n x}{L}\right)\right) \left(\frac{v_{0n}}{\omega_n} \sin \omega_n t\right), \tag{2.26}$$

where v_{0n} and g_{0n} are the contributions of each mode on the velocity and acceleration initial condition. The constant C_n is obtained by enforcing the orthogonality condition

$$\int_0^L \hat{U}_m(x)\hat{U}_n(x)dx + \frac{L}{\beta}\hat{U}_m(0)\hat{U}_n(0) = \delta_{mn}, \tag{2.27}$$

where δ_{mn} is the Kronecker delta function, see Appendix A. The orthogonality of normal modes allows the initial conditions can be written as

$$\begin{aligned} q_n(0) &= 0, \quad n = 1, 2, \ldots \\ \dot{q}_n(0) &= \sqrt{2gH}\left(\int_0^L \hat{U}_n(x)dx + \frac{L}{\beta}\hat{U}_n(0)\right) = v_{0n}, \quad n = 1, 2, \ldots \end{aligned} \tag{2.28}$$

Finally, as the static stress increases, β approaches zero, then the characteristic equation of Eqn. (2.24) becomes $\tan\alpha = 0$. Obviously, in this case $\alpha_n = n\pi/2$, where $n = 1, 2 \ldots \infty$. The acceleration of the impacting mass can be written as

$$\left.\frac{\partial^2 u(x,t)}{\partial t^2}\right|_{x=0} = \sum_{n=1}^{\infty} -v_{0n}C_n\omega_n\left(\frac{\beta}{\alpha_n}\right)\sin\omega_n t. \tag{2.29}$$

Note that the acceleration is a sum of sinusoids each with an amplitude of $v_{0n}C_n\omega_n\left(\frac{\beta}{\alpha_n}\right)$, which is denoted as the amplitude G_n. G_n is directly proportional to the velocity of the platten at impact for each mode of vibration and can be normalized as $G_n/(c/L\sqrt{2gH})$ and can be plotted versus static stress, σ. It is evident from this plot that the first mode dominates the response with its amplitude being an order of magnitude higher than the higher order modes of vibration, see Fig. 2.3. The amplification factor for each mode initially decreases as the static stress increases until each reaches an asymptote. Figure 2.4 shows the normalized eigenvalues or normalized frequencies versus static stress. The first mode decreases with static stress. The higher order modes are nearly constant as static stress increases.

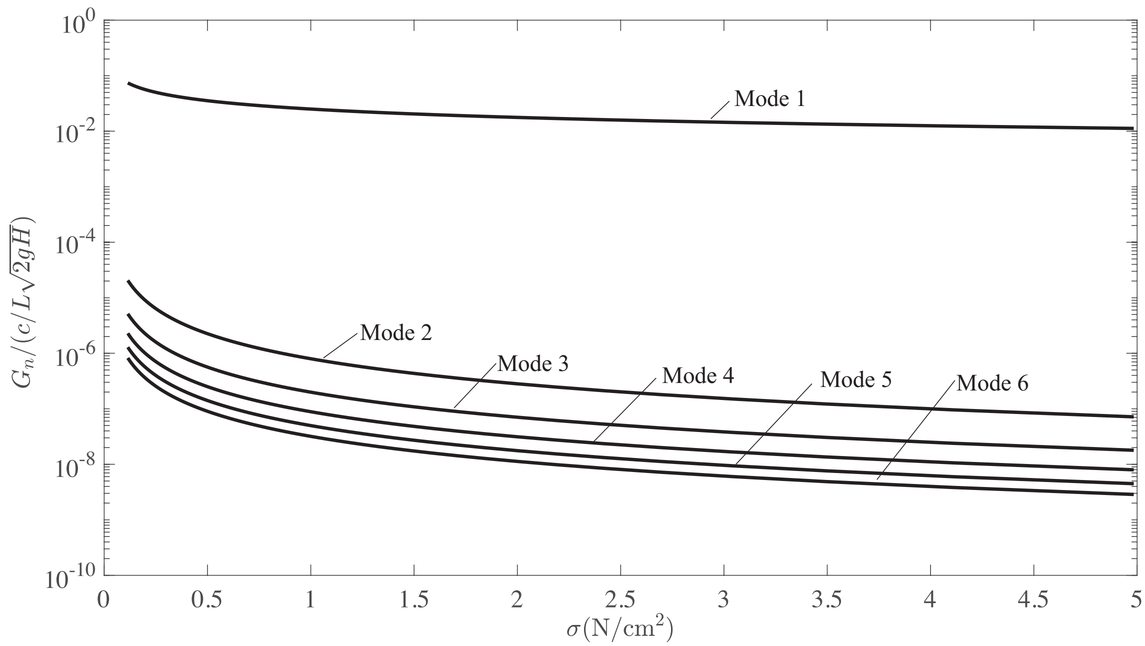

Figure 2.3. Normalized maximum acceleration of the first six modes versus static stress.

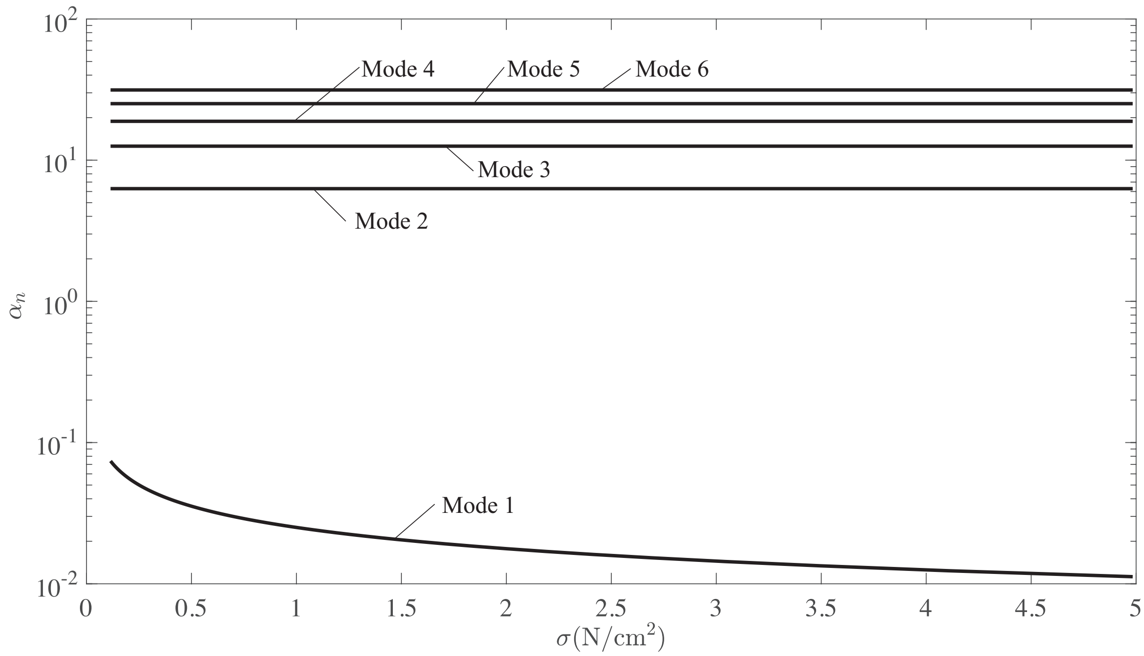

Figure 2.4. Normalized eigenvalues of the first six modes versus static stress.

2.3.3 Non-Linear Analysis

A Galerkin expansion is used to discretize Eqn. (2.14) by assuming a solution that has the separable form as a finite series of

$$\hat{u}(x,t) = \sum_{n=1}^{N} \hat{U}_n(x) q_n(t), \tag{2.30}$$

where $q_n(t)$ are the generalized time-dependent coordinates, and $\hat{U}_n(x)$ are the set of mass-normalized, orthonormal admissible functions representing the mode shapes of a clamped-free uniform rod with a tip mass attached at the free end. The admissible functions are obtained by solving the linear differential eigenvalue problem defined by Eqn. (2.21) and its associated boundary conditions when the nonlinearity is neglected, and damping C_D set to zero. The functions can be written as

$$\hat{U}_n(x) = C_n \left(\frac{\beta}{\alpha_n} \cos\left(\frac{\alpha_n x}{L}\right) + \sin\left(\frac{\alpha_n x}{L}\right)\right). \tag{2.31}$$

The constant $\beta = \rho g L/\sigma_s$ represents the ratio of foam's weight per unit length to static stress and $\alpha_n = \omega_n L/c$ is the dimensionless, undamped natural frequency determined from the characteristic equation

$$\alpha_n \tan \alpha_n = \beta. \tag{2.32}$$

The constant C_n is obtained by enforcing the orthogonality condition

$$\int_0^L \hat{U}_m(x)\hat{U}_n(x)dx + \frac{L}{\beta}\hat{U}_m(0)\hat{U}_n(0) = \delta_{mn}, \tag{2.33}$$

where δ_{mn} is the Kronecker delta function. The boundary conditions can then be written as

$$\sum_{n=1}^{N} \hat{U}_n(L)q_n(t) = 0,$$
$$\sum_{n=1}^{N}\left(\hat{U}'_n(0)q_n(t) + \sum_{k=1}^{K} E_k\left(\sum_{j=0}^{k-1}\binom{k}{j}\left(\hat{U}'_n(0)q_n\right)^{k-j}\epsilon_s^j\right)\right) = \frac{\sigma_s}{E_1 g}\sum_{n=1}^{N}\hat{U}_n(0)\ddot{q}_n(t). \quad (2.34)$$

Substituting Eqn. (2.30) into Eqn. (2.4) yields

$$\sum_{n=1}^{N}\hat{U}_n(x)\ddot{q}_n(t) =$$
$$\frac{C_D}{\rho}\sum_{n=1}^{N}\hat{U}''_n(x)\dot{q}_n(t) + c^2\left(1+\sum_{k=2}^{K} kE_k\left(\sum_{j=0}^{k-1}\binom{k}{j}\left(\sum_{n=1}^{N}\hat{U}'_n(x)q_n\right)^{k-1-j}\epsilon_s^j\right)\right)\times \quad (2.35)$$
$$\left(\sum_{n=1}^{N}\hat{U}''_n(x)q_n(t)\right) = 0.$$

Multiplying by $\hat{U}_m(x)$ and integrating over the length of the rod while exploiting the orthogonal properties of the admissible functions yields the following set of nonlinear, ordinary differential equations for N modes. In a similar procedure, Eqn. (2.35) is multiplied by other $\hat{U}_n(n > 1)$ and integrated over 0 to L. Eventually N set of coupled equations, analogous to Eqn.(2.35) can be written as

$$\ddot{q}_n(t) + \omega_n^2 q_n(t) = \frac{C_D}{\rho}\left(\int_0^L \hat{U}_n(x)\sum_{s'=1}^{N}\hat{U}''_{s'}(x)\,dx - \hat{U}_n(0)\sum_{s'=1}^{N}\hat{U}'_{s'}(0)\right)\dot{q}_{s'}(t)$$
$$+ c^2\int_0^L\left(\sum_{k=2}^{K} kE_k\left(\sum_{j=0}^{k-2}\binom{k-1}{j}\epsilon_s^j\left(\sum_{s'=1}^{N}\hat{U}'_{s'}(x)q_{s'}\right)^{k-1-j}\right)\hat{U}_n(x)\sum_{s'=1}^{N}\hat{U}''_{s'}(x)\right)\,dx\; q_{s'}(t)$$
$$- c^2\hat{U}_n(0)\sum_{k=2}^{K} E_k\left(\sum_{j=0}^{k-2}\left(\binom{k}{j}\epsilon_s^j\left(\sum_{s'=1}^{N}\hat{U}'_{s'}(0)q_{s'}(t)\right)^{k-j}\right)\right) = 0.$$
$$(2.36)$$

Finally, Eqn.(2.36) and the associated initial conditions,

$$q_n(0) = 0, \quad \text{and} \quad \dot{q}_n(0) = v_{0n},$$

are solved numerically yielding $q_n(t)$. Eqn. (2.30) is used to recover the complete response.

2.4 Single Mode Representation of Cushioning System Response

Assuming that the response is dominated by the first modal frequency of the rod, the set of nonlinear differential equations (2.35) reduces to

$$\begin{aligned} \ddot{q}_1(t)+&2\zeta_1\omega_1\dot{q}_1(t) + \omega_1^2 q_1(t) + \bar{\alpha}_{12}q_1^2(t) + \bar{\alpha}_{13}q_1^3(t) + \bar{\alpha}_{14}q_1^4(t)+ \\ &\bar{\alpha}_{15}q_1^5(t) + \bar{\alpha}_{16}q_1^6(t) + \bar{\alpha}_{17}q_1^7(t) = 0, \end{aligned} \tag{2.37}$$

the coefficients of which are contained in Appendix B with initial conditions $q_1(0) = 0$, and $\dot{q}_1(0) = v_{01}$, Solutions of Eqn. (2.37) provide estimates of the shock pulse magnitude and duration.

2.4.1 An Energy Based Estimation of the Cushion Curve

Similar to Ramon and Miltz [20] and Burgess [21,22], the polynomial description of the cushion's material behavior allows the use of conservation of energy to estimate the peak acceleration during the weight/foam impact. The process begins by assuming that the system is conservative, i.e., setting ζ_1 to zero and again ignoring the inertial initial condition. The equation of motion can then be written as

$$\ddot{q}_1(t)+\omega_1^2 q_1(t)+\bar{\alpha}_{12}q_1^2(t)+\bar{\alpha}_{13}q_1^3(t)+\bar{\alpha}_{14}q_1^4(t)+\bar{\alpha}_{15}q_1^5(t)+\bar{\alpha}_{16}q_1^6(t)+\bar{\alpha}_{17}q_1^7(t) = 0. \tag{2.38}$$

Rewriting Eqn. (2.38) in terms of the potential energy as

$$\ddot{q}_1(t) + \frac{dV(q_1(t))}{dq_1(t)} = 0 \quad \text{and} \quad V(q_1(t)) = \omega_1^2 \frac{q_1(t)^2}{2} + \sum_{i=2}^{7} \bar{\alpha}_{1i} \frac{q_1(t)^{i+1}}{i+1}, \tag{2.39}$$

Next, multiplying Eqn. (2.39) by $\dot{q}_1(t)$ allows the governing equation to be rewritten as

$$\frac{d}{dt}\left(\frac{1}{2}\dot{q}_1(t)^2 + V(q_1(t))\right) = 0, \quad \text{or} \quad \frac{1}{2}\dot{q}(t)_1^2 + V(q_1(t)) = C = \text{constant}, \tag{2.40}$$

where the latter is the Hamiltonian of the system. Applying the initial conditions, the constant in Eqn. (2.40) is obtained as

$$C = gH\left(\int_0^L \hat{U}_1(x)dx + \frac{L}{\beta}\hat{U}_1(0)\right)^2. \tag{2.41}$$

When damping is neglected, the acceleration reaches its peak when $\dot{q}_1(t) = 0$ and displacement is at its maximum, $q_1 = q_{1,max}$, thus Eqn. (2.40) becomes,

$$V(q_{1,max}) = \omega_1^2 \frac{q_{1,max}^2}{2} + \sum_{i=2}^{7} \bar{\alpha}_{1i} \frac{q_{1,max}^{i+1}}{i+1} = C. \tag{2.42}$$

Equation (2.42) is a polynomial in $q_{1,max}$, i.e., the generalized coordinate when the compressive deformation is maximum whose roots can be solved. The peak acceleration, $\ddot{q}_{1,max}$, can be recovered by substituting back into Eqn. (2.38). Finally, the ratio of maximum deceleration to gravity, G, used for generating the cushion curve, is obtained as

$$G = \frac{\ddot{u}(0, t_{max})}{g} = \frac{\hat{U}_1(0)\ddot{q}_{1,max}}{g}. \tag{2.43}$$

2.5 Results

In this section an analysis of the effects of the modes used in the numerical model is conducted by: 1) the analytical and numerical predictions of the cushion curves are compared to experimentally determined cushion curves, and 2) the analytical predictions of a shock pulse is compared to experimental data. Published quasi-static stress-strain data [28] and experimentally determined cushion curves for Styropor® (BASF) [54] are used for the modal analysis and cushion curve analysis of Sections 2.5.1 and 2.5.2. The shock pulse analysis of Section 2.5.3 is conducted using stress-strain and impact response behavior characterized in this study for Ethafoam® 150 (Nova Chemicals).

2.5.1 Modal Effects

Model predictions are made using EPS20 foam with the quasi-static compression moduli defined in Table 2.1 [28]. We begin our study by examining the effect of the number of modes used in the prediction of the impact responses.

The model predicted shock response of the system is explored without damping, see Fig. 2.5, and with damping, see Fig. 2.6, for single and multiple mode approximations. The damping present in the material is assumed to be viscous damping and is determined by finding the value that matches a single amplitude determined from a set of cushion curves. A H/L of 24 and a static stress of 1 N/cm^2 is used to determine the proper model viscous damping ratio of $\zeta = 0.012$. The foam modeled has a cross sectional area of 192 cm^2 and thickness of 3.2 cm. Figure 2.5 contains the response of the displacement, velocity and acceleration for the case, $H/L = 16$, with zero damping. Note that two wave forms are shown in each subfigure; single mode predictions are indicated by dots and three mode predictions are indicated by lines. The time histories of the foam's top surface deformation during impact are plotted, see Fig. 2.5 (a), (d), and (g), for static stresses of 0.4 kPa, 5 kPa, and 15 kPa, respectively. These static stresses correspond to regions I, II, and III of the stress strain curve in Fig. 2.1. The corresponding velocities at the top surface are plotted in Fig. 2.5 (b), (e), and (h). The acceleration waveforms are shown in Fig 2.5 (c), (f), and (i).

Several noteworthy trends are observed in the undamped displacement, velocity, and acceleration plots, see Fig. 2.5. 1) The amplitude and shape of the acceleration shock pulse depend on the static stress. 2) The pulses are symmetric about the peak in the absence of damping. 3) The effects of the higher modes of vibrations differ based on the hyperelastic region of strain. In Region II, the simulations indicate that little energy is present in the higher order modes. When the strain either decreases or increases to Region I or III respectively, the higher order modes are more pronounced.

The addition of damping to the system is explored, and several observations are made. The presence of damping reduces the effect of higher modes as seen in Fig. 2.6. As the damping in the system is increased, the effect of the higher modes are mitigated. The higher mode waveforms are almost coincident with their respective single mode equivalent. For these reasons, the remaining analysis is performed with only one mode of vibration and the effects of damping are further explored.

2.5.2 Cushion Curve Prediction

The peak amplitudes of the predicted acceleration pulses at various static stresses are used to generate cushion curves for various drop height to cushion thickness ratios for comparison to experimental data, see Fig. 2.7. Cushion curves are generated for drop height to cushion thickness ratios of 2, 8, 16, 24, 28, and 40. The energy based estimation (undamped) is indicated with blue circular dots, the numerical integration estimation (damped) is indicated with black dots, and the experimental data is represented by green dashed lines. The red dash lines indicate the ±18% lab-to-lab variation expected in experimental data per ASTM D1596. In all cases, model predictions and experimental data exhibit good agreement. However, model and experimental cushion curve agreement is further improved with the incorporation

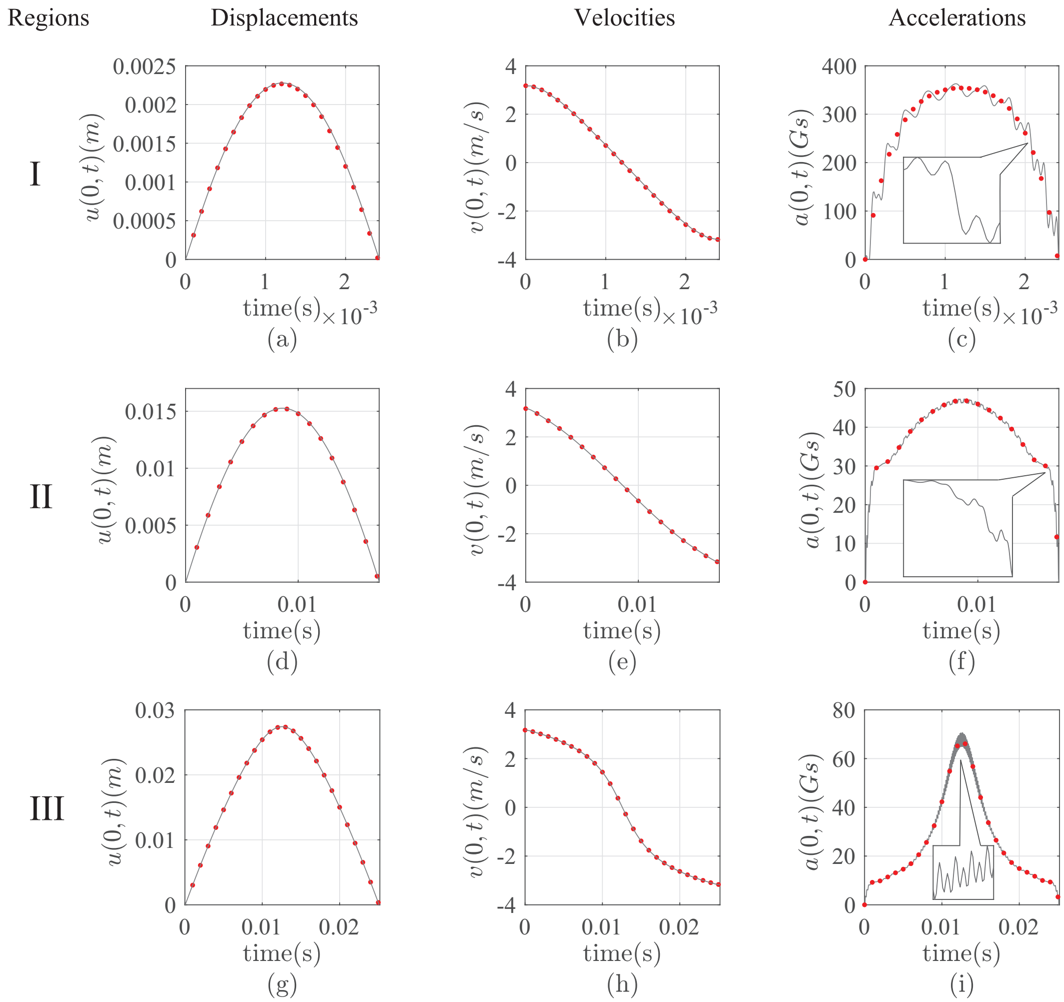

Figure 2.5. Impact response using static stresses in the three regions of quasi-static stress curve for $H/L = 16$. Dots are for 1-mode and solid lines are for 3-mode estimations. Static stress in Region I is 0.4 kPa, Region II is 5 kPa, and Region III is 15 kPa: (a) compressive deformation in Region I, (b) velocity in Region I, (c) acceleration in Region I, (d) compressive deformation in Region II,(e) velocity in region II, f) acceleration in Region II including its zoomed out view, g) compressive deformation in Region III, h) velocity in Region III, and (i) acceleration in Region III . The inserts contains zoomed views to see the effects of including multiple modes.

of damping in Eqn. (2.37). The effect of damping can be clearly seen by plotting the relative error between the energy based and numerical estimated cushion curves with experimental data, Fig. 2.8.

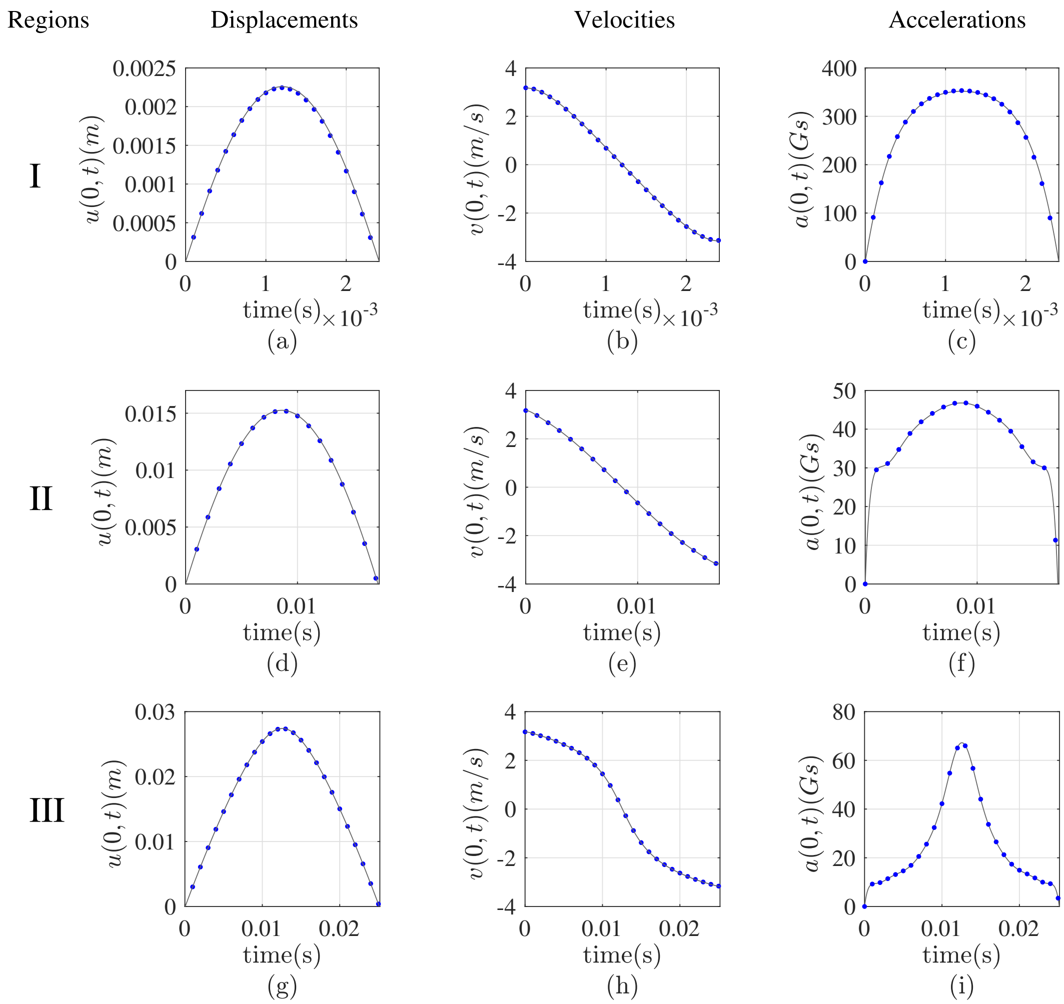

Figure 2.6. Impact response using static stresses in the three regions of quasi-static stress curve for $H/L = 16$ and damping $\zeta = 0.012$. Dots are for 1-mode and solid lines are for 3-mode estimations. Static stress in Region I is 0.4 kPa, region II is 5 kPa, and Region III is 15 kPa: (a) compressive deformation in Region I, (b) velocity in Region I, (c) acceleration in Region I, (d) compressive deformation in Region II, (e) velocity in Region II, (f) acceleration in Region II including its zoomed out view, (g) compressive deformation in Region III, h) velocity in Region III, and (i) acceleration in Region III.

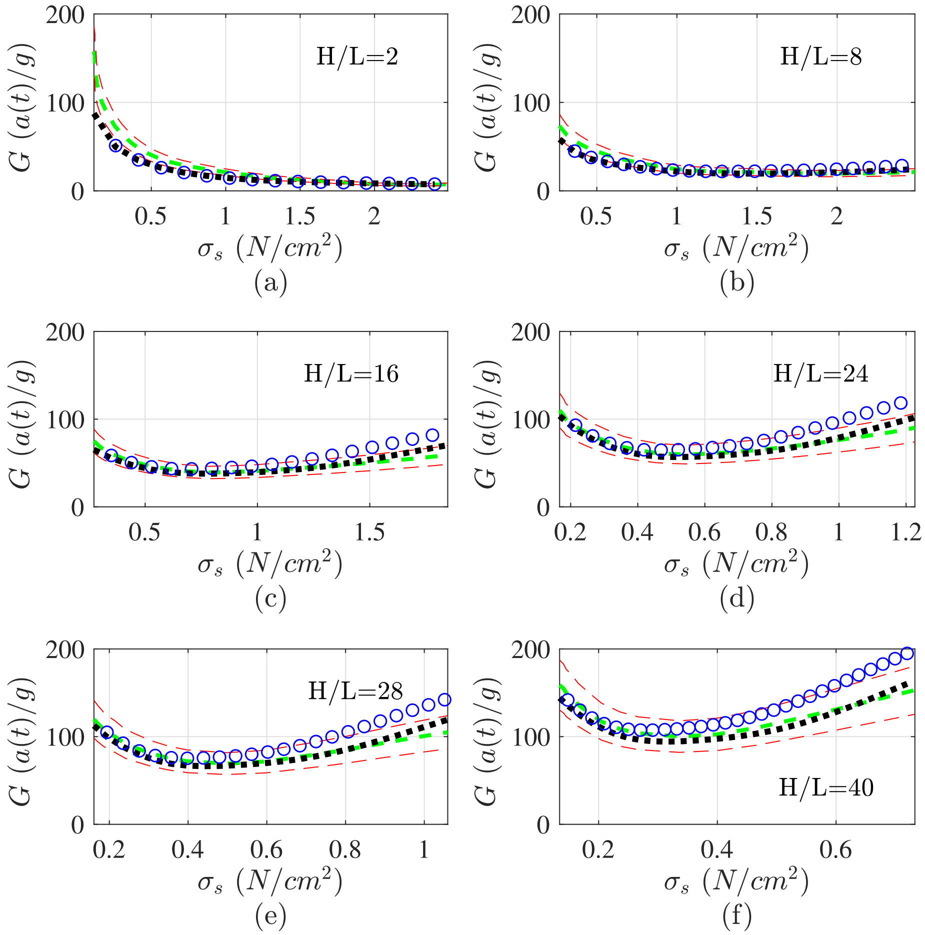

Figure 2.7. Estimates of cushion curves considering a damping ratio, $\zeta = 0.012$, for $H/L = 2, 8, 16, 24, 28,$ and 40. Circular blue dots indicate energy based estimation (undamped), black dots indicate numerical integration estimation (damped), and green dash lines are experimental data. Red dashes indicate $\pm 18\%$ bounds.

The introduction of damping in Eqn. (2.37) yields notable improvement in the agreement between the experimental and predicted cushion curves as seen in Fig. 2.7. This improvement can be clearly seen by plotting the relative error between both the analytical energy based (no damping) and numerical (damped) cushion curves and the experimentally determined cushion curves, see Fig. 2.8. Note that with the exception of small regions in the cushion curves for H/L equal to 2 and 8, the

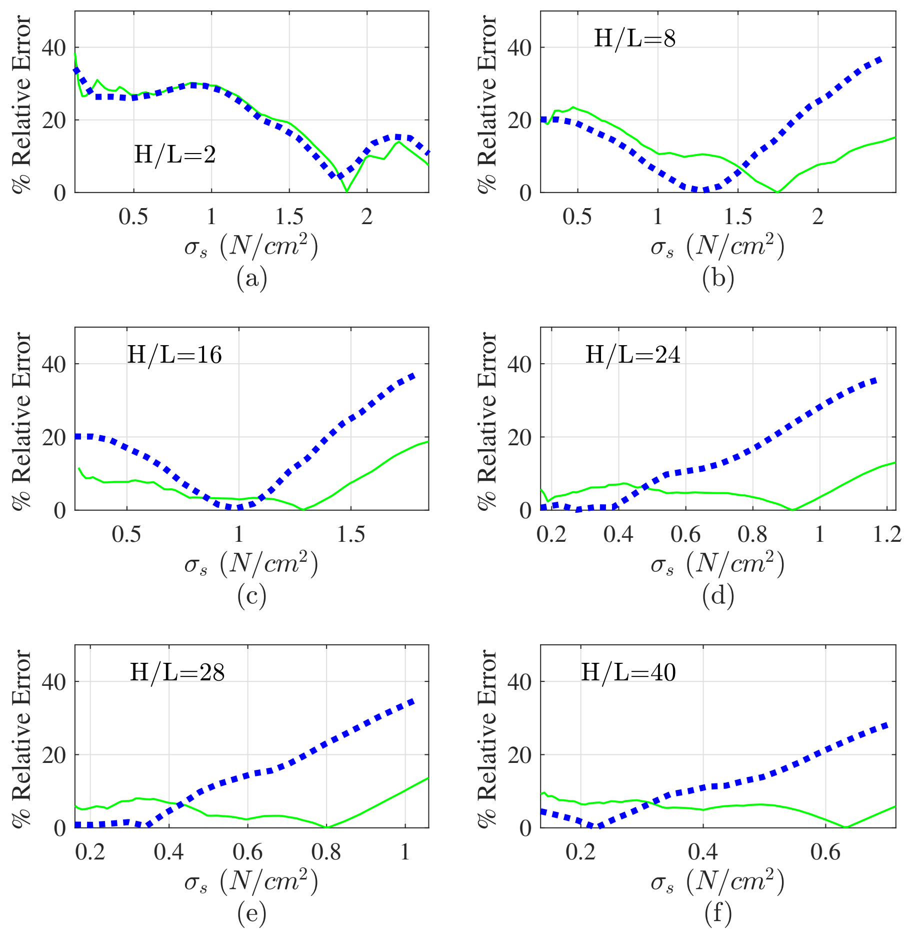

Figure 2.8. Comparison of the relative errors for $H/L = 2, 8, 16, 24, 28$, and 40. Blue dots indicate error between energy balance predictions (no damping) and experimental data, green lines indicate the relative error between numerical predictions (with damping) and the experimental data.

damped data is within the 18% lab to lab variability. However, the linear damping does not completely approximate the viscoelastic loss mechanism and has only a second order effect in determining the shape of the cushion curve based on the quasi static description of stress. It is also worth noting that the polynomial stress-strain relationship, σ_p, is not a purely hyperelastic description of the material behavior, since the material is viscoelastic, testing the material at slightly different quasi static strain rates will produce slightly different polynomial expressions.

We have shown that the material behavior can be adjusted to represent the impact response by calibrating the model using a viscous damping coefficient predicted from the shock pulse. This approach works well, since the dynamic stress -strain relationship [21] does not significantly deviate from the quasi-static stress-strain relationship in the polystyrene foam [29].

2.5.3 Experimental Shock Pulse Prediction

The ability of the model developed to accurately predict a set of cushion curves has been demonstrated through comparison to experimental cushion curve data. An additional experiment is conducted to further validate the model and its ability to predict the shock response of a mass impacted cushion sample in the time domain. An expanded polyethylene foam material, Ethafoam® 150 (Sealed Air Corporation) is used for this experiment. The stress-strain behavior of Ethafoam® 150 is characterized using a Satec Universal Tester - T10000 (Instron Corporation) following the procedure outlined in the previous work by Batt et al. [63–65]. A polynomial was fit to the average of the data sets collected and the polynomial coefficients are listed in Table 2.2.

The time domain, acceleration response of the cushion material is generated using a cushion tester (Lansmont Corporation). A 20.6 kg platten is dropped from a height of 59.5 cm and vertically impacts a $15 \times 15.1 \times 5.6$ cm sample. The model developed with a damping ratio of $\zeta = 0.13$ is used to predict the resulting shock pulse. The pulse predicted is compared to the low-pass filtered shock pulse from the cushion tester, Fig. 2.9.

There is excellent agreement between the model predicted pulse and the filtered experimental pulse in both frequency and amplitude, see Fig. 2.9. This is the first time in literature that this level of accuracy in predicted cushion impact performance has been demonstrated with a continuous model. Impact characterization of cushion materials is historically a time intensive, experimental process, requiring thousands of impacts to account for different drop heights, cushion thicknesses, and static stresses [66]. The use of such a model, identified from only the material's stress-strain behavior and a single shock pulse, can significantly reduce the time and cost of characterizing the impact response of a given material.

Table 2.2. Modulus and relative moduli for uniaxial compression polynomial model of Ethafoam® 150.

E_1	0.454 MPa	E_5	490.776 MPa / MPa
E_2	-12.741 MPa / MPa	E_6	-438.998 MPa / MPa
E_3	83.558 MPa / MPa	E_7	157.173 MPa / MPa
E_4	-277.471 MPa / MPa		

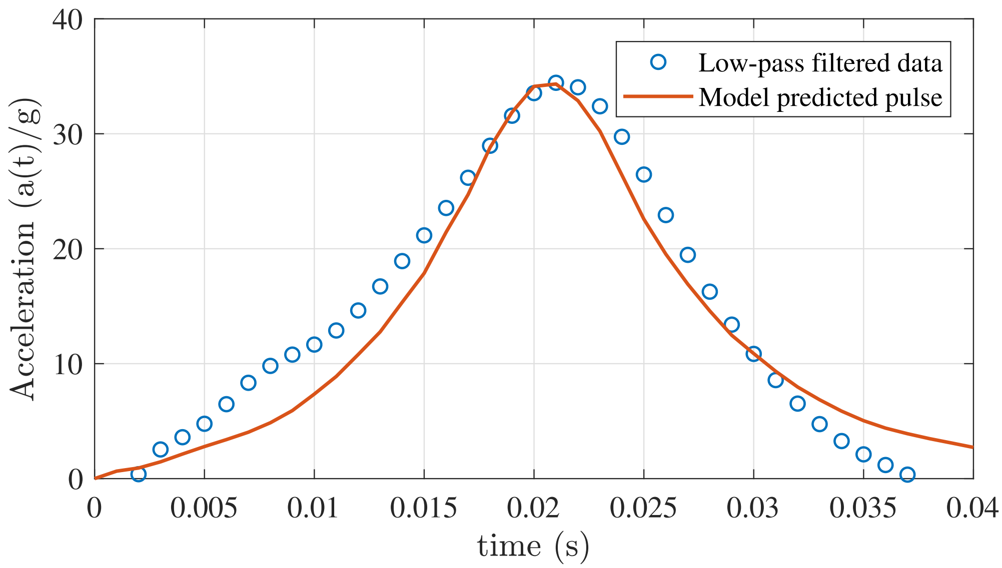

Figure 2.9. Low-pass filtered experimental acceleration pulse compared with the present model pulse for static stress of 8.9 kPa and $H/L = 10.6$.

2.6 Chapter Summary

This chapter modeled the dynamics of a falling platten impacting a foam cushion as a nonlinear rod with an end mass subject to an initial velocity. It departed from the lumped parameter paradigm that is typically used to determine cushion response. The nonlinearities are a result of the hyperelastic material describing the foam's stress-strain behavior. Both the nonlinearity and the viscoelasticity are modeled with polynomial constitutive relationship combined with a Kelvin-Voight model of damping. The model is used to generate acceleration waveforms during impact, and by varying static stresses, one can generate a set of cushion curves. Ignoring damping and using a single mode approximation allows analytical estimates of the cushion curve based on an energy balance approach. The energy balance estimation, while predicting the overall shock characteristics of the foam, under predicts the peak acceleration at lower drop heights and static stresses and over predicts higher drop heights and static stresses. Furthermore, the energy based estimation is limited to materials for which the dynamic stress and quasi-static stress versus strain responses are similar in shape and magnitude. Including damping in the model and solving the governing equations of motion numerically improves cushion curve prediction. It is worth noting that the both un-damped and damped predicted impact shock responses are in agreement with experimental results, and the latter closely matches.

In the next chapter we introduce a metamaterial with a specific geometry that mimics the material behavior of the foams presented here.

3. EXTENDED χ STRUCTURE

In the proceeding chapter of the shock response of foam several key insights can be obtained. First, the effect of higher order modes are smaller in the shock response. Second, both damping and nonlinear elastic deformation also play a role in governing shock absorbing behavior. This observation is underscored when one realizes that the presence of Region II in the constitutive relations coincided with minimal rebound acceleration. Note that in Region II the effective modulus in this zone of stress and strain is nearly zero, i.e., it has quasi-zero modulus. Furthermore, we will show in this section the effective nonlinear material behavior can be influenced by the topology of an architected material.

3.1 Background

One particular metamaterial geometry that exhibits quasi-zero modulus or equivalently quasi-zero stiffness (QZS) is an χ shaped topology first proposed by Bunyan et al. [11]. In its initial realization the mechanical metamaterial was fabricated out of polyurethane rubber and composed of unit cells containing a network of beams arranged in a geometric configuration of two opposing triangles attached at their apex, resembling the letter "X", Fig 3.1 (a). Mimicking cellular foams the unit cell of the material exhibited three distinct regions of quasi-static stress under uniaxial compression [5, 62]. Region I occurs between 5-10% nominal strain; and is characterized by local linear compression of the horizontal members, and axial compression of the diagonal members. At the apex of this region, the members experience buckling. The plateau region, II, is typically defined to occur at 10-60% strain. This region is the onset of buckling. Region III occurs past the plateau and is known as the densification region. In this region the members of the members of the structure self contact leading to a region of high resistive force and stiffness.

Furthermore, Bunyan and Tawfick [11] noted that the relative height and width of the unit cell changed the average stiffness of the structure, the width of the plateau region, and the energy absorption of the structure; the area under the force-displacement curve. Helou and Harne [67] extended the research by studying layers of χ unit cells to develop a framework to control the collapse of layers in a functionally graded elastomeric structures based on this topology. This is achieved by tailoring the beam thickness in each layer.

However, both studies [11, 67] due to their rigid adherence to the χ topology neglected to consider a fundamental question that is: In a fixed volume for a given material, can the behavior of the unit cell be changed by manipulating the topology of the unit cell, i.e., the relative orientation and length of the members? It is with these limitations in mind, the present work proposes a modification to the original topology by expanding the design space to include the vertical neck that connects the apexes. This configuration is dubbed the extended χ configuration.

Considering the preceding discussion, the remainder of this chapter presents the fabrication, material testing and finite element modeling of a χ unit cell.

3.2 Fabrication and Testing

A combination of experiments and numerical analysis is used to first examine the behavior of the extended χ shaped elastomeric structure. The structures studied in this work are fabricated by casting a platinum cure two part silicone rubber (Smooth-On Mold Star 15S) in polylactic acid (PLA) thermoplastic negative molds. The models are produced on a fused deposition 3D printer (Ultimaker S5). The rubber is cured for two hours at 50 °C in a Print Dry filament dryer and then allowed to aerate for 24 hours. The samples are tested by Mark 10 ESM 1500 electromechanical load frame with a load capacity of 6700 N (1500 lbF). In the tests, the frame is equipped

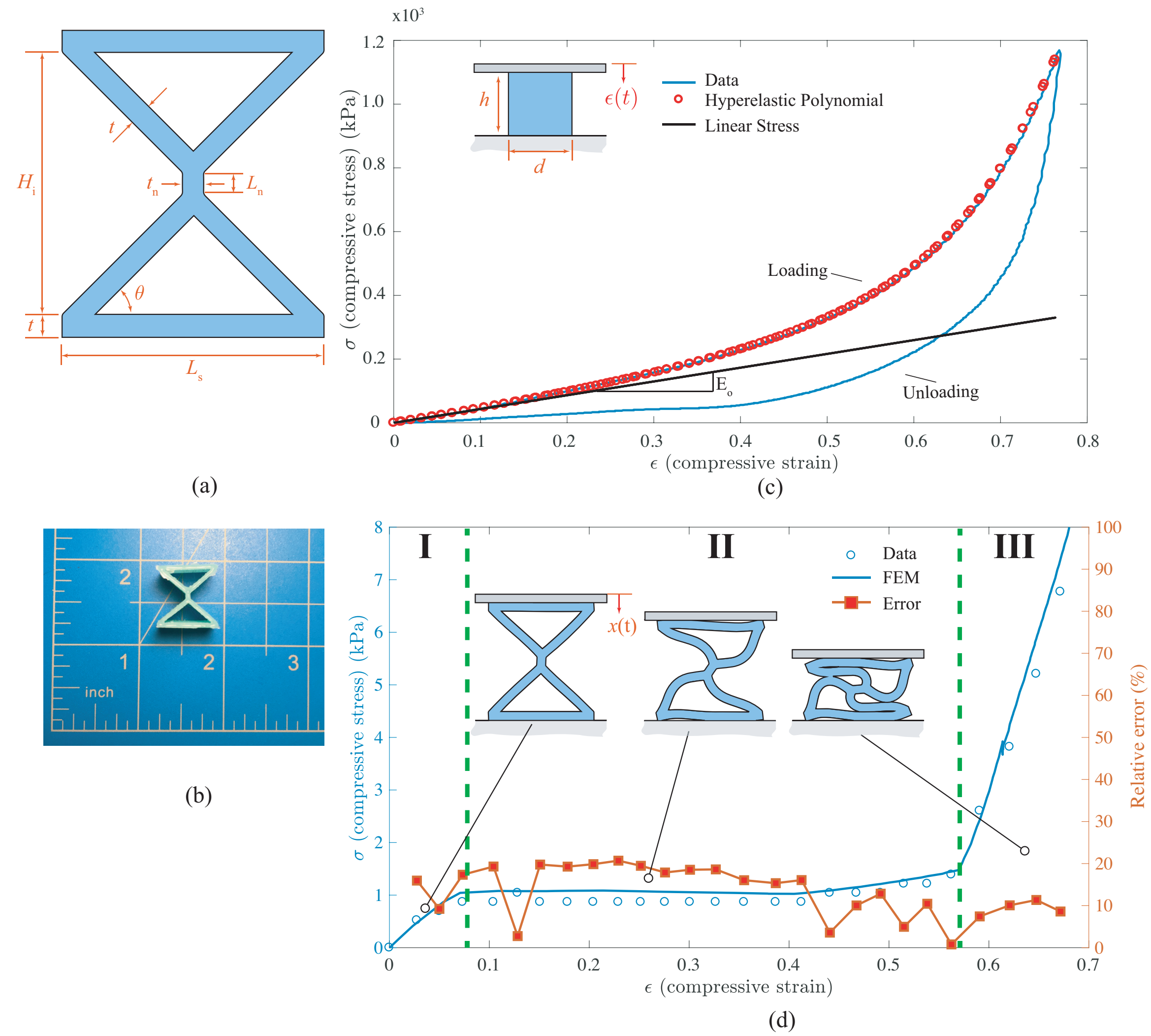

Figure 3.1. Extended χ Shaped Unit Cell: (a) Schematic of extended χ structure with annotated dimensions. The tested dimensions are $L_s = H_i = 24$ mm, $t = t_n = L_n = 2$ mm, and $\theta = 45°$. (b) Photo of fabricated unit cell. (c) Compressive behavior of test coupon at 10 mm/s loading rate. The dimensions of the test cylinder are $d = 29$ mm, $h = 13$ mm. Red dot indicates hyperelastic polynomial fit and black line indicates initial linear fit. (d) Plot of the compressive behavior of unit cell at 10 mm/s loading rate, along with FEM predictions and relative error between model and experimental data. Inserts show the simulated FEM response in the three phases of deformation: I) linear elastic region, II) asymmetric buckling of unit cell giving rise to region of quazi-zero-modulus, and III) large tangent modulus region due to self contacting members.

with a Mark 10 MR01-50 load cell that has a 250 N (50 lbf) capacity and a 0.1 N (0.02 lbf) resolution.

3.2.1 Finite Element Model

The structure was simulated in ABAQUS using a Dynamic-Implicit analysis with a CPS4R element with hyperelastic material behavior that is described by the polynomial strain energy density function. The material properties are directly imported from experimental stress-strain results. Using the imported data and hyperelastic model in Material module in ABAQUS, the coefficients are obtained automatically for a polynomial model of hyperelasticity. The extended χ structure was placed between two discrete rigid wire parts with surface contact. In addition, self contact properties are defined in the normal and tangential directions for the elements on the members' edges as hard contact and tangential contact with penalty coefficient of 1, respectively. The analysis is displacement controlled; the top surface is allowed to move until the χ structure has been compressed to 70% of its original height. A small perturbation force (0.01 to 0.05 N depending on the geometry) directed to right or left, is applied to the middle to initiate the asymmetric buckling instability in deformation.

3.3 Material Response

Figure 3.1 (c) shows the stress-strain curve of a cylinder in uniaxial compression. The cylinder has dimensions $d = 29$ mm and $h = 13$ mm. The tests were conducted in accordance with ASTM D395-18 [68]. The test is displacement controlled with the load frame set to compress the specimen to 75% of its uncompressed height. The material exhibits a nonlinear constitutive behavior and a considerable amount of hysteresis from the loaded and unloaded configurations. A second order polynomial [69] strain energy density function approximates the loading experimental uniaxial compression response with a modified coefficient of determination of 0.92. Appendix C provides the procedure for calculating the coefficients for the polynomial hyperelasticity. The material constants for the model are $C_{10} = 28605.48$ Pa, $C_{01} = 43465.27$ Pa, $C_{20} = -17629.01$ Pa, $C_{02} = -1252.43$ Pa, and $C_{11} = 7279.86$ Pa. This yields an initial shear modulus of 144.14 kPa and initial tangent modulus of $E_0 = 432.42$ kPa (See Appendix C). In addition, we see that the material exhibits a significant amount of hysteresis under a large deformation. This indicates that similar to the foams in Chapter 2, the material is viscoelastic in nature. It is worth noting that a sensitivity analysis examining the effect of the material parameters on the finite element model was not performed.

3.4 Quasi-Static Unit Cell Response

In this section, we examine the response of an elastomeric extended χ unit cell. Figure 3.1 (a) is a schematic extended χ structure with annotated dimensions and Fig. 3.1 (b) is a photo of the fabricated unit cell. The cell is a rectangle of outer width, L_s, and inner height, H_i, and contains two equilateral triangles connected at their respective apexes by a member with width, t_n, and length, L_n. The base angle of each equilateral triangle is denoted as θ. The dimensions are arbitrarily specified as $L_s = H_i = 24$ mm, $t = t_n = L_n = 2$ mm, and $\theta = 45°$.

Figure 3.1 (d) plots an effective stress-strain relationship of the unit cell. The effective strain and stress are defined as

$$\bar{\sigma} = \frac{F}{A_{TS}} \quad \text{and} \quad \bar{\epsilon} = \frac{x_T}{H_i}, \tag{3.1}$$

where F is the force on the structure, A_{TS} is the area of the top surface of the structure, x_T is the displacement of the platten contacting the structure, and H_i is the inner height of the unit cell, neglecting the thickness of the bottom and top legs. The deformation has three stages: I) before buckling, II) asymmetric buckling, and III) self contact where hardening starts, see insert in Fig 3.1 (d). Note that the FEM model captures the general trend of the nonlinear response of the experimental specimen.

The model predicts the onset of the three distinct regions of deformation; however, there is roughly a 20% maximum relative difference in compressive strain between the model and the experimental results. The sources of this differences are: (1) the imperfections in the sample such as raised small air bubbles during solidification and tiny damages during demolding, (2) approximate contact parameters in FEM, between the legs in the extended χ structure and between the legs and the rigid compressors, and (3) approximate hyperelastic material model in FEM.

3.5 Response of Extended χ Structure Due to Cyclic Loading at Various Compression Rates

The unit cell is compressed use the aforementioned Mark-10 test frame under displacement control at compression rates of 10, 20, 100 and 200 mm/s for four cycles. Visually, the hysteresis loop is narrower at the lowest compression rate of 10 mm/s and widens at a rate of 200 mm/s. Note that base material exhibited a significant amount of hysteresis indicated by the unloading curve deviating significantly from the loading curve in Fig 3.1 (b). However, the unit cell does not exhibit the same amount of hysteresis, Fig 3.2. Arguably, at these strain rates the effect of hysteresis is negligible.

3.6 Influencing the Linear and Quasi-Zero Modulus Regions

Examining the deformation of the structure can lead to the hypothesis that an increase in the region of quasi-zero modulus region can be obtained by increasing the height, H_i, of the structure while fixing its width, L_s. This can be understood by realizing that elongating the legs and neck will make them more susceptible to buckling. Another option is to keep the effective area of the unit cell ($L_s \times H_i$) fixed and change the local topology, i.e., θ or equivalently the length of the neck, L_n. Figure 3.3 compares these two cases with unit cells having: 1) $\theta = 42.5°$ that provides $L_n = 3.8$ mm, and 2) $\theta = 47.5°$ (without neck). It clearly shows that adding a neck

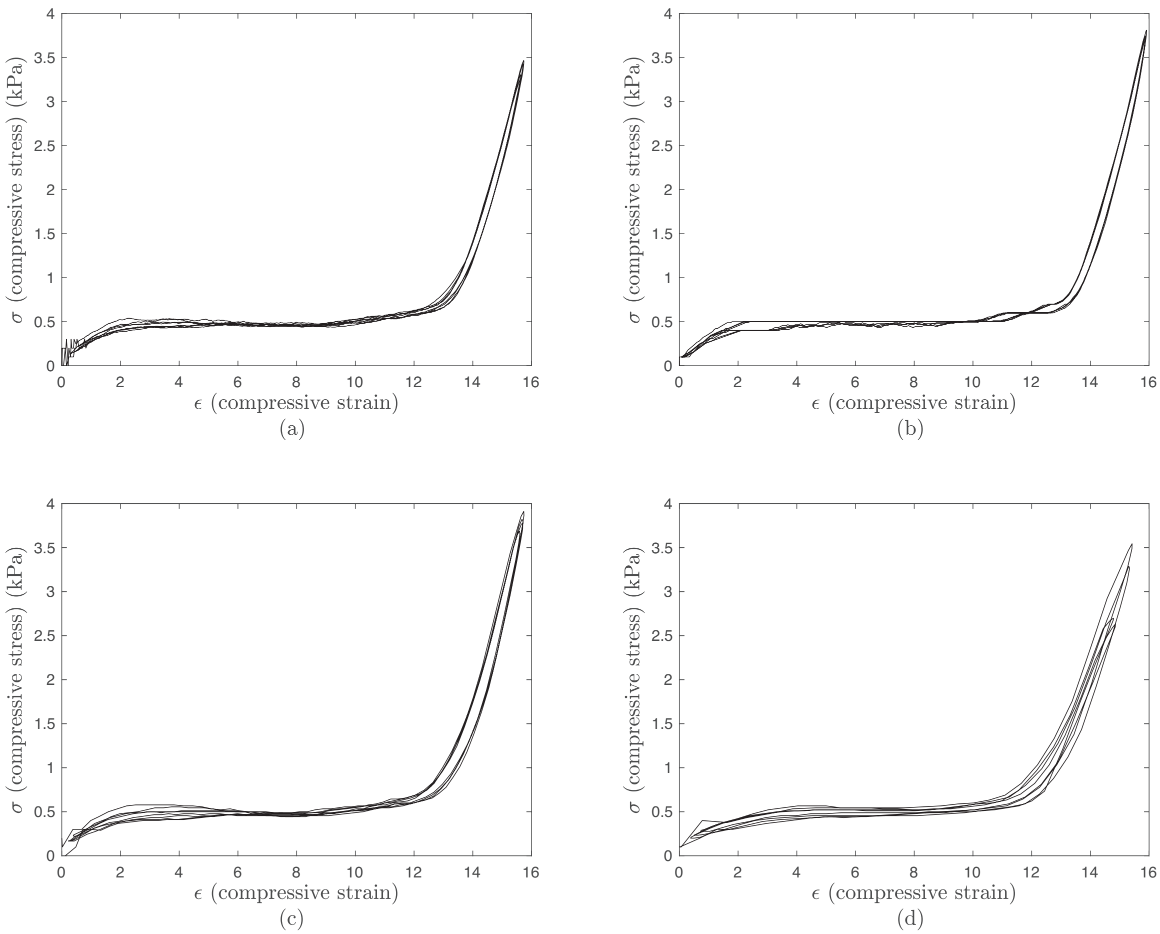

Figure 3.2. Compressive testing for the extended χ with 4 cycles at various compression rates: (a) 10 mm/s, (b) 20 mm/s, (c) 100 mm/s, and (d) 200 mm/s. The dimensions of the unit cell are: $L_s = H_i = 24$ mm, $t = t_n = L_n = 2$ mm, and $\theta = 45°$.

postpones the densification region. By adding the neck, the self contact is postponed by distancing upper legs and lower legs. This is not without a trade off; the changes in topology causes the linear region of the effective stress and strain to increase.

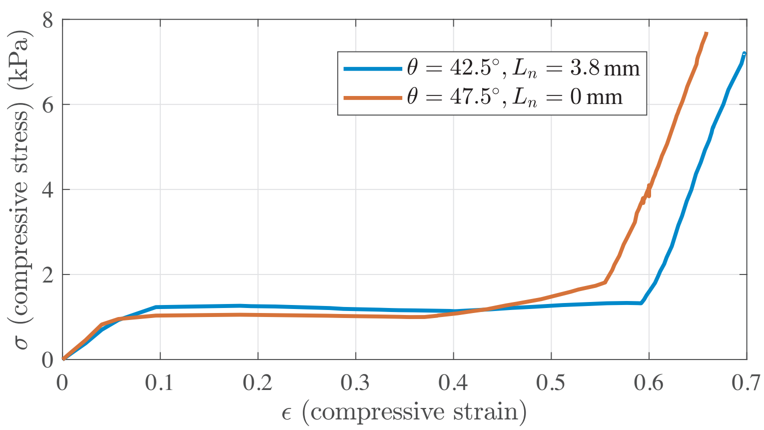

Figure 3.3. Extended χ structure at values of L_n of 3.8 mm an 0.0 mm.

3.7 Chapter Summary

This chapter has provided an overview of both the material and unit cell response. The unit cell is dubbed the extended χ structure due to it "X" shaped topology. This unique topology yields an effective stress-strain relationship that resembles that of polymer foams. The next chapter will focus on Region I of the response, in particular the effects of topology on buckling through a combination of semi-analytical and finite element modeling.

4. MODELING LINEAR BUCKLING OF EXTENDED χ

In this chapter a linear, semi-analytical model of buckling for the extended χ structure is developed. The structure is modeled as seven Euler Bernoulli beams that are rigidly connected. It is assumed that the beams are slender and that the contribution of the shear forces can be neglected. In examining the extended χ structure the onset of buckling of the structure ends the linear force-displacement region, Region I equivalent of a polymer foam, and begins the quasi-zero stiffness region, ie., the equivalent Region II of a polymer foam. Understanding the geometric parameters that define this region are essential in customizing the material response.

The model is based on the stiffness matrix of a beam-column where equilibrium conditions are imposed at each joint to determine the critical load and the corresponding modes. The chapter begins by deriving the Euler-Bernoulli equation for a beam in buckling. Next, the resulting equations are used to model the extended χ structure. Finally, the results are validated against a finite element model developed in ABAQUS for a given unit cell geometry. The models presented in this section are a departure from previous work [11,67] that relied primarily on finite element analysis to model a complete cyclic loading, and neglected the buckling analysis of the unit cell.

4.1 Euler-Bernoulli Beam Buckling

The section presents a simplified model to determine the buckling behavior of the extended χ structure. In addition, it presents two finite element models that are used to verify the validity of this model.

The unit cell extended χ structure can be viewed as a set of interconnected plates; however, Bunyan and Tawfick [11] showed that a beam based FEM approximation provides a reasonable estimate of its response due to a compressive load. Therefore, we will assume that an Euler Bernoulli beam will approximate the buckling behavior of each member of the structure. The equilibrium equation for an elastically buckled Euler-Bernoulli beam, Fig. 4.1, under axial loads P, shear end loads V_1 and V_2, and end moments M_1 and M_2 can be written as [70, 71]

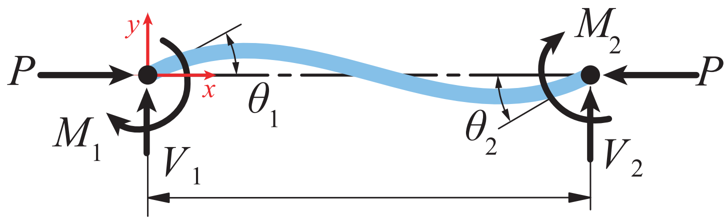

Figure 4.1. Beam in buckling subject compressive end loading, P. The undeformed position is indicated by dotted line.

$$\frac{d^2y}{dx^2} + \frac{P}{EI}y = -\frac{M_1}{EI}\left(1 - \frac{x}{L}\right) + \frac{M_2}{EI}\frac{x}{L}, \tag{4.1}$$

where E, I, and L are the modulus of elasticity, the second moment of inertia, and the beam length respectively. The solution for $y(x)$ can be written as

$$y(x) = A\sin(kx) + B\cos(kx) - \frac{M_1}{P}\left(1 - \frac{x}{L}\right) + \frac{M_2 x}{PL}. \tag{4.2}$$

Assuming the beam does not sway, i.e, the beam does not undergo transverse displacement and rigid body rotations at its ends then the constants A and B can be obtained as

$$A = -\frac{M_1}{P}\cot(kL) - \frac{M_2}{P}\csc(kL), \quad B = \frac{M_1}{P}, \tag{4.3}$$

where $k^2 = P/EI$. The first derivative of $y(x)$ in Eqn. (4.2) at $x = 0$ and $x = L$, equals θ_1 and θ_2 respectively. Eqn. (4.2) can be rearranged in terms of θ_1 and θ_2, M_1 and M_2 as

$$M_1 = \frac{EI}{L}(S\theta_1 + SC\theta_2), \quad \text{and} \quad M_2 = \frac{EI}{L}(S\theta_2 + SC\theta_1). \tag{4.4}$$

The functions S and C have different forms depending on whether the axial force P is compressive or tensile. When P is compressive the functions S and C can be written as

$$S = \frac{\lambda(1-\lambda\cot(\lambda))}{2\tan(0.5\lambda)-\lambda}, \quad C = \frac{\lambda\csc(\lambda)-1}{1-\lambda\cot(\lambda)}, \quad \text{where} \quad \lambda = kL. \tag{4.5}$$

When P is tensile the solution to Eqn. 4.2 is in terms of hyperbolic functions and not trigonometric functions, then S and C have the following form

$$S = \frac{\lambda(\lambda\cosh(\lambda)-\sinh(\lambda))}{2-2\cosh(\lambda)+\lambda\sinh(\lambda)}, \quad C = \frac{\sinh(\lambda)-\lambda}{\lambda\cosh(\lambda)-\sinh(\lambda))}, \quad \text{where} \quad \lambda = kL. \tag{4.6}$$

Finally, if $P = 0$, the solution to Eqn. 4.2 is cubic polynomial and in this case C and S are $\frac{1}{2}$ and 4. In the next section, a static analysis will reveal that the extended χ structure contains both compressive and tensile members.

4.1.1 Statics of Extended χ Structure under Concentrated Forces

In this section, we approximate the loads from either an experimental vertical compression from material testing or an impact as four concentrated forces of f, applied on the endpoints of legs AB, EF as shown in Fig. 4.2. In developing the model we assume, members at A, B, C, D, E, and F are rigidly connected and the

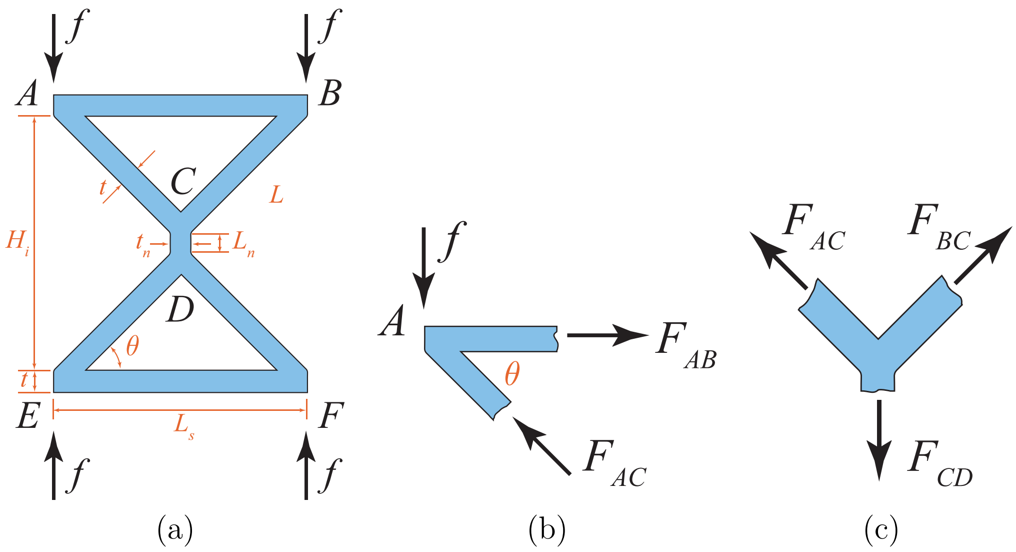

Figure 4.2. Extended χ subject to four concentrated compression loads of magnitude f: (a) fully freebody diagram of the structure, (b) and (c) freebody diagram of isolated joints.

effects of shear are negligible. Static equilibrium dictates the following relationship between internal and external forces,

$$
\begin{aligned}
&F_{AC} = f \csc\theta, \quad F_{AB} = f \cot\theta, \\
&F_{CD} = 2f, \quad F_{BC} = F_{DE} = F_{DF} = F_{AC}, \quad F_{EF} = F_{AB}.
\end{aligned} \tag{4.7}
$$

Clearly the angle θ influences the internal forces. We will heretofore refer to θ as the characteristic angle of the unit cell. In addition, the normal forces in horizontal legs AB and EF are tensile and have the same magnitude, $f \cot\theta$. The normal forces in legs AB, AC, DE, DF are compressive and have the same magnitude, $f \csc\theta$. The "neck" of the structure, member CD, has a compressive internal force of $2f$ and experiences a large portion of the load.

4.1.2 Buckling of Extended χ Structure

Now, the internal forces can be defined in terms of the applied forces and the geometry of the structure can be defined in terms of the angle θ, and leg length L. In analyzing the buckling behavior, consider the extended χ structure in equilibrium is disturbed in such a manner that gives rise to moments and deformations, Fig. 4.3. The slope at the endpoints of each leg is denoted as follows:

$$\theta_{ij} = \frac{dw_{ij}}{dx}, \quad \text{where } (ij) = (AB),\ (AC),\ (BC),\ (CD),\ (DE),\ (DF), (EF), \tag{4.8}$$

and

$$\theta_{ji} = \frac{dw_{ji}}{dx}, \quad \text{where } (ji) = (BA),\ (CA),\ (CB),\ (DC),\ (ED),\ (DF), (FE). \tag{4.9}$$

Using Eqns. (4.5), (4.6) and Eqn. (4.4) the moments on the ends of each leg can be written in terms of the slopes of the each respective leg as

$$M_{AB} = \frac{EI}{L_{AB}}(S_{AB}\theta_{AB} + S_{BA}C_{BA}\theta_{BA}), \quad M_{BA} = \frac{EI}{L_{BA}}(S_{BA}\theta_{BA} + S_{AB}C_{AB}\theta_{AB}), \tag{4.10a}$$

$$M_{AC} = \frac{EI}{L_{AC}}(S_{AC}\theta_{AC} + S_{CA}C_{CA}\theta_{CA}), \quad M_{CA} = \frac{EI}{L_{CA}}(S_{CA}\theta_{CA} + S_{AC}C_{AC}\theta_{AC}), \tag{4.10b}$$

$$M_{BC} = \frac{EI}{L_{BC}}(S_{BC}\theta_{BC} + S_{CB}C_{CB}\theta_{CB}), \quad M_{CB} = \frac{EI}{L_{CB}}(S_{CB}\theta_{CB} + S_{BC}C_{BC}\theta_{BC}), \tag{4.10c}$$

for the upper portion of the structure, and

$$M_{CD} = \frac{EI}{L_{CD}}(S_{CD}\theta_{CD} + S_{DC}C_{DC}\theta_{DC}), \quad M_{DC} = \frac{EI}{L_{DC}}(S_{DC}\theta_{DC} + S_{CD}C_{CD}\theta_{CD}), \tag{4.11}$$

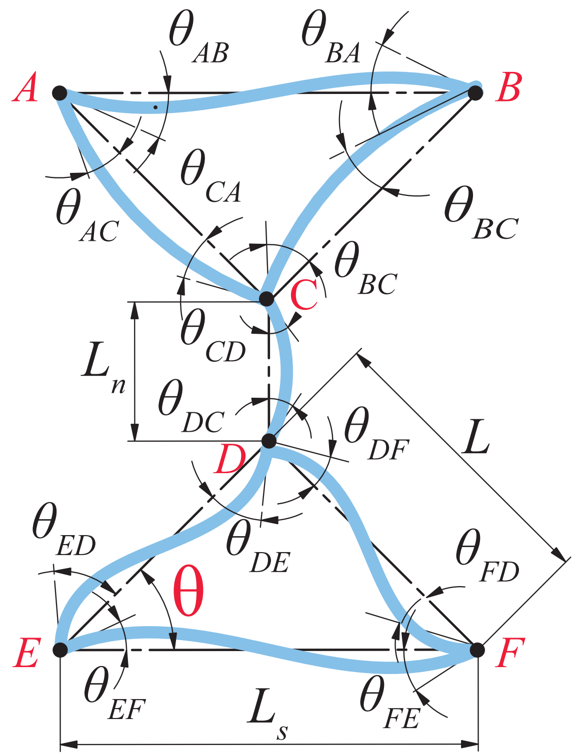

Figure 4.3. Deformation of buckled extended χ under concentrated compression loads.

for the neck, and

$$M_{DE} = \frac{EI}{L_{DE}}(S_{DE}\theta_{DE} + S_{ED}C_{ED}\theta_{ED}), \quad M_{ED} = \frac{EI}{L_{ED}}(S_{ED}\theta_{ED} + S_{DE}C_{DE}\theta_{DE}), \tag{4.12a}$$

$$M_{DF} = \frac{EI}{L_{DF}}(S_{DF}\theta_{DF} + S_{FD}C_{FD}\theta_{FD}), \quad M_{FD} = \frac{EI}{L_{FD}}(S_{FD}\theta_{FD} + S_{DF}C_{DF}\theta_{DF}), \tag{4.12b}$$

$$M_{EF} = \frac{EI}{L_{EF}}(S_{EF}\theta_{EF} + S_{FE}C_{FE}\theta_{FE}), \quad M_{FE} = \frac{EI}{L_{FE}}(S_{FE}\theta_{FE} + S_{EF}C_{EF}\theta_{EF}), \tag{4.12c}$$

for the lower portion of the structure, where

$$k = k_{AC} = k_{BC} = k_{DE} = k_{DF}, \tag{4.13}$$

$$k_{AB} = k_{EF} = k\sqrt{\cos\theta}, \tag{4.14}$$

$$k_{CD} = k\sqrt{2\sin\theta}, \tag{4.15}$$

the constant $k = \lambda/L$. Finally, we note the following geometric relationships between the legs and neck of the structure

$$\begin{aligned} &L = L_{AC} = L_{BC} = L_{DE} = L_{DF}, \quad L_{AB} = L_{ED} = 2L\cos\theta, \\ &\text{and} \quad L_{CD} = H_i - 2L\sin\theta. \end{aligned} \tag{4.16}$$

According to equilibrium of moments on points A, B, C, D, E, and F, we have

$$\begin{aligned} &M_{AB} + M_{AC} = 0, \\ &M_{BA} + M_{BC} = 0, \\ &M_{CA} + M_{CD} + M_{CB} = 0, \\ &M_{DC} + M_{DE} + M_{DF} = 0, \\ &M_{ED} + M_{EF} = 0, \\ &M_{FD} + M_{FE} = 0. \end{aligned} \tag{4.17}$$

The legs are assumed to be rigidly connected [71]. Therefore,

$$\begin{aligned} &\theta_{AB} = \theta_{AC} = \theta_A, \quad \theta_{BA} = \theta_{BC} = \theta_C, \\ &\theta_{CA} = \theta_{CB} = \theta_{CD} = \theta_C, \quad \theta_{DC} = \theta_{DE} = \theta_{DF} = \theta_D, \\ &\theta_{ED} = \theta_{EF} = \theta_E, \quad \text{and} \quad \theta_{FE} = \theta_{FD} = \theta_F. \end{aligned} \tag{4.18}$$

Substituting Eqns. (4.10a) to (4.10c), (4.11), (4.12c), and (4.18) in Eqns. (4.17), and canceling out EI/L factors, yields the matrix equation $\mathbf{A}\boldsymbol{\theta} = \mathbf{0}$ whose terms can be written as

$$\mathbf{A} = \begin{pmatrix} A_{11} & A_{12} & A_{13} & 0 & 0 & 0 \\ A_{21} & A_{22} & A_{23} & 0 & 0 & 0 \\ A_{31} & A_{32} & A_{33} & A_{34} & 0 & 0 \\ 0 & 0 & A_{43} & A_{44} & A_{45} & A_{46} \\ 0 & 0 & 0 & A_{54} & A_{55} & A_{56} \\ 0 & 0 & 0 & A_{64} & A_{65} & A_{66} \end{pmatrix}, \quad \boldsymbol{\theta} = \begin{pmatrix} \theta_A \\ \theta_B \\ \theta_C \\ \theta_D \\ \theta_E \\ \theta_F \end{pmatrix}, \text{ and } \mathbf{0} = \begin{pmatrix} 0 \\ 0 \\ 0 \\ 0 \\ 0 \\ 0 \end{pmatrix}, \qquad (4.19)$$

where

$$\begin{aligned}
A_{11} &= \frac{S_{AB}}{L_{AB}} + \frac{S_{AC}}{L_{AC}}, \; A_{12} = A_{21} = \frac{S_{AB}C_{AB}}{L_{AB}}, \; A_{13} = A_{31} = \frac{S_{AC}C_{AC}}{L_{AC}}, \\
A_{22} &= \frac{S_{AB}}{L_{AB}} + \frac{S_{BC}}{L_{BC}}, \; A_{23} = A_{32} = \frac{S_{BC}C_{BC}}{L_{BC}}, \\
A_{33} &= \frac{S_{AC}}{L_{AC}} + \frac{S_{BC}}{L_{BC}} + \frac{S_{CD}}{L_{CD}}, \; A_{34} = A_{43} = \frac{C_{CD}S_{CD}}{L_{CD}}, \\
A_{44} &= \frac{S_{CD}}{L_{CD}} + \frac{S_{DE}}{L_{DE}} + \frac{S_{DF}}{L_{DF}}, \; A_{45} = A_{54} = \frac{S_{DE}C_{DE}}{L_{DE}}, \; A_{46} = A_{64} = \frac{S_{DF}C_{DF}}{L_{DF}}, \\
A_{55} &= \frac{S_{DE}}{L_{DE}} + \frac{S_{EF}}{L_{EF}}, \; A_{56} = A_{65} = \frac{S_{EF}C_{EF}}{L_{EF}}, \\
A_{66} &= \frac{S_{DF}}{L_{DF}} + \frac{S_{EF}}{L_{EF}}.
\end{aligned}$$

Note that for a given geometry, the only unknown in $\mathbf{A}$ is the concentrated force, f or equivalently λ, leading to an eigenvalue problem. In order to find non-trivial solutions of $\mathbf{A}\boldsymbol{\theta} = \mathbf{0}$, the determinant of the $\mathbf{A}$ must equal zero, the values of λ (f) that satisfy this criteria are designated critical buckling loads f_{cr} of the structure. An analytical solution for λ (f) is either not possible or cumbersome. Therefore for a specified geometry (see Section 4.2) a numerical solution for λ (f) can be obtained.

This is done by evaluating the determinant over a range λ's and detecting when the determinant changes sign. The set of Λ can be written as

$$\Lambda = \{\lambda_0,\ \lambda_1\ \lambda_2, \cdots \lambda_{N-1}, \lambda_N\}, \quad \text{where} \quad \lambda_i = \lambda_i + \delta\lambda. \tag{4.20}$$

This zero crossing value in the set Λ is first estimate of the root and is then used as an initial guess for a root finding algorithm.

It is convenient to write the determinant of $\mathbf{A}$ as $D(\mathbf{A}) = |\mathbf{A}| = \phi_1(\lambda)\phi_2(\lambda)$ the functions, $\phi_1(\lambda)$ and $\phi_2(\lambda)$ are defined as

$$\phi_1(\lambda) = (S_{AB} - C_{AB}S_{AB} + 2S_{AC}\cos(\theta)), \tag{4.21}$$

and

$$\begin{aligned}\phi_2(\lambda) =&(-(1 + C_{AB})^2 S_{AB}^2((-1 + C_{CD})S_{CD} - 2S_{AC}\alpha)(S_{CD} + C_{CD}S_{CD} + 2S_{AC}\alpha)-\\ &2S_{AC}^2((1 + C_{CD})S_{CD} - 2(-1 + C_{AC}^2)S_{AC}\alpha)((-1 + C_{CD})S_{CD}+\\ &2(-1 + C_{AC}^2)S_{AC}\alpha) - 4(1 + C_{AB})S_{AB}S_{AC}((-1 + C_{CD}^2)S_{CD}^2+\\ &2(-2 + C_{AC}^2)S_{AC}S_{CD}\alpha + 4(-1 + C_{AC}^2)S_{AC}^2\alpha^2)\cos(\theta)-\\ &2S_{AC}^2((1 + C_{CD})S_{CD} - 2(-1 + C_{AC}^2)S_{AC}\alpha)((-1 + C_{CD})S_{CD}+\\ &2(-1 + C_{AC}^2)S_{AC}\alpha)\cos(2\theta))\sec(\theta)^4 \quad \text{where} \quad \alpha = L_{CD}/L_{AB}.\end{aligned}$$

The aforementioned numerical algorithm can be applied directly to $D(\mathbf{A})$ or the factorizations $\phi_1(\lambda)$ and $\phi_2(\lambda)$. Finally, the roots of λ can be written in terms of force where the force that yields a zero is denoted as f_{cr}. The critical values of λ/force correspond to a particular buckling mode shape. The total critical compression load is obtained as $F_{cr} = 2f_{cr}$. Solutions to $\phi_1(\lambda) = 0$ yields buckling modes that are symmetric about a vertical line passing through the structure and are labeled S^M for symmetric buckling modes. Similarly, solutions to $\phi_2(\lambda) = 0$ yields buckling modes that are antisymmetric about a vertical line passing through the structure and are

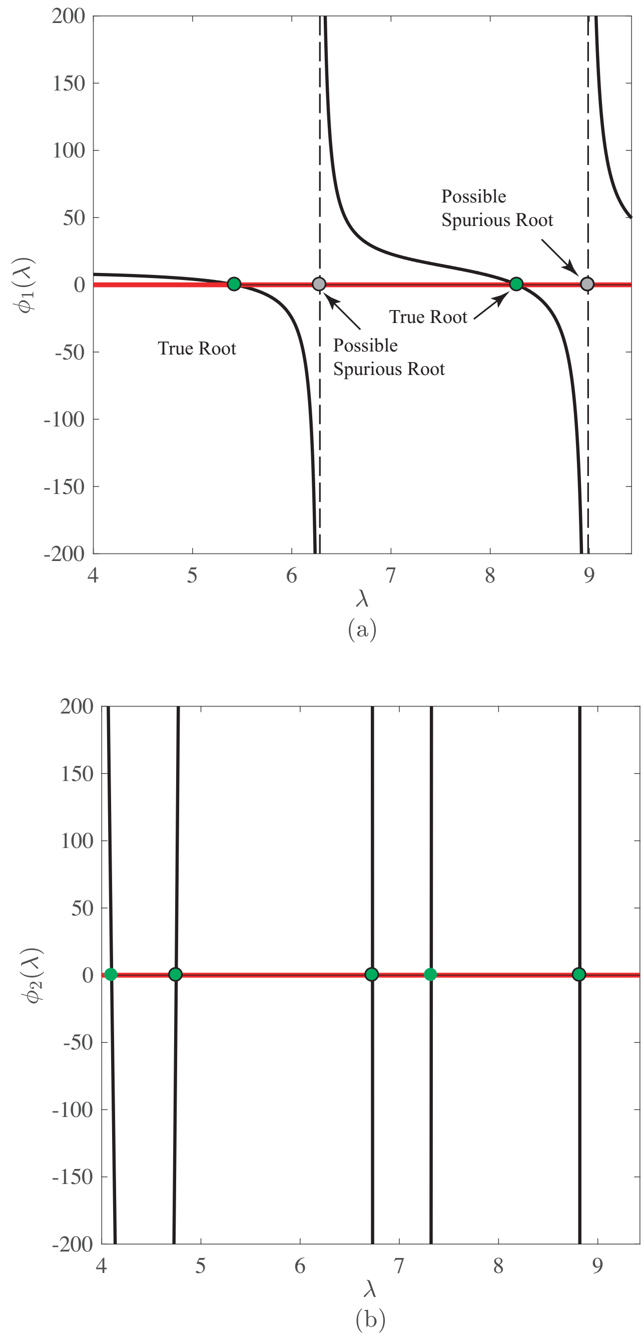

Figure 4.4. Components of $D(\mathbf{A})$: (a) $\phi_1(\lambda)$ and (b) $\phi_2(\lambda)$ for extended χ structure with dimensions $L_s = 20$ mm and $H_i = 22$ mm, and $\theta = 36°$. In the plot green dots indicate true roots and grey dots indicate possible spurious roots.

labeled AS^M for antisymmetric buckling modes. Figure 4.4 (a) and (b) are plots of $\phi_1(\lambda)$ and $\phi_2(\lambda)$, respectively. The roots of the functions are indicated by green dots.

Examining Fig. 4.4 (a) reveals a possible pitfall in determining the roots. The function $\phi_1(\lambda)$ has vertical asymptotes. This can cause two problems. First, if the plot of $\phi_1(\lambda)$ is too coarse, one may miss the true root in the zero-crossing portion of the algorithm. In addition, if the algorithm is used without first plotting the functions then it may find a root at the asymptote Possible spurious roots are denoted on Fig. 4.4 (a) by grey dots. In order to see if the root is spurious or not, the value of λ is plugged back into the matrix $\mathbf{A}$. If the value of the rank of matrix is full, then only the null solution exist for the eigenvalue problem and the root is spurious.

4.1.3 Finite Element Modeling

The analytical model was compared to two finite element models. The models were developed in ABAQUS and dubbed type 1, and type 2. The type 1 finite element model is the same model detailed in Chapter 3. In the type 1 model, the buckling is determined from the transition of a linear elastic response to a plateau response. For the sake of completeness the details of the model are repeated.

The type 1 model was created in ABAQUS using a Dynamic-Implicit analysis with a CPS4R element with hyperelastic material behavior that is described by the polynomial strain energy density function. The material properties are directly imported from experimental stress-strain results determined in Chapter 3. Using the imported data and hyperelastic model in Material module in ABAQUS, the coefficients are obtained automatically for a polynomial model of hyperelasticity. The extended χ structure was placed between two discrete rigid wire parts with surface contact. In addition, self contact properties are defined in the normal and tangential directions for the elements on the members' edges as hard contact and tangential contact with penalty coefficient of 1, respectively. The analysis is displacement controlled; the top surface is allowed to move until the χ structure has been compressed to 70% of its original height. A small perturbation force (0.01 to 0.05 N depending on the geometry) directed to right or left, is applied to the middle to initiate the asymmetric buckling instability in deformation. In this model buckling was judge to be the end of Region I on the effective stress-strain curve this occurred when the effective stress reached a plateau.

The type 2 model utilized a B21 wire beam element based on a linear Euler Bernoulli beam. Finally, the type 2 FEM model used a modulus of elasticity (E) of 432.2 MPa, and a poisson's ratio (ν) of 0.49. The structure is constrained from translating at the bottom and the top leg is subject to a points load f applied at both of its ends. The buckling eigenvalue from ABAQUS is given as $\lambda_p = \sqrt{2f/(EI)}$, where I is moment of inertia of the beam element. It should be noted that both FEM models do not prevent the swaying motion of the legs or neck of the extended χ structure.

4.2 Unit Cell Buckling

The following analysis considers an extended χ structure with $L_s = 20$ mm and $H_i = 22$ mm, and $\theta = 36°$. The first three AS^M buckling modes are shown in Fig. 4.5 (a)-(c), and the first three S^M buckling modes are shown in Fig. 4.5 (d)-(f). In addition each depiction of the mode is annotated to indicate the λ, the total applied load at the top of the structure F_{cr}, and a buckling eigenvalue λ_p. The first thing to note is that lowest buckling mode is antisymmetric, this makes sense intuitively. Each member is modeled as pinned-pinned beams and the first buckling mode of pinned beams are half sine waves and could be considered antisymmetric using the aforementioned definition. This mode also closely resembles the deformation observed by the structure at the onset of buckling, Fig. 3.1 (d). Observe that the pinned-pinned configuration of beam does not permit buckling deformations that are symmetric about it's axis. This is reflected in the current model by the member CD not experiencing any deformation for S^M modes.

Table 4.1 compares the buckling modes of the present analysis with the ABAQUS model. A detailed description of the model is provided in Appendix G. The results indicate that the analytic model and finite element analysis have less that 10% error for the first four modes. However, the fifth and sixth modes of the structure deviate significantly from the FEM analysis. Examining the FEM mode shapes, see Appendix G, one finds that the fourth mode has sway in the neck region. The present model does not allow for this type of motion. After the fourth mode the two models deviate in the deformation modes that they predict.

Table 4.1. Comparison of six analytical and finite element buckling eigenvalues, $\lambda_p = \sqrt{2f/(EI)}$.

Mode	λ_p Analytical	λ_p FEM	Percent Error
1(AS^M)	359.64	389.62	7.69%
2(AS^M)	416.77	459.46	9.29%
3(S^M)	476.03	470.51	1.17%
4(AS^M)	590.30	633.2	6.81%
5(S^M)	725.59	–	–
6(S^M)	1028.00	–	–

4.2.1 Effect of Angle on First Buckling Mode

The previous section focused on an analytical model that is capable of predicting multiple buckling modes. It should be noted that the loading and the material composition of the extended χ structure renders it difficult to experience the higher order buckling modes before the structure self contacts. Furthermore, the first buckling mode determines the length of Region I in the effective stress-strain relationship. Therefore, the focus of this section is on the accuracy of the first buckling mode to changes in characteristic angle of the unit cell.

The characteristic angle θ is varied from 26° to 46°. The limits are chosen to prevent the structure from buckling due to its own weight. As mentioned in section 3.4, the modulus of elasticity of 432.2 kPa is applied. Figure 4.6 compares the critical buckling loads from the present analytical approach with the FEM models. The results from the two solutions are in agreement for characteristic angles up to 42°.

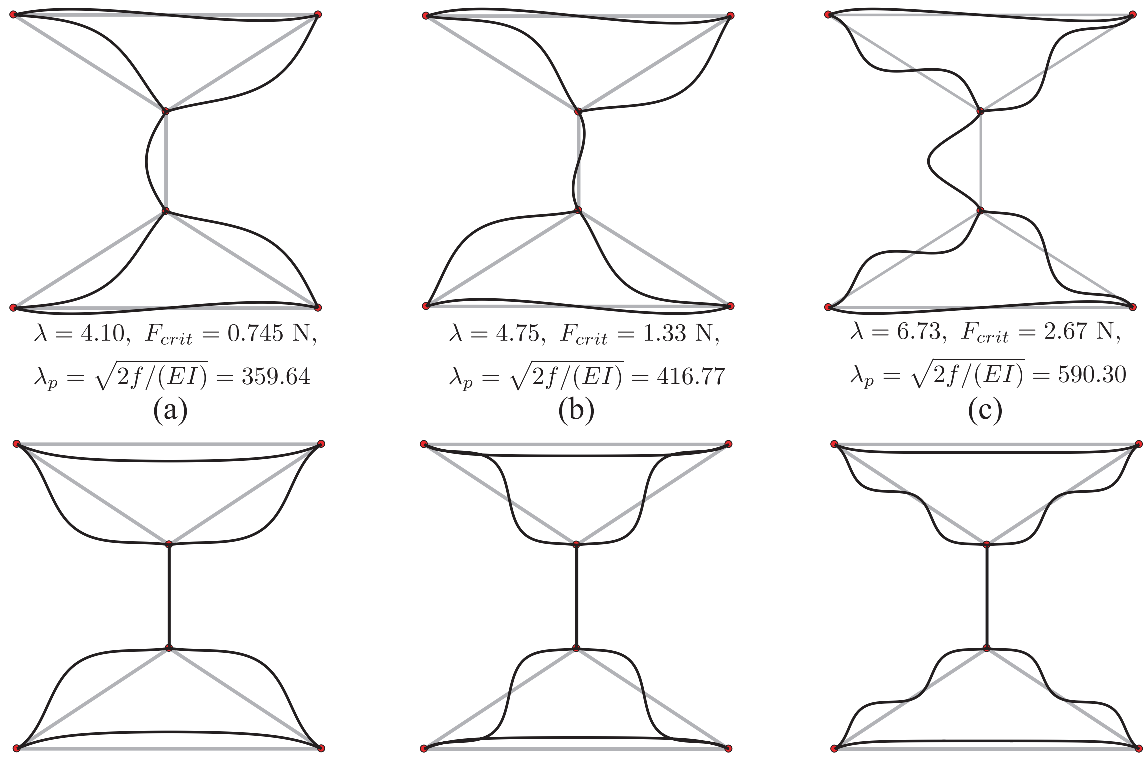

$\lambda = 4.10,\ F_{crit} = 0.745$ N, $\lambda_p = \sqrt{2f/(EI)} = 359.64$
(a)

$\lambda = 4.75,\ F_{crit} = 1.33$ N, $\lambda_p = \sqrt{2f/(EI)} = 416.77$
(b)

$\lambda = 6.73,\ F_{crit} = 2.67$ N, $\lambda_p = \sqrt{2f/(EI)} = 590.30$
(c)

$\lambda = 5.43,\ F_{crit} = 1.73$ N, $\lambda_p = \sqrt{2f/(EI)} = 476.03$
(d)

$\lambda = 8.27,\ F_{crit} = 4.04$ N, $\lambda_p = \sqrt{2f/(EI)} = 725.59$
(e)

$\lambda = 11.72,\ F_{crit} = 8.11$ N, $\lambda_p = \sqrt{2f/(EI)} = 1028.00$
(f)

Figure 4.5. First three symmetric and antisymmetric modeshapes of extended χ structure: (a), (b), (c) are antisymmetric modes and (d), (e), (f) are symmetric modes. The buckling shapes are plotted in black and the original configuration in gray. The critical dimensions of the structure are $L_s = 20$ mm and $H_i = 22$ mm, θ=36°.

However, for larger angles that the neck becomes shorter, the analytical results deviate from the FEM models. Again, the reason for the discrepancy is that the model is the no sway assumption, i.e., the model does not allow for a rigid body rotation of the neck. At smaller values of θ, the neck is sufficiently long enough to buckle as θ increases the neck shortens and experiences a rigid body rotation. This can be seen in the type 1 FEM shapes of the deformation of the structure near the end of Region I, Fig. 4.7 (b). When $\theta = 35°$ the deformation resembles the first AS^M , when $\theta = 45°$ the neck rotation is clear, and when $\theta = 40°$ the deformation is a between these

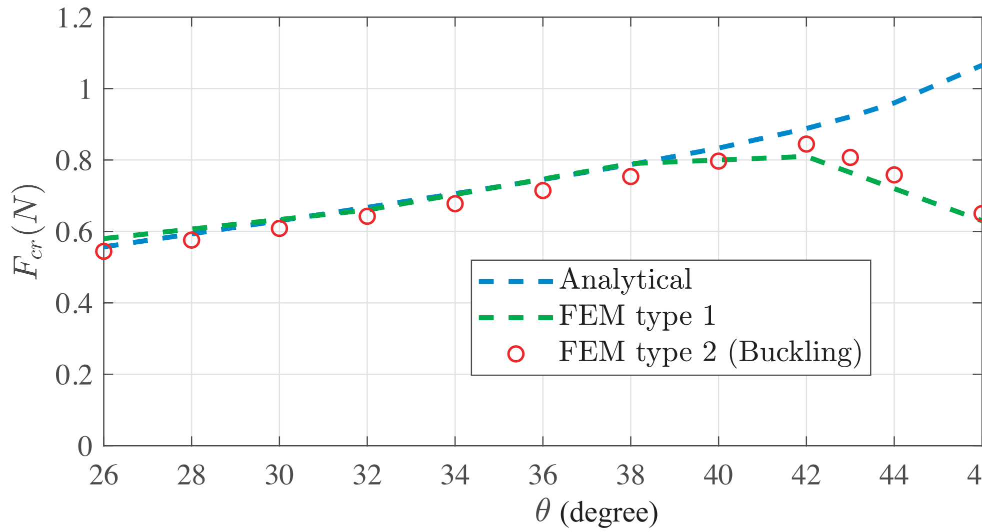

Figure 4.6. Critical buckling force F_{cr} versus characteristic angle θ for $L_s = 20$ mm and $H_i = 22$ mm from the analytical and FEM models.

two extremes, the neck both bends and rotates. This combination of motion causes uneven deformation of the diagonal legs at the top and bottom of the structure.

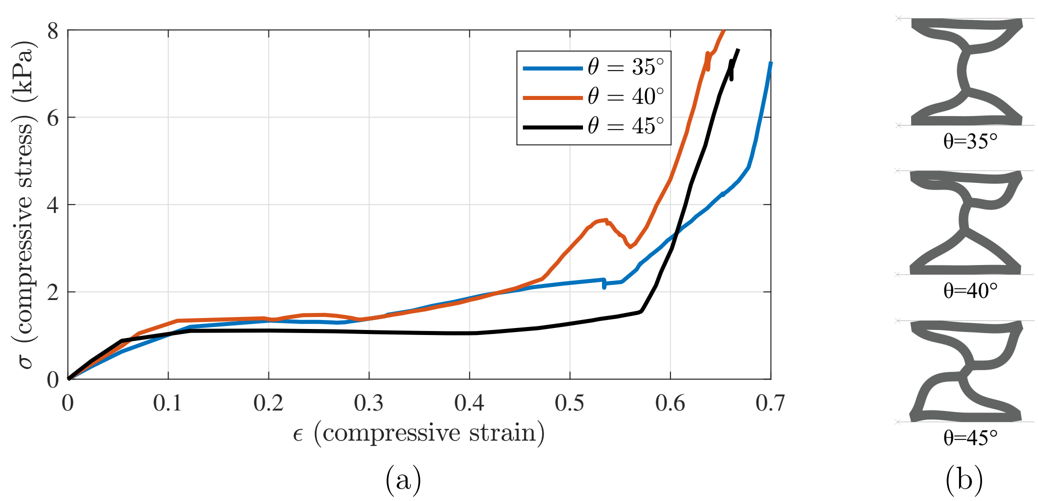

Figure 4.7. Neck dominated behavior, $\theta = 35°$ and $\theta = 40°$, where neck is long and buckled, versus $\theta = 45°$ where neck does not buckle but experiences a rigid body rotation.

4.3 Limitations to Extending Region I

The previous section examined how the characteristic angle can change the region of linear buckling. This section shows that manipulating the buckling behavior of the structure influences the entire effectives stress-strain curve. Figure .4.7 is a plot the effective stress-strain curve for χ structures with characteristic angles of $\theta = 35°$, $\theta = 40°$, and n $\theta = 45°$. A closer examination of the effective constitutive relationship in Fig. 4.7 when $\theta = 40°$ reveals that the effective stress-strain relationship does not show the typical three regions. The effective stress reaches a local maximum near an effective strain of 0.55 before declining and then increasing. Changing the length of neck causes the top legs and bottom legs to experience self contact at different points in time, hence the local maximum. Furthermore, when the neck is sufficiently long then Region II is no longer characterized by quasi-zero modulus as indicated by the stress-strain for a structure with an characteristic angle of 35°.

4.4 Chapter Summary

This chapter has provided a semi-analytical model of the buckling of the extended χ structure. At lower characteristic angle θ the model agrees with both finite element models: of buckling and effective stress strain characterization of the structure. However, the model is restricted to prevent rigid body rotations of its members causing it to be inaccurate in: 1) predicting higher order buckling modes, and 2) the buckling at larger values of the characteristic angle. The next chapter will utilize the FEM model of the unit cell to further explore the shock absorbing behavior of the structure.

5. SHOCK ABSORBING PERFORMANCE OF EXTENDED χ STRUCTURE

The shock absorption performance of the χ unit cell has been neglected up to this point. A unit cell's topology not only changes its quasi static stress-strain response; it also influences the energy that the structure can absorb. This chapter contains an exploration of this performance using a combination of analytical and finite element modeling. The analytical model mirrors the analysis of Chapter 2; however instead of examining the cushions curves of the polymer foams the theoretical cushion curve of a single extended χ unit cell is examined. Finite element models are used to examine the length of the the quasi-static region and the energy absorbed under the effective stress-strain curve.

5.1 Cushion Curve

In developing the cushion curve the analysis follows that of Chapter 2, the goal is to develop a dynamic model of ASTM D1596 [14] and examine the acceleration of an object when it is dropped on the extended χ unit cell. The process begins with a polynomial curve fit of the quasi-static stress-strain relationship this relationship is used to model the χ structure as a nonlinear spring. Using a simple lumped parameter model the transient response of the foam is treated as an initial value problem where the initial impact velocity of the mass is specified.

5.1.1 Curve Fit of Quasi-Steady State Stress-Strain

The quasi-static effective constitutive relationship of the extended χ structure can be modeled as a polynomial that can be written as

$$\bar{\sigma}(t) = \bar{E}_1 \left(\bar{\epsilon} + \sum_{k=2}^{K} \bar{E}_k \left(\bar{\epsilon}\right)^k \right), \text{ where } \bar{\sigma} = \frac{F}{A_{TS}} \quad \text{and} \quad \bar{\epsilon} = \frac{x}{H_i}, \tag{5.1}$$

where the constant $\bar{E}_1$ is the effective elastic modulus, and $\bar{E}_k$ are the effective relative elastic moduli, $\bar{\sigma}$ is the effective stress, $\bar{\epsilon}$ is the effective strain, F is the force on the top of the structure, A_{TS} is the area of the top surface of the structure, x is the displacement of the top of the structure, and H_i is the effective height of the extended χ structure. The effective elastic modulus and the effective relative elastic moduli, can be determined using a least squares fit. The number of terms in the approximation is equal to seven ($K = 7$); the coefficients for the fit are given in Table 5.1 for χ structure with characteristic angles of $\theta = 35°$, $\theta = 40°$, and $\theta = 45°$. In Fig. 5.1 (a), the experimental data is illustrated with red circular dots, and the curve fit with a blue line. The seventh order polynomial captures the stress in the three regions of deformation. Figure 2.1 (b) shows R^2 values for polynomial fits with orders ranging from four to nine. This plot clearly indicates that polynomial of orders greater than seven don't appreciably improve the curve fit.

Table 5.1. Modulus and relative moduli for uniaxial compression polynomial model of χ structure at $\theta = 35°$, $\theta = 40°$, and $\theta = 45°$.

Moduli and Relative Moduli	$\theta = 35°$	$\theta = 40°$	$\theta = 45°$
$\bar{E}_1$ (kPa)	2.65×10^{1}	2.21×10^{1}	2.40×10^{1}
$\bar{E}_2$ (kPa/kPa)	-1.34×10^{-2}	-8.38×10^{-3}	-9.70×10^{-3}
$\bar{E}_3$ (kPa/kPa)	9.64×10^{-2}	6.00×10^{-2}	6.29×10^{-2}
$\bar{E}_4$ (kPa/kPa)	-3.67×10^{-1}	-3.07×10^{-1}	-2.82×10^{-1}
$\bar{E}_5$ (kPa/kPa)	7.57×10^{-1}	8.88×10^{-1}	7.58×10^{-1}
$\bar{E}_6$ (kPa/kPa)	-7.98×10^{-1}	-1.26×10^{0}	-1.06×10^{0}
$\bar{E}_7$ (kPa/kPa)	3.39×10^{-1}	6.91×10^{-1}	5.89×10^{-1}

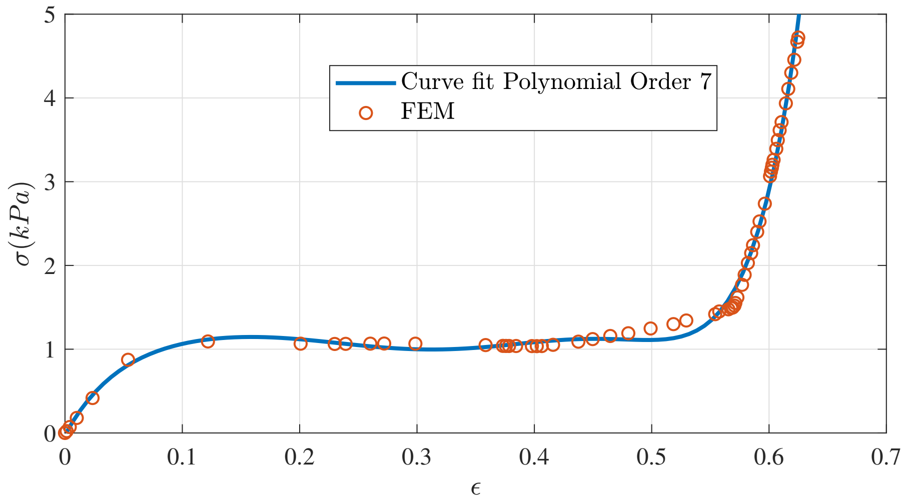

(a)

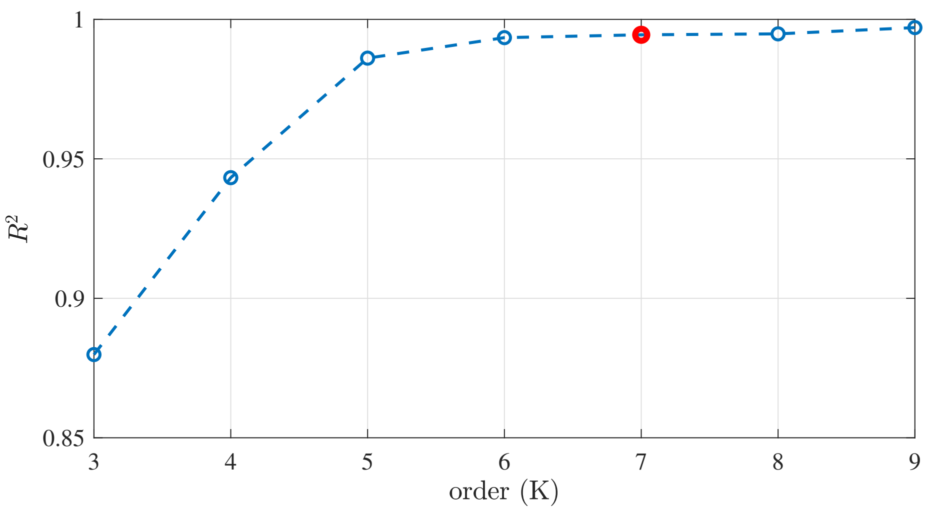

(b)

Figure 5.1. Quasi-static stress strain curve of extended χ structure at $\theta = 45°$ at 10 mm/s (a) and curve fit, (b) R^2 values for least square curve fits where polynomial order, K, ranges from four to nine.

5.2 Lumped Parameter Model

Now that the effective stress-strain response of the extended χ structure has been modeled, a dynamic model of the structure's response to an impact can be formulated. Figure 5.2 (a) shows an illustration of a drop test as applied to the extended

χ structure, while Fig. 5.2 (b) shows the proposed lumped parameter model used to simulate the test. The model incorporates several assumptions to simplify the

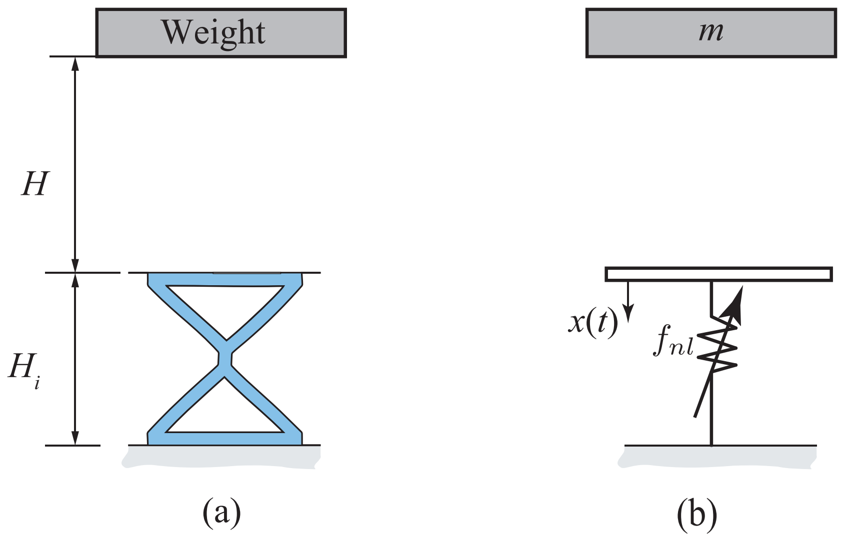

Figure 5.2. Drop test: (a) schematic, and (b) lumped parameter approximation.

analysis:

- The inertia of the structure is neglected and is modeled as a spring and damper.
- Frictional losses between the platten and the guide rails are neglected.
- The structure only deforms when it is in contact with the platten thus the viscoelastic effects are only present during deformation. Once the platten is removed, the material is assumed to recover instantly.
- The nonlinear restoring force is based on the constitutive relation in Eqn. (5.1) where the viscoelastic effects of the material are ignored.

The model consists of a mass m, representing the platten, a nonlinear spring representing the extended χ structure. The nonlinear spring's force f_{nl} equals $\bar{\sigma} A_{TS}$ and the model can be written as

$$m\ddot{x} + k_1 \left(x + \sum_{k=2}^{K} \hat{k}_k x^k \right) - mg = 0, \quad x(0) = 0, \ \dot{x}(0) = \sqrt{2gH}, \tag{5.2}$$

where k_1 is the linear stiffness equal to $\bar{E}_1 A_{TS}/H_i$, and k_k is the relative stiffness $\bar{E}_k A_{TS}/H_i$, g is the acceleration due to gravity, and H is the drop height. Equation 5.2 can be recast in terms of the static stress, σ_s, by using the relationship $m = \sigma_s A_{TS}/g$. The static stress is simply the stress caused by the platten if it rests on the cushion material. Equation (5.2) can be recast in terms of static stress as

$$\sigma_s \ddot{x} + \alpha_1 \left(x + \sum_{k=2}^{K} \hat{\alpha}_k x^i \right) - \sigma_s g = 0, \quad x(0) = 0,\ \dot{x}(0) = \sqrt{2gH}, \tag{5.3}$$

where the constants are defined as $\alpha_1 = \bar{E}_1 g/(H_i)$ and $\alpha_k = \bar{E}_k/(H_i^{k-1})$. The rewriting of the governing equations in terms of static stress is typical in the packaging research community [25] due to the weight of the platten being measured in terms of static stress instead of mass and facilitates sizing as will be shown the following paragraphs.

An energy based estimation of the cushion curve can be obtained by following the procedure outlined in Section 2.4. This method can be used to determine the peak acceleration (G) versus static stress for a range of drop heights. This results of this procedures are the cushion curves shown in Fig. 5.3. In this plot the cushion curves are determined for a range of drop heights (H/H_i of $2, 5, 10, 16$, and 24). Circles, dashes, and solid lines represent cushion curves for extended χ structures with angles of $\theta = 35°$, $\theta = 40°$, and $\theta = 45°$, respectively.

Now consider, the object that is to be protected has a 40 G acceleration limit during the impact before damage occurs when it is dropped from a height 10 times the height of the extended χ structure. On the cushion curve this limit is depicted as the horizontal red line on the plot of the $H/H_i = 10$ cushion curve , Fig. 5.4. In order to determine the range of static stresses that the χ structure meets this acceleration, one must determine the intersection points of the acceleration with the respective cushion curves. The corresponding static stresses at intersection points of these cushion curves with the acceleration limit are indicated by the dashed vertical lines. The plot indicates static stress limits of approximately 160-275 Pa, 140-222 Pa, and 140 - 210 Pa for structures with characteristic angles of 35° 40°, 45°, respectively.

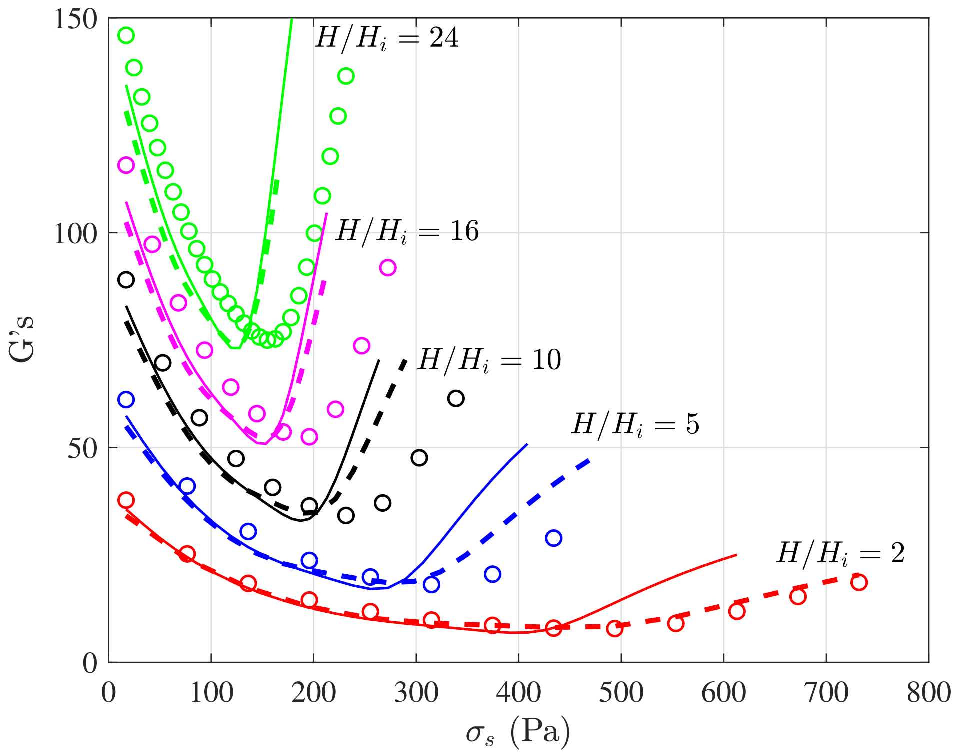

Figure 5.3. Estimates of cushion curves for extended χ unit cell with $H/H_i = 2, 5, 10, 16,$ and 24. The circles, dashes, and solid lines represent $\theta = 35°$, $\theta = 40°$, and $\theta = 45°$, respectively.

5.3 Effect of Topology

The previous model used a numerical curve fit of the stress-strain data to determine the cushion curves of three extended χ structures with different characteristic angles. In this sections the effect on the geometry will be studied on both the effective stress-strain relationship and two shock absorption metrics. The results in the section utilized the ABAQUS model developed in Section 3.2.1 to examine the length of Region II in terms of strain and the energy under the quasi-static stress-strain curve,

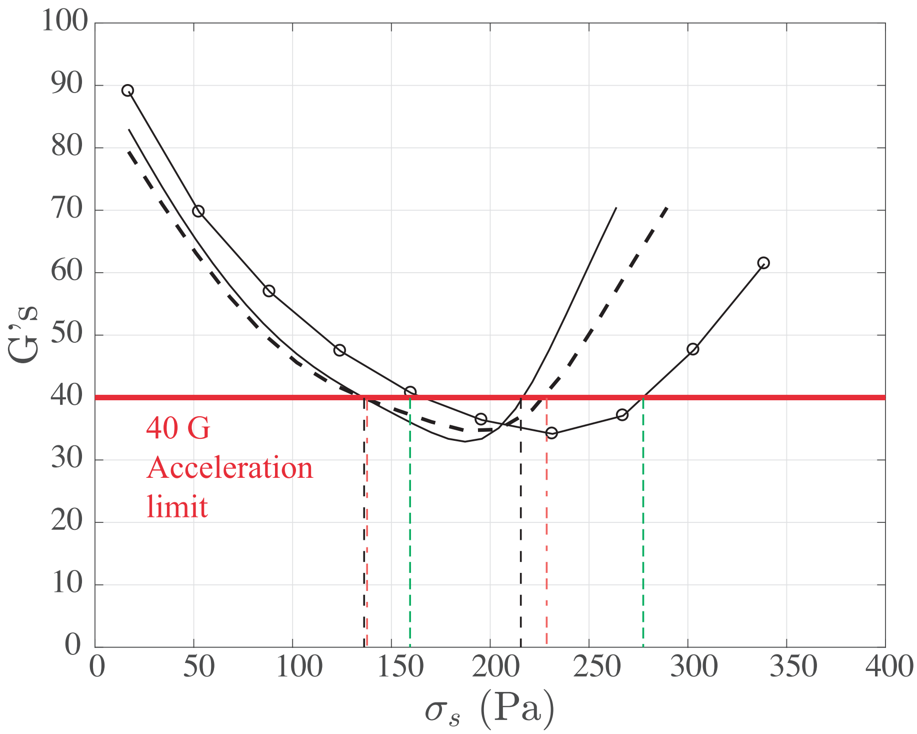

Figure 5.4. Estimates of cushion curves for extended χ unit cell with $H/H_i = 10$. The circles, dashes, and solid lines represent $\theta = 35°$, $\theta = 40°$, and $\theta = 45°$, respectively. The red line horizontal line indicates a 40 G acceleration limit. The regions of static stresses that can be withstood by the structure to maintain this limit are indicated by the dashed vertical lines.

i.e., toughness. In this analysis, the extended χ structure is modified for different characteristic angles θ an H_i/L_s to obtain stress-strain curve for each.

5.3.1 Plateau Analysis

The FEM results are processed to pick a point inside Region II. Two lines above and below the plateau with 10% value of the plateau stress are drawn to determine the beginning and end of Region II. The plateau stress is defined as the stress at which the effective strain curve is no longer linear. The start and end points are found as the x-coordinate of intersections of the lower and top lines with the curve respectively. The length of a plateau is obtained by subtracting end from start point x-coordinate

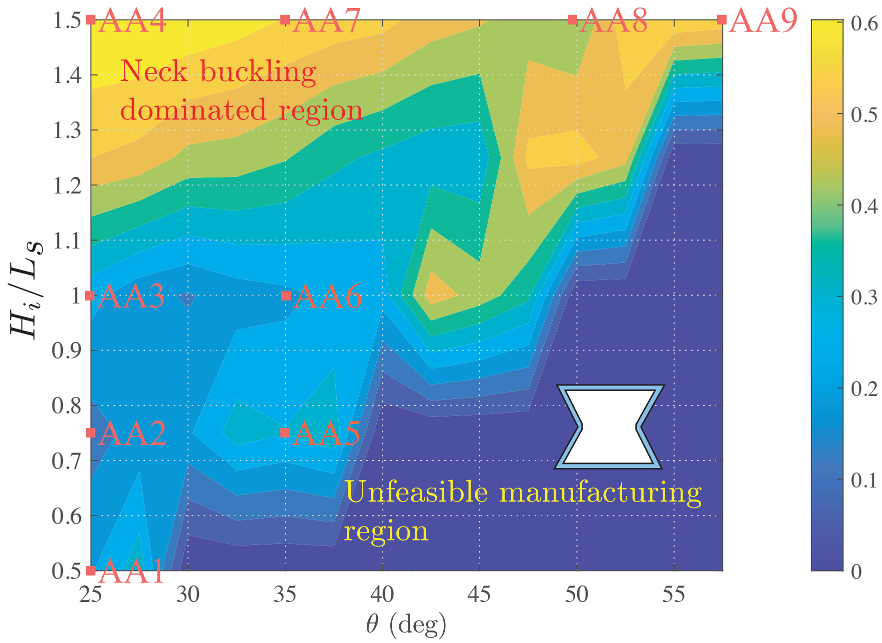

(a)

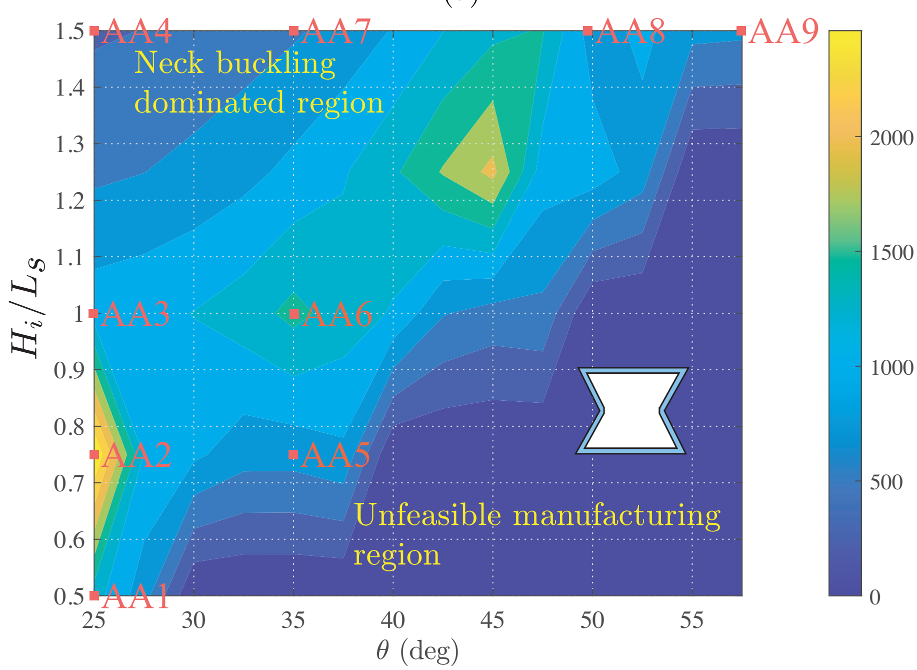

(b)

Figure 5.5. Geometric examination: (a) the effect of angle and H_i/L_s variations on non-dimensionalized plateau length, (b) the effect of angle and H_i/L_s variations on absorbed energy before densification.

values. Then the length of the plateau is divided by the corresponding inner cell height, H_i, to non-dimensionalize the results. Figure 5.5 (a) shows the plateau length for H_i/L_s ratios and characteristic angles (θ) ranging from 0.5 to 1.5 and 25° to 55°, respectively. The left top corner of Fig. 5.5 (a) is related to high H_i/L_s ratios and low angles that produce long necks and is called "neck buckling dominated region". If the H_i/L_s is low, it is no longer possible to manufacturing the extended χ structure for large characteristic angles. The bottom right corner represents high angles with low H_i/L_s ratios that is called "unfeasible manufacturing region". In this region the angles yield geometries that are trapezoidal and no longer have a neck, see the inset in Figs. 5.7 (a) and (b). The unfeasible manufacturing regions are not considered.

The plots of plateau length in Fig. 5.5 (a) reveal several noteworthy trends. In general, the plateau length is larger for high aspect ratio structures, and are in the neck dominated buckling region. In these cases, the neck initially buckles and deforms before self contact occurs. The annotations AA1-AA9 indicate selected points in Fig. 5.5 (a), the corresponding stress-strain curves for these points are shown in Fig. 5.6 (a) to (c). AA4, AA7, AA8, and AA9 indicate structures whose aspect ratio (H_i/L_s) is equal to 1.5, the corresponding structures have long plateau lengths. In general, as the aspect ratio is lowered the plateau length shrinks regardless of a change in characteristic angle. Examples of stress-strain curves in the region that have reduced or negligible plateau length correspond to points AA1, AA2, AA3, AA5, and AA6. Note in particular structures with a characteristic angle of 25° (AA1 - AA4) that the stress-strain curve has no clear delineation between Region I and Region II (QZM region).

5.3.2 Absorbed Energy Analysis

Absorbed energy or toughness before densification is obtained by integrating the stress-strain curve from beginning to the obtained end point of the plateau region. Figure 5.5 shows the contour plot of absorbed energy for different characteristic angle and H_i/L_s ratios. The point AA2 lies in the maximum energy absorption region. This structure's effective stress-strain curve has several interesting traits: 1) it does not posses a clear Region I and Region II, 2) densification occurs at a high strain, and 3) the magnitude of the stress-strain curve is large. Point AA6 also has the next largest toughness and the stress-strain curve has similar traits, i.e., large magnitude and no clear distinction between Region I and Region II. In this case, the transition to the densification region is less distinct.

5.3.3 Effect of Leg Thickness on Plateau Length and

In addition to the characteristic angle the thickness of the legs effect on Region II and absorbed energy was investigated. Consider that extended χ structures with thicker legs shows higher resistance to buckling. Figures 5.7 (a) and (b) shows contour plots for plateau length and absorbed energy, respectively, for legs thicknesses from 1 mm to 3 mm and characteristic angles from 40° to 45°. Thinner legs provide longer plateau while absorb lower energy. Samples with lower leg thickness and characteristic angles shows higher energy absorption and reduced plateau lengths. The reason for this behavior can be seen plotting points the stress-strain curves at points labeled A1-A9 on the contours in Fig. 5.7 (a) and (b). Points A1-A3 are for 1 mm thick legs and characteristic angles of 40°, 42°, and 45°, respectively. Points A4-A6 are for 2 mm thick legs and characteristic angles of 40°, 42°, and 45°, respectively. Points A7-A8 are for 3 mm thick legs and characteristic angles of 40°, 42°, and 45°, respectively. Regardless of characteristic angle, the curves are clustered by magnitudes based on thickness of legs. In this clustering several noteworthy trends are present. First, the curves corresponding to 1 mm legs have the lowest plateau stresses but the longest quasi-zero modulus (QZM) regions. As the leg thickness increases to 2 mm the linear (Region I) and densification (Region III) regions grow and the QZM regions (Region II) shrinks. In addition, the overall magnitude of stress-strain curve increases for 2 mm thick legs compared to extended χ structures with 1mm thick legs. This trend continues as the legs are increased to 3 mm; however, here the characteristic angle plays a more prominent role. In this case, extended χ structures at 42° and 45° have a Region II that is of lower modulus than Region I and II at these angles but is no longer quasi-zero. The transition from the linear region to the QZM region is less delineated. The increase in magnitude as leg thickness increases allows the structure to absorb more energy, i.e., an increase in area under the stress-strain curve as seen in Fig. 5.7 (b).

5.4 Chapter Summary

This chapter explored the performance of extended χ using a combination of analytical and finite element modeling. The analytical model mirrors the analysis of Chapter 2, here we examine the theoretical cushion curve of a single extended χ unit cell. In the cushion curve analysis, the extended χ structure mirrored the cushion curve of a typical packaging foam.

Finite element models are used to examine the length of the the quasi-static region and the energy absorbed under the effective stress-strain curve. FEM analysis indicates that unit cells with larger characteristic angles and aspect ratios yield longer plateau regions.

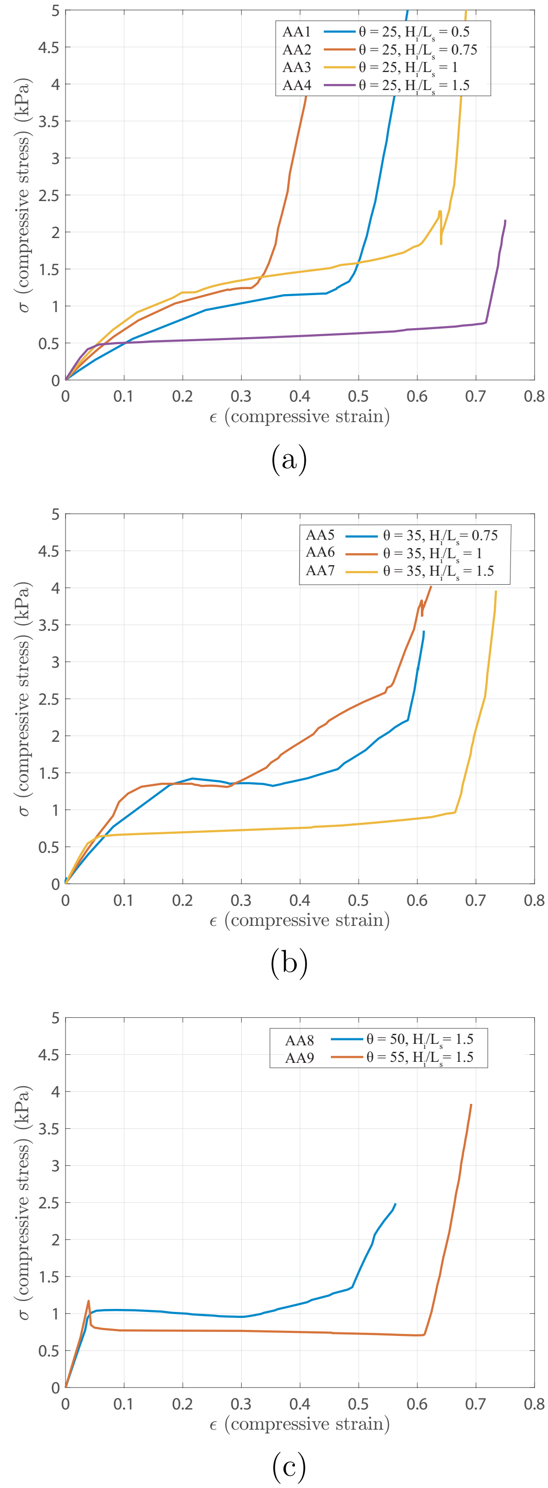

Figure 5.6. Selected stress-strain curves for points AA1 through AA9 on non-dimensionalized plateau length and absorbed energy contours.

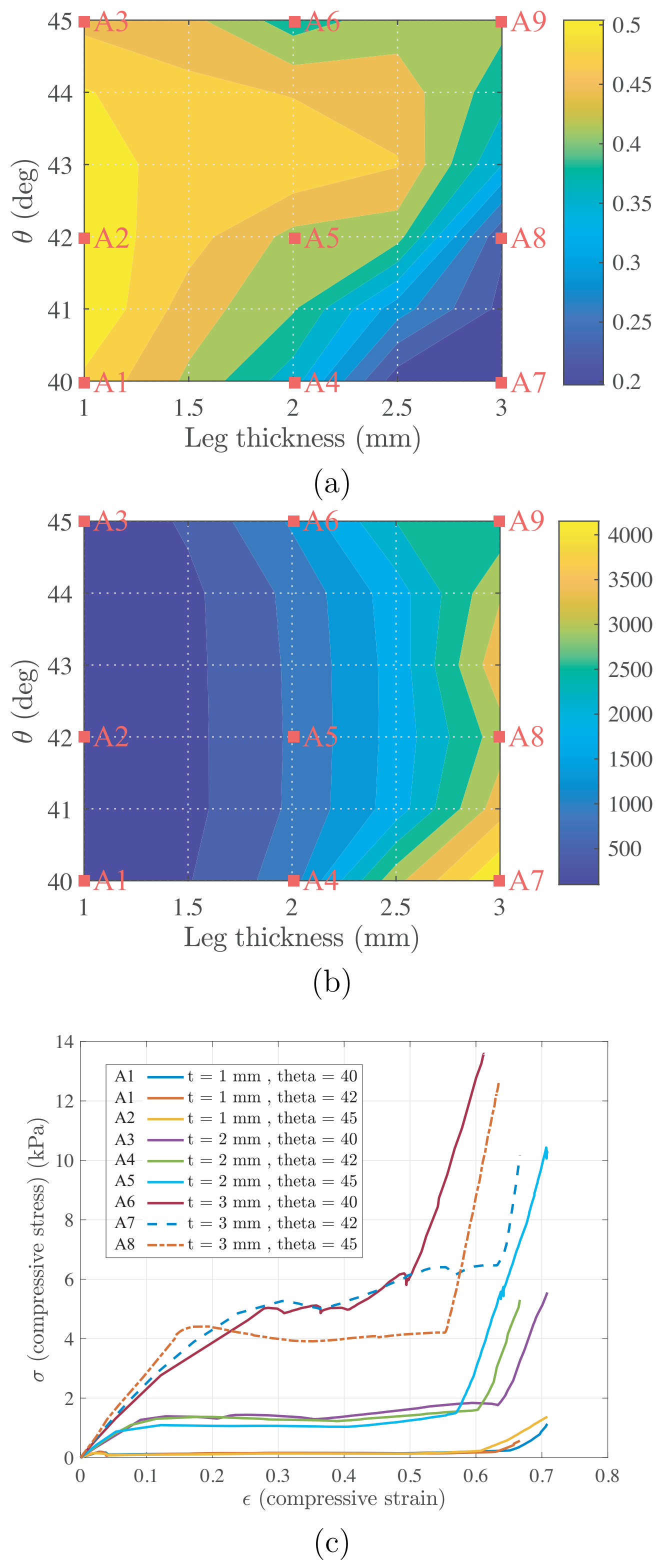

Figure 5.7. Contour plots of (a) plateau length and (b) absorbed energy, (c) selected stress-strain curves, for different characteristic angles and leg thicknesses.

6. 2-D EXTENDED χ STRUCTURE

The previous chapters explored the behavior of the extended χ unit cell. The unit cell is designed to be loaded in one direction that is normal to the top and bottom legs of the structure. This restriction on loading limits its shock absorbing capabilities in a real world environment where the structure may experience loading in multiple directions. This chapter briefly explores using the basic extended χ unit cell to provide an equal force displacement response in two directions. In terms of shock absorbing applications a material that posses these characteristics will not have a preferred loading direction and thus emulate a polymer foam in providing multi-directional protection. The chapter details the initial concept, fabrication, finite element modeling and force displacement characterization of the 2-D χ structure.

6.1 2D Extended χ Structure

The extended χ shaped architecture can be arranged to provide quasi-zero stiffness not only in 1-D but also in 2-D. A 2-D unit cell can be obtained by arranging the extended χ structure along the perimeter of a square, Fig 6.1 (a). In this version, the square is hollow, however; it may be filled or have an inset to increase its stiffness and stability. Figure 6.1 (b) shows a tessellation of the unit cell. Observe that the tessellated unit cell results in a diamond shaped cavity in the structure. Without the stiffeners in this cavity the deformation of the structure will not be isolated to the underlying leg and neck 1-D unit cell instead all members of the cell will deform. In the tessellated version, stiffened regions are indicated by dark black lines. Finally, note in both Fig 6.1 (a), (b), contain a 1-2-3 material coordinate system. The 3 axis points out of the page. The addition of the coordinate system was included to discuss the symmetry of the force-displacement relationship of the structure.

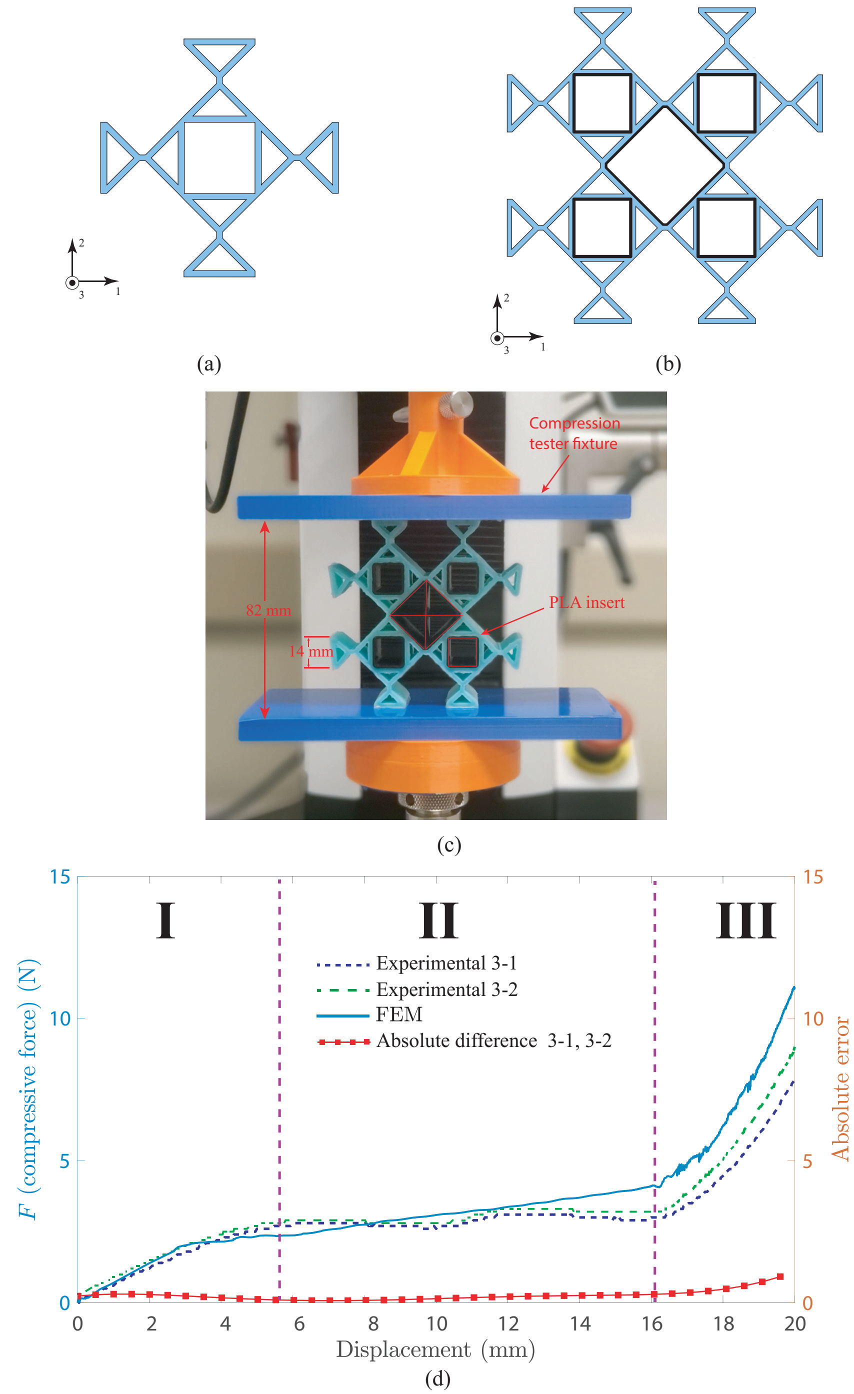

Figure 6.1. Two dimensional extended χ structure: (a) 2-D unit cell, (b) tessellated 2-D unit cell with inserts, (c) experimental material characterization, and (d) force-displacement curve for FEA analysis, and experimental compression along two faces.

6.1.1 Manufacturing

The manufacturing of the 2-D extended χ structure follows the same procedure as the 1-D unit cells. They are made by casting a platinum cure two part silicone rubber (Smooth-On Mold Star 15S) in polylactic acid (PLA) thermoplastic negative molds. The molds are in turn produced on a fused deposition 3D printer (Ultimaker S5). The rubber is allowed to cure in the molds for two hours at 50 °C in a Print Dry filament dryer and then allowed to aerate for 24 hours. In addition, the Ultimaker S5 is used to print the inner stiffeners. The total unit cell is contained in a square with sides of 82 mm length. The underlying 1-D extended χ unit cell has dimensions of $L_s = H_i = 14$ mm, $t = t_n = L_n = 2$ mm, and $\theta = 45°$.

Figure 6.1 (c) shows the finalized prototype before testing. We observed that due to manufacturing limits; it was not possible to produce a perfectly stable single unit cell shown in Fig 6.1 (a), hence the analysis will utilize the tessellated cell shown in Figure 6.1 (b).

6.1.2 Finite Element Model

The finite element model is an extension of the 1-D unit cell model found in section 3.2.1 using a Dynamic-Implicit analysis with a CPS4R element with hyperelastic material behavior that is described by the polynomial strain energy functional in ABAQUS. The material properties are directly imported from experimental stress-strain results. Similar to the extended χ structure, the 2-D extended χ structure was placed between two discrete rigid wire parts with surface contact. Self contact is defined in the normal and tangential directions for the elements on the members' edges as hard contact and tangential contact with penalty coefficient of 1, respectively. The analysis is displacement controlled; the top surface is allowed to move until the χ structure has been compressed to 30% of its original height. A small perturbation force (0.01 to 0.05 N depending on the geometry) directed to right or left, is applied to the middle to initiate the asymmetric buckling instability in deformation.

6.1.3 Characterizing the Nonlinear Force Displacement Relationship

In the analysis of the 1-D structures, an effective strain and stress was introduced in the discussing the unit cell's behavior. In discussing the 2-D extended χ structure, these quantities are replaced by the compressive force on the platten and the compressive distance between the platten due to the geometry of the unit cell, i.e., it does not have a continuous surface that may be compressed. Similar to the characterization of the 1-D extended χ structure the 2-D structure is tested on Mark 10 ESM 1500 electromechanical load frame with a load capacity of 6700 N (1500 lbF). In the tests, the frame is equipped with a Mark 10 MR01-50 load cell that has a 250 N (50 lbf) capacity and a 0.1 N (0.02 lbf) resolution. The sample is first tested along the 3 face in the 1 direction. Then it is rotated for 90° and tested again and tested along the 3-face in the 2 direction. Figure 6.1 (d) compares the recorded two force-displacement curves with the results from FEM analysis in ABAQUS. The first thing to note is that forced displacement curve retains the desired three regions in both material directions. The results of the two faces are in agreement and compared to ABAQUS model and they both agree with the model. However, they deviate gradually from each other as displacement increases. The maximum deviation occurs during densification in Region III with a maximum of 12.8% difference in force. This deviation may originate from manufacturing imperfections, e.g. pockets of air in the material after solidification, geometric imperfections that occur when removing the sample from the mold, and inconsistency in the manufacturing of the PLA supports. The presence of air bubbles may be eliminated by placing the rubber in a vacuum chamber before casting.

6.1.4 Limitations

Extending the extended χ structure to act in multiple dimensions is not without its limitations. Here, we have considered a version of the basic unit cell with a cavity. This was done to reduce weight. Figure 6.2 (a) shows the finite element analysis of this structure with the cavity that has not been stiffened. The analysis indicates that buckling is no longer confined to the diagonal legs and neck as in the original extended χ structure this is due to the cavity being more compliant than the 1-D unit cells. In this case, the legs of the basic 1-D unit cell deform in compression. This is not possible in the original arrangement of the 1-D unit cell in compression since the top and bottom legs are always in tension. In order to counteract this behavior the stiffeners were added to the cavities, Fig. 6.2 (b). In this case there is some separation of the elastomer from the PLA stiffeners. Nonetheless, the most prominent drawback is that the deformation only engages the four 1-D unit cells; two on the bottom and two on the top of the structure.

This structure like the 1-D unit cell is limited in the types of loading that it can resist. The current topology restricts its uses to applications where the loading is in the 1 and 2 material directions, no support is offered in the 3-direction. Furthermore, the analysis has not considered the application of a load that is applied at angle. In order to accommodate this type of loading the structure would need to be encapsulated in a square domain with side walls.

6.2 Chapter Summary

This chapter contains an analysis of 2-D tessellated extended χ unit cell. The cells are fabricated using a combination of 3D printing of negative PLA molds, and PLA stiffeners. The material for the tessellated unit cell is a two part silicone rubber. Compression test in two different material directions indicate that the force displacement relationship has a maximum deviation of 12%. This deviation is attributed to air pockets present in the material and imperfections that occurred during the removal of the structure from the mold. Despite the limitations, compression test indicate that force-displacement relationship retains the characteristic three regions of the original extended χ unit cell.

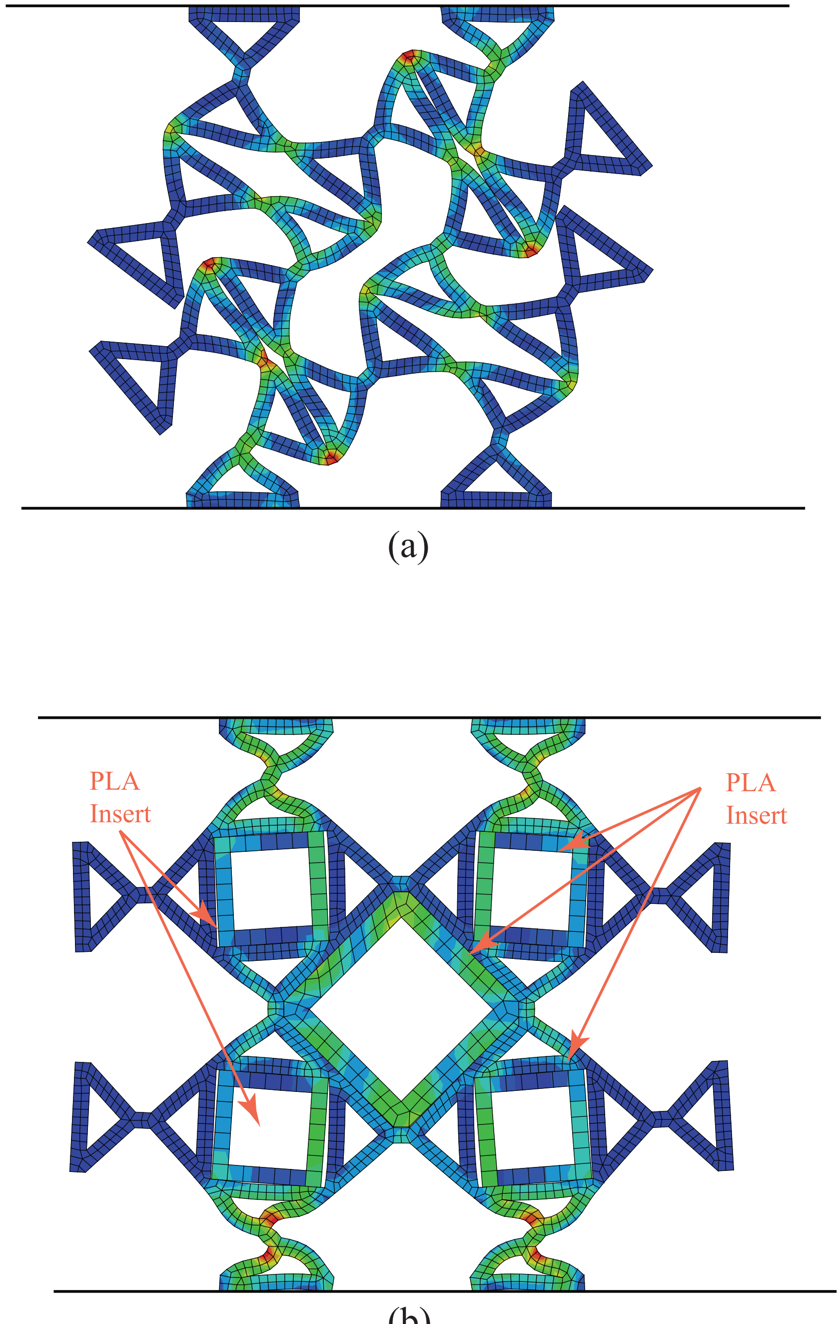

(a)

(b)

Figure 6.2. Deformation of two dimensional extended χ structure in compression: (a) without PLA inserts, and (b) with PLA inserts.

7. CONCLUSIONS AND FUTURE WORK

This chapter reviews the research question discussed in Chapter 1. In addition, it provides insights about this study and suggestions about possible future work.

7.1 Concluding Remarks

The research questions in Chapter 1 were divided into two categories, the first group of questions were focused on the multimodal response of polymer foams subject to an impact and are as follows:

1. *What are the effects of higher order modes of vibration on the rebound acceleration of an object impacting a cushion?*
2. *What are the effects of damping on the rebound acceleration?*
3. *Using this multimodal analysis, what are the dominant constitutive properties of foam for shock response?*
4. *Using this multimodal analysis, can a quasi-static compressive test be used to determine the acceleration pulse?*

The second set of research questions are focused on the shock absorption characteristics on an architected material. These research questions are as follows::

5. *What geometry effectively mimics the quasi-static compression and shock absorption of an elastic closed cell foam?*
6. *Can the quasi-static compressive behavior of the architected material be modeled using FEA?*
7. *Can the elastic buckling of the structure be modeled analytically?*

8. *Can the geometry be tessellated to provide bi-directional tunable quasi-static compressive behavior?*

All of these items are addressed and summarized here.

Question 1

The study in Chapter 2 models the dynamics of a falling platten impacting a foam cushion as a nonlinear rod with an end mass subject to an initial velocity. It departs from the lumped parameter paradigm that is typically used to determine cushion response. The nonlinearities are a result of the hyperelastic material describing the foam's stress-strain behavior. Both the nonlinearity and the viscoelasticity are modeled with a polynomial constitutive relationship combined with a Kelvin-Voight model of damping. It is evident that in a linear response the first mode dominates the response with its amplitude being an order of magnitude higher than the higher orders modes of vibration. The amplification factor for each mode initially decreases as the static stress increases until each it reaches an asymptote. When the nonlinearities are included the effects of the number of modes on the response becomes less clear and depend on the static stress the foam is subjected to during impact. However, the multimodal response appears as a dominant single mode waveform with higher oscillations superimposed on the response. The inclusion of modes has a minimal effect on the prediction of a cushion curve.

Question 2

Chapter 2 shows that damping improves the prediction of the peak rebound acceleration but its effect is secondary to the nonlinear quasi-static behavior for the polystyrene foam considered in this study. This is evident when damping is ignored and a single mode approximation is used. In this case, analytical estimates of the cushion curve can be determined using an energy balance approach. The energy balance estimation, while predicting the overall shock characteristics of the foam, under predicts the peak acceleration at lower drop heights and static stresses and over predicts higher drop heights and static stresses. Furthermore, the energy based estimation is limited to materials for which the dynamic stress and quasi-static stress versus strain responses are similar in shape and magnitude. Including damping in the model and solving the governing equations of motion numerically improves cushion curve prediction. It is worth noting that for the both undamped and damped cases the predicted impact shock responses are in agreement with experimental results, and the latter closely matches. This approach works well, since the dynamic stress-strain relationship is not significantly greater than the quasi-static stress-strain relationship in the polystyrene foam.

Question 3

In both a single mode and multiple mode approximation the acceleration waveform is determined by nonlinear material behavior. As mentioned in Item 1, the multimodal response appears as perturbations superimposed on the single mode response. In both cases the overall shape of the waveform is determined by the static stress and material behavior. Similar to the single mode response, the shape of the waveform and the cushion depends on both material behavior and static stress. The characteristic “trough” like shape of the cushion curve is directly due to the nonlinear quasi-static stress-strain relationship in a multi mode analysis. This relationship has three distinct regions of stress and strain: 1) Region I is a linear elastic zone, 2) Region II is a zone of stress and strain where the modulus in small of near zero, and 3) Region III is a densification zone of high modulus due to the internal walls of the foam contacting. Each region influences the shape of the cushion curve of a foam regardless of the number of modes included in the model.

Question 4

The model is used to generate acceleration waveforms during impact, and by varying static stresses, one can generate a set of cushion curves. In addition, the results in Chapter 2 show that the model can predict the peak rebound acceleration and yield accurate predictions of the time waveform. Again, this is due to the effect of damping being secondary in the response, and that a simple damping model can represent the polystyrene foam in this study.

Question 5

Chapter 3 introduces a unique structure made of silicon rubber that yields an effective stress strain relationship that resembles the stress-strain behavior of polymer foams. The chapter has provided an overview of both the material and unit cell response. The unit cell is dubbed the extended χ structure due to it “X” shaped topology. The topology of the unit cell can be described by a characteristic angle between the diagonal and the horizontal legs of the structure.

Chapter 5 explored the performance of extended χ using a combination of analytical and finite element modeling. The analytical model mirrors the analysis of Chapter 2 of polymer foams, here we examine the theoretical cushion curve of a single extended χ unit cell. In the cushion curve analysis, the extended χ structure mirrored the cushion curve of a typical packaging foam. Finite element models are used to examine the length of the quasi-static region and the energy absorbed under the effective stress-strain curve. FEM analysis indicates that unit cells with larger characteristic angles and aspect ratios yield longer plateau regions. However, this does not translate into energy absorption where there is a near linear relationship between aspect ratio and characteristic angle on maximum energy absorbed.

Question 6

Chapter 5 demonstrated that an FEM model is able to reproduce the effective stress-strain behavior of the extended χ unit cell for experimental geometry considered in this study. The model predicts the onset of the three distinct regions of deformation; however, there is roughly a 20% maximum relative difference in compressive strain between the model and the experimental results. It is theorized that these deviations in the model and prototype response are due to: (1) the imperfections in the sample such as raised small air bubbles during solidification and tiny damages during demolding, (2) approximate contact parameters in FEM, between the legs in the extended χ structure and between the legs and the rigid compressors, and (3) approximate hyperelastic material model in FEM.

Question 7

Chapter 4 has provided a semi-analytical model of the buckling of the extended χ structure. At lower characteristic angle θ the model agrees with both finite element models: of buckling and effective stress strain characterization of the structure. However, the model is restricted to prevent rigid body rotations of its members causing it to be inaccurate in: 1) predicting higher order buckling modes, and 2) the buckling at larger values of the characteristic angle.

Question 8

Chapter 6 contains an analysis of 2-D tessellated extended χ unit cell that exhibits similar response in two material directions. The cells are fabricated using a combination of 3D printing of negative PLA molds, and PLA stiffeners. The material for the tessellated unit cell is a two part silicone rubber. Compression test in two different material directions indicate that the force displacement relationship has a maximum deviation of 12%. This deviation is attributed to air pockets present in the material and imperfections that occurred during the removal of the structure from the mold. Despite the limitations, compression tests indicated that the force-displacement relationship retains the characteristic three regions of the original extended χ unit cell.

7.2 Future Directions

In the analysis of cushion curve prediction discussed in Chapter 2, the damping coefficient is determined by matching the analytical acceleration peak (of an arbitrary static stress and drop height ratio) with its corresponding experimental data. The obtained damping coefficient is then applied to all other cases. While this approach saves cost, simplifies the solution procedures, and provides acceptable results within $\pm 18\%$ of experimental results; it neglects that the material response may be strain rate dependent. This effect can be captured by higher order viscoelastic models of the stress-strain relationship. Furthermore it may extend this modeling approach to materials where the dynamic stress-strain relationship differs from greatly from the quasi-static stress-strain relationship.

In a recent study, Rice et al. [72] studied viscoelastic material application in designing protective cushion for packaging and helmets. They highlighted the importance of impact duration that is either long duration where acceleration is mitigated to avoid damage, or short duration where the velocity changes before and after of impact is the reason of damage. For implementing both criteria into the cushion design, an optimum viscoelastic property is selected. This analysis can be implemented into the nonlinear model discussed in Chapter 2 to better study the viscoelasticity part of our model and to analyze the effect of impact duration on cushion curves.

Numerous variations other than the proposed extended χ meta-material structures in Chapter 3 can be designed for the purpose of shock absorption enhancement. The main idea is to build a structure with a set of connected legs that resists compression pressures to a desired level then buckles quickly and proceeds to a large strain without noticeable change in stress until self-contact occurs. In the present analysis in Chapter

3, the χ geometry is symmetric, e.g. all legs have same length and thickness. This study can be expanded by investigating the result of asymmetric geometry change on compression and cushion diagrams.

Structures with self-sensing properties are able to sense their own condition such as temperature, strains, etc. [73]. Attaching sensors to legs converts the extended χ to a self-sensing structure in determining its effective strain. One means of accomplishing this to utilize triboelectric generators attached to the legs of the χ structure. Triboelectics are flexible polymer based sensors that utilize electrostatic induction and contact electrification in their operation. Previous work by Tao and Gibert [74] have shown the efficacy of these devices when they are embedded in polymer based metamaterials. In this application, the devices could be surface mounted to two opposing legs.

REFERENCES

REFERENCES

[1] JE Alexander. Shock response spectrum-a primer. *Sound & Vibration*, 43(6):6–15, 2009.

[2] R Sabelli. *Research on improving the design and analysis of earthquake resistant steel braced frames*. EERI Oakland, 2001.

[3] FA Noghondar and E Bressel. Effect of shoe insole density on impact characteristics and performance during a jump-landing task. *Footwear Science*, 9(2):95–101, 2017.

[4] T Fadiji, C Coetzee, P Pathare, and UL Opara. Susceptibility to impact damage of apples inside ventilated corrugated paperboard packages: Effects of package design. *Postharvest Biology and Technology*, 111:286–296, 2016.

[5] LJ Gibson and MF Ashby. *Cellular Solids: Structure and Properties*. Cambridge University Press, 2nd edition, 1997.

[6] J Miltz and O Ramon. Energy absorption characteristics of polymeric foams used as cushioning materials. *Polymer Engineering & Science*, 30(2):129–133, 1990.

[7] FM Casati, PR Berthevas, RM Herrington, and Y Miyazaki. The contribution of molded polyurethane foam characteristics to comfort and durability of car seats. Technical report, SAE Technical Paper, 1999.

[8] FM Shuaeib, AMS Hamouda, SV Wong, RS Radin Umar, and MMH Megat Ahmed. A new motorcycle helmet liner material: The finite element simulation and design of experiment optimization. *Materials & Design*, 28(1):182–195, 2007.

[9] TJ Cui, DR Smith, and R Liu. *Metamaterials*. Springer, 2010.

[10] M Wegener. Metamaterials beyond optics. *Science*, 342(6161):939–940, 2013.

[11] J Bunyan and S Tawfick. Exploiting structural instability to design architected materials having essentially nonlinear stiffness. *Advanced Engineering Materials*, 21(2):1800791, 2019.

[12] WT Thomson. Shock spectra of a nonlinear system. *Journal of Applied Mechanics*, 27(3):528–534, 1960.

[13] MA Biot. *Transient Oscillations in Elastic Systems*. PhD thesis, California Institute of Technology, 1932.

[14] ASTM. D1596: Dynamic shock cushioning characteristics of packaging material. In *Annual Book of ASTM Standards*. ASTM International, West Conshohocken, Pa., 2014.

[15] M Daum. A simplified process for determining cushion curves: The stress energy method. In *Proceeding from Dimensions 2006*, San Antonio, TX, 1997.

[16] ASTM. D3332-9: Standard test methods for mechanical-shock fragility of products, using shock machines. In *Annual Book of ASTM Standards*. ASTM International, West Conshohocken, Pa., 2010.

[17] J Miltz and G Gruenbaum. Evaluation of cushioning properties of plastic foams from compressive measurements. *Polymer Engineering & Science*, 21(15):1010–1014, 1981.

[18] E Suhir. Dynamic response of a one-degree-of-freedom linear system to a shock load during drop tests: effect of viscous damping. *IEEE Transactions on Components, Packaging, and Manufacturing Technology: Part A*, 19(3):435–440, 1996.

[19] O Ramon and J Miltz. Prediction of dynamic properties of plastic foams from constant–strain rate measurements. *Journal of Applied Polymer Science*, 40(9-10):1683–1692, 1990.

[20] O Ramon, S Mizrahi, and J Miltz. Mechanical properties and behavior of open cell foams used as cushioning materials. *Polymer Engineering & Science*, 30(4):197–201, 1990.

[21] G Burgess. Consolidation of cushion curves. *Packaging Technology and Science*, 3(4):189–194, 1990.

[22] G Burgess. Generation of cushion curves from one shock pulse. *Packaging Technology and Science*, 7(4):169–173, 1994.

[23] TL Totten, G Burgess, and SP Singh. The effects of multiple impacts on the cushioning properties of closed-cell foams. *Packaging Technology and Science*, 3(2):117–122, 1990.

[24] G Li, V Rouillard, and MA Sek. Evaluation of static and dynamic cushioning properties of polyethylene foam for determining its cushion curves. *Packaging Technology and Science*, 28(1):47–57, 2015.

[25] MA Sek, M Minett, V Rouillard, and B Bruscella. A new method for the determination of cushion curves. *Packaging Technology and Science: An International Journal*, 13(6):249–255, 2000.

[26] Y Wang and KH Low. Damped response analysis of nonlinear cushion systems by a linearization method. *Computers & Structures*, 83(19):1584–1594, 2005.

[27] NJ Mills and Y Masso-Moreu. Finite element analysis (FEA) applied to polyethylene foam cushions in package drop tests. *Packaging Technology and Science: An International Journal*, 18(1):29–38, 2005.

[28] UE Ozturk and G Anlas. Finite element analysis of expanded polystyrene foam under multiple compressive loading and unloading. *Materials & Design*, 32(2):773–780, 2011.

[29] T Piatkowski and P Osowski. Modified method for dynamic stress-strain curve determination of closed-cell foams. *Packaging Technology and Science*, 29(6):337–349, 2016.

[30] Y Azizi, AK Bajaj, P Davies, and V Sundaram. Prediction and verification of the periodic response of a single-degree-of-freedom foam-mass system by using incremental harmonic balance. *Nonlinear Dynamics*, 82(4):1933–1951, 2015.

[31] Y Azizi, P Davies, and AK Bajaj. Identification of nonlinear viscoelastic models of flexible polyurethane foam from uniaxial compression data. *Journal of Engineering Materials and Technology*, 138(2):021008, 2016.

[32] RS Kshetrimayum. A brief intro to metamaterials. *IEEE potentials*, 23(5):44–46, 2004.

[33] HW Bixby. Development of a paperboard honeycomb decelerator for use with large platforms in aerial delivery systems. *WADC'TR*, pages 59–776, 1959.

[34] SD Papka and S Kyriakides. In-plane biaxial crushing of honeycombs—: Part ii: Analysis. *International Journal of Solids and Structures*, 36(29):4397–4423, 1999.

[35] SRG Bates, IR Farrow, and RS Trask. 3d printed polyurethane honeycombs for repeated tailored energy absorption. *Materials & Design*, 112:172–183, 2016.

[36] Y Chen, T Li, Z Jia, F Scarpa, CW Yao, and L Wang. 3d printed hierarchical honeycombs with shape integrity under large compressive deformations. *Materials & Design*, 137:226–234, 2018.

[37] FN Habib, P Iovenitti, SH Masood, and M Nikzad. Cell geometry effect on in-plane energy absorption of periodic honeycomb structures. *The International Journal of Advanced Manufacturing Technology*, 94(5-8):2369–2380, 2018.

[38] C Ge, L Priyadarshini, D Cormier, L Pan, and J Tuber. A preliminary study of cushion properties of a 3d printed thermoplastic polyurethane kelvin foam. *Packaging Technology and Science*, 31(5):361–368, 2018.

[39] EB Duoss, TH Weisgraber, K Hearon, C Zhu, W Small IV, TR Metz, JJ Vericella, HD Barth, JD Kuntz, RS Maxwell, et al. Three-dimensional printing of elastomeric, cellular architectures with negative stiffness. *Advanced Functional Materials*, 24(31):4905–4913, 2014.

[40] Y Song. *Optimizing Hyperdamping Materials for Enhancing Vibration Control and Shock Attenuation Properties*. PhD thesis, The Ohio State University, 2017.

[41] RL Harne, Y Song, and Q Dai. Trapping and attenuating broadband vibroacoustic energy with hyperdamping metamaterials. *Extreme Mechanics Letters*, 12:41–47, 2017.

[42] T Li, Y Chen, X Hu, Y Li, and L Wang. Exploiting negative poisson's ratio to design 3d-printed composites with enhanced mechanical properties. *Materials & Design*, 142:247–258, 2018.

[43] P Vuyk, S Cui, and RL Harne. Illuminating origins of impact energy dissipation in mechanical metamaterials. *Advanced Engineering Materials*, 20(5):1700828, 2018.

[44] K Bertoldi, MC Boyce, S Deschanel, SM Prange, and T Mullin. Mechanics of deformation-triggered pattern transformations and superelastic behavior in periodic elastomeric structures. *Journal of the Mechanics and Physics of Solids*, 56(8):2642–2668, 2008.

[45] JTB Overvelde and K Bertoldi. Relating pore shape to the non-linear response of periodic elastomeric structures. *Journal of the Mechanics and Physics of Solids*, 64:351–366, 2014.

[46] N Hu and R Burgueño. Buckling-induced smart applications: recent advances and trends. *Smart Materials and Structures*, 24(6):063001, 2015.

[47] S Shan, SH Kang, JR Raney, P Wang, L Fang, F Candido, JA Lewis, and K Bertoldi. Multistable architected materials for trapping elastic strain energy. *Advanced Materials*, 27(29):4296–4301, 2015.

[48] J Meaud and K Che. Tuning elastic wave propagation in multistable architected materials. *International Journal of Solids and Structures*, 122:69–80, 2017.

[49] K Bertoldi. Harnessing instabilities to design tunable architected cellular materials. *Annual Review of Materials Research*, 47:51–61, 2017.

[50] K Che, C Yuan, J Wu, H Jerry Qi, and J Meaud. Three-dimensional-printed multistable mechanical metamaterials with a deterministic deformation sequence. *Journal of Applied Mechanics*, 84(1), 2017.

[51] S Cui and RL Harne. Characterizing the nonlinear response of elastomeric material systems under critical point constraints. *International Journal of Solids and Structures*, 135:197–207, 2018.

[52] F Niu, LS Meng, WJ Wu, JG Sun, WH Su, G Meng, and ZS Rao. Recent advances in quasi-zero-stiffness vibration isolation systems. In *Applied Mechanics and Materials*, volume 397, pages 295–303. Trans Tech Publ, 2013.

[53] C Ge. Theory and practice of cushion curve: A supplementary discussion. *Packaging Technology and Science*, 32(4):185–197, 2019.

[54] BASF. Packing with styropor®. `http://starfoameps.com/cms/upload/documents/5c48d088c4b3c_documents.pdf`. Accessed: 2016-6-22.

[55] A Joodaky, GS Batt, and JM Gibert. Prediction of cushion curves of polymer foams using a nonlinear distributed parameter model. *Packaging Technology and Science*, 33(1):3–14, 2020.

[56] RD Mindlin. Dynamics of package cushioning. *Bell Labs Technical Journal*, 24(3):353–461, 1945.

[57] Y Masso-Moreu and NJ Mills. Impact compression of polystyrene foam pyramids. *International Journal of Impact Engineering*, 28:653–676, 2003.

[58] JM Gibert and GS Batt. Impact oscillator model for the prediction of dynamic cushion curves of open cell foams. *Packaging Technology and Science*, 28(3):227–239, 2015.

[59] RW Ogden. Large deformation isotropic elasticity–on the correlation of theory and experiment for incompressible rubberlike solids. *Proceedings of the Royal Society of London. A. Mathematical and Physical Sciences*, 326(1567):565–584, 1972.

[60] HT Banks, NG Medhin, and GA Pinter. Multiscale considerations in modeling of nonlinear elastomers. *International Journal for Computational Methods in Engineering Science and Mechanics*, 8(2):53–62, 2007.

[61] RW Widdle, AK Bajaj, and P Davies. Measurement of the poisson's ratio of flexible polyurethane foam and its influence on a uniaxial compression model. *International Journal of Engineering Science*, 46:31–49, 2008.

[62] SK Maiti, LJ Gibson, and MF Ashby. Deformation and energy absorption diagram for cellular solids. *Acta Metallurgica*, 32(11):1963–1975, 1984.

[63] GS Batt, JM Gibert, and M Daqaq. Small strain vibration of a continuous, linearized viscoelastic rod of expanded polymer cushion material. *Journal of Sound and Vibration*, 349:330–347, 2015.

[64] GS Batt, JM Gibert, and M Daqaq. Reduced-order modeling of the linear vibration response of expanded polymer cushion material. *Packaging Technology and Science*, 28(1):59–74, 2015.

[65] GS Batt, JM Gibert, and M Daqaq. Primary resonance behaviour of a nonlinear, viscoelastic model of expanded polymer cushion material. *Packaging Technology and Science*, 28(8):694–709, 2015.

[66] K Paulin, G Batt, and M Daum. Statistical analysis of the stress-energy methodology applied to cushion curve determination. *Journal of Testing and Evaluation*, 41(3):409–416, 2013.

[67] C El-Helou and RL Harne. Exploiting functionally graded elastomeric materials to program collapse and mechanical properties. *Advanced Engineering Materials*, 21(12):1900807, 2019.

[68] ASTM. D395-18: Standard test methods for rubber property compression set. In *Annual Book of ASTM Standards*. ASTM International, West Conshohocken, Pa., 2018.

[69] RS Rivlin and DW Saunders. Large elastic deformations of isotropic materials vii. experiments on the deformation of rubber. *Philosophical Transactions of the Royal Society of London. Series A, Mathematical and Physical Sciences*, 243(865):251–288, 1951.

[70] M Gregory. *Elastic Instability: Analysis of Buckling Modes and Loads of Framed Structures*. E. and F. N. Spon Ltd, 1967.

[71] SH Kang, S Shan, A Košmrlj, WL Noorduin, S Shian, JC Weaver, DR Clarke, and K Bertoldi. Complex ordered patterns in mechanical instability induced geometrically frustrated triangular cellular structures. *Physical Review Letters*, 112(9):098701, 2014.

[72] MC Rice, EM Arruda, and MD Thouless. The use of visco-elastic materials for the design of helmets and packaging. *Journal of the Mechanics and Physics of Solids*, page 103966, 2020.

[73] DDL Chung. Self-sensing structural composites in aerospace engineering. In *Advanced Composite Materials for Aerospace Engineering*, pages 295–331. Elsevier, 2016.

[74] H. Tao and J. Gibert. Multifunctional mechanical metamaterials with embedded triboelectric nanogenerators. *Advanced Functional Materials*, page 2001720, 2020.

APPENDICES

A DERIVATION OF ORTHONORMALITY CONDITION AND NORMALIZATION OF THE MODE SHAPES

The orthogonality conditions can be derived by considering the undamped vibrations of Eqn. (2.14), where only the linear terms are retained

$$\frac{\partial^2 \hat{u}}{\partial t^2} = c_{eff}^2 \frac{\partial^2 \hat{u}}{\partial x^2}, \tag{I.1}$$

with the associated initial conditions

$$\hat{u}(x,0) = 0 \quad \text{and} \quad \frac{\partial \hat{u}}{\partial t}(x,0) = \sqrt{2gH}, \tag{I.2}$$

and boundary conditions

$$\hat{u}(L,t) = 0 \quad \text{and} \quad \frac{\sigma_s}{E_{1,eff}\, g} \frac{\partial^2 \hat{u}}{\partial t^2}\bigg|_{x=0} = \frac{\partial \hat{u}}{\partial x}\bigg|_{x=0}. \tag{I.3}$$

Assume a solution in the form

$$\hat{u}(x,t) = \sum_{n=1}^{\infty} \hat{U}_n(x) q_n(t), \tag{I.4}$$

where $\hat{U}_n(x)$'s are the mode shapes and $q_n(t)$'s are the temporal coordinates

$$\hat{U}_n(x)\ddot{q}_n(t) = c_{eff}^2 \hat{U}_n''(x) q_n(t). \tag{I.5}$$

Dividing both sides of Eqn. (I.5) by $q_n(t)$ yielding

$$\frac{\ddot{q}_n(t)}{q_n(t)} = c_{eff}^2 \frac{\hat{U}_n''(x)}{\hat{U}_n(x)} = -\omega_n^2, \tag{I.6}$$

or

$$\ddot{q}_n(t) - \omega_n^2 q_n(t) = 0, \quad \text{and} \tag{I.7}$$

$$\hat{U}_n''(x) + \bar{\beta}_n^2 \hat{U}_n(x) = 0, \quad \text{where} \quad \bar{\beta}_n = \frac{\omega_n}{c_{eff}}. \tag{I.8}$$

Multiplying both sides of Eq. (I.8) by $\hat{U}_m(x)$ and integrating over the length of the beam yields

$$c_{eff}^2 \int_0^L \hat{U}_n''(x)\hat{U}_m(x)\,dx = -\omega_n^2 \int_0^L \hat{U}_n(x)\hat{U}_m(x)\,dx. \tag{I.9}$$

Integrating by parts yields

$$-\omega_n^2 \int_0^L \hat{U}_n(x)\hat{U}_m(x)\,dx = -c_{eff}^2 \int_0^L \hat{U}_n'(x)\hat{U}_m'(x)\,dx + c_{eff}^2\, \hat{U}_n(x)\hat{U}_m'(x)\Big|_0^L. \tag{I.10}$$

Plugging the modal decomposition, Eq. (I.4) into the boundary conditions of Eq. (I.3) and into Eq. (I.10) yields

$$\omega_n^2 \left(\int_0^L \hat{U}_n(x)\hat{U}_m(x)\,dx + \frac{L}{\beta}\hat{U}_n(0)\hat{U}_m(0) \right) = c_{eff}^2 \int_0^L \hat{U}_n'(x)\hat{U}_m'(x)\,dx \tag{I.11}$$

where $\beta = \rho g L/\sigma_s$, this can also be written as

$$\omega_m^2 \left(\int_0^L \hat{U}_m(x)\hat{U}_n(x)\,dx + \frac{L}{\beta}\hat{U}_m(0)\hat{U}_n(0) \right) = c_{eff}^2 \int_0^L \hat{U}_m'(x)\hat{U}_n'(x)\,dx, \tag{I.12}$$

if the expansion is written as $\hat{u}(x,t) = \sum_{m=1}^{\infty} \hat{U}_m(x)q_m(t)$. Subtracting

$$\left(\omega_m^2 - \omega_n^2\right) \left(\int_0^L \hat{U}_m(x)\hat{U}_n(x)\,dx + \frac{L}{\beta}\hat{U}_m(0)\hat{U}_n(0) \right) = 0, \tag{I.13}$$

and since $\omega_n \neq \omega_m$, yields the following

$$\int_0^L \hat{U}_m(x)\hat{U}_n(x)\,dx + \frac{L}{\beta}\hat{U}_m(0)\hat{U}_n(0) = \delta_{mn}, \tag{I.14}$$

where δ_{mn} is the Kronecker delta. Equation (I.14) gives the orthonormality condition and the normalization fo the mode shape $\hat{U}_n(x)$.

B COEFFICIENT OF THE SINGLE MODE APPROXIMATION OF FOAM'S IMPACT MODEL

The coefficients for the single mode approximation can be written as

$$
\begin{aligned}
\bar{c}_{11} &= \frac{C_D}{\rho}\left(U_1(0)\hat{U}_1'(0) - \int_0^L \hat{U}_1(x)\hat{U}_1'(x)\,dx\right),\\
\zeta_1 &= \frac{\bar{c}_{11}}{2\omega_1},\\
\bar{\alpha}_{12} &= c^2\left(2E_2 + 6\epsilon_s E_3 + 12\epsilon_s^2 E_4 + 20\epsilon_s^3 E_5 + 30\epsilon_s^4 E_6 + 42\epsilon_s^5 E_7\right)\\
&\quad\left(\frac{1}{2}\hat{U}_1(0)\hat{U}_1'(0)^2 - \int_0^L \hat{U}_1(x)\hat{U}_1'(x)\hat{U}_1''(x)\,dx\right),\\
\bar{\alpha}_{13} &= c^2\left(3E_3 + 12\epsilon_s E_4 + 30\epsilon_s^2 E_5 + 60\epsilon_s^3 E_6 + 105\epsilon_s^4 E_7\right)\\
&\quad\left(\frac{1}{3}\hat{U}_1(0)\hat{U}_1'(0)^3 - \int_0^L \hat{U}_1(x)\hat{U}_1'(x)^2\hat{U}_1''(x)\,dx\right),\\
\bar{\alpha}_{14} &= c^2\left(4E_4 + 20\epsilon_s E_5 + 60\epsilon_s^2 E_6 + 140\epsilon_s^3 E_7\right)\left(\frac{1}{4}\hat{U}_1(0)\hat{U}_1'(0)^4 - \int_0^L \hat{U}_1(x)\hat{U}_1'(x)^3\hat{U}_1''(x)\,dx\right),\\
\bar{\alpha}_{15} &= c^2\left(5E_5 + 30\epsilon_s E_6 + 105\epsilon_s^2 E_7\right)\left(\frac{1}{5}\hat{U}_1(0)\hat{U}_1'(0)^5 - \int_0^L \hat{U}_1(x)\hat{U}_1'(x)^4\hat{U}_1''(x)\,dx\right),\\
\bar{\alpha}_{16} &= c^2\left(6E_6 + 42\epsilon_s E_7\right)\left(\frac{1}{6}\hat{U}_1(0)\hat{U}_1'(0)^6 - \int_0^L \hat{U}_1(x)\hat{U}_1'(x)^5\hat{U}_1''(x)\,dx\right),\\
\bar{\alpha}_{17} &= c^2\left(7E_7\right)\left(\frac{1}{7}\hat{U}_1(0)\hat{U}_1'(0)^7 - \int_0^L \hat{U}_1(x)\hat{U}_1'(x)^6\hat{U}_1''(x)\,dx\right).
\end{aligned}
$$

C POLYNOMIAL MODEL FOR HYPERELASTICITY

The strain energy density for the Polynomial model can be written as

$$W = \sum_{i,j=0}^{N} C_{ij}(I_1 - 3)^i (I_2 - 3)^j, \tag{I.15}$$

where C_{ij} are the material constants. I_1 and I_2 are the first and second strain invariants and can be written as

$$I_1 = \lambda_1^2 + \lambda_3^2 + \lambda_3^2, \tag{I.16}$$

$$I_2 = \lambda_1^2\lambda_2^2 + \lambda_2^2\lambda_3^2 + \lambda_3^2\lambda_1^2, \tag{I.17}$$

where λ_1, λ_2, and λ_3 are the stretch ratios in the principle directions. Assuming the material is incompressible, $\lambda_1\lambda_2\lambda_3 = 1$. Now noting that the loading is uniaxial leads to the following relationship between stretch ratios

$$\lambda_2 = \lambda_3 = \frac{1}{\sqrt{\lambda_1}}, \tag{I.18}$$

The stretch ratio in the compression direction is defined as $\lambda_1 = 1 + x_1/L_o$. The nominal stress in the compression direction can be written as

$$\sigma_1 = \lambda_1 \frac{\partial W}{\partial \lambda_1}. \tag{I.19}$$

The initial shear modulus of the material is given by

$$\mu_0 = 2(C_{10} + C_{01}), \tag{I.20}$$

assuming the material is incompressible, i.e. $\nu = 0.5$, then the initial Young's modulus is given by

$$E_0 = 2\mu(1 + \nu). \tag{I.21}$$

The error between the nonlinear stress and the linear approximation can be seen in Figure I.1. As expected the error increases monotonically as the compressive strain

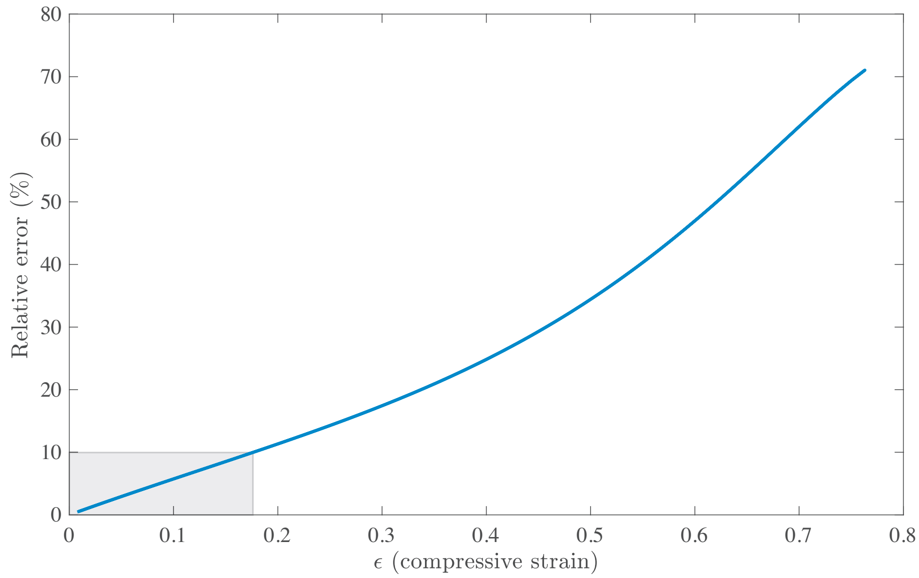

Figure I.1. Relative error between $\sigma_1 = \lambda_1 \frac{\partial W}{\partial \lambda_1}$ and $E_0\epsilon$. Shaded region indicates area where the relative error is within 10%

increases; the error is under 10% for strains under 0.18.

C.1 MATHEMATICA CODE FOR HYPERELASTIC CURVE FITTING

This appendix contains a detailed discussion of the numerical implementation for the hyperelastic curve fit. The program for the curve fit was written using the Mathematica technical computing system. The comments to the workbook are structured to provide the reader with an explanation of the relevant output.

```
Clear["Global`*"]
dir = "/Users/Dropbox/Amin/X_and_other/X_Codes_and_Data";
SetDirectory[dir];

FileNames[];

(*Set Geometry/ units are mm*)
th = 0.013; (*thickness*)
di = 0.029;  (*diameter*)
AREA = Pi/4*di^2;(*area calculation*)
(*Read in .mat data*)

Data = Import["Cylinder_Sili_with_SteelSupport_rate10.mat"];

(*Seperate time, strain,stress, raw voltage, and units*)

DataTime   = Flatten[Data[[1]]];
DataStrain = Flatten[Data[[2]]]/th/1000;
DataStress = Flatten[Data[[3]]]/AREA;
DataElec    = Flatten[Data[[4]]];
DataUnit     = Data[[5]]
NRaw         = Length[DataTime]/2
```

```
(*Determine maximum strain*)
DataMax = DataStrain[[NRaw]]

RespTable =
  Table[{-DataStrain[[nn + 1]], -DataStress[[nn + 1]]}, {nn, 1,
    NRaw - 1 }];
ListPlot[RespTable, Frame -> True,
 FrameLabel -> {"\[Epsilon]", "\[Sigma]"} Frame -> True]

(*Average out to smooth data*)
RespTableM = MovingMap[Mean, RespTable, 4];

NM = Length[RespTableM];
RespTableMM = Table[RespTableM[[i]] - RespTableM[[NM]], {i, 1, NM}];

UniRules = {\[Lambda]1 -> \[Lambda], \[Lambda]2 ->
   1/Sqrt[\[Lambda]], \[Lambda]3 -> 1/Sqrt[\[Lambda]]}

(*Strain Energy Density Function*)

Upoly = C10*(I1 - 3)^1*(I2 - 3)^0 +
              C20*(I1 - 3)^2*(I2 - 3)^0 +
              C01*(I1 - 3)^0*(I2 - 3)^1 +
              C02*(I1 - 3)^0*(I2 - 3)^2 +
              C11*(I1 - 3)^1*(I2 - 3)^1;

(* Invarients in terms of strestch ratios*)PolyRules = {I1 -> \
\[Lambda]1^2 + \[Lambda]2^2 + \[Lambda]3^2,
  I2 -> \[Lambda]1^2*\[Lambda]2^2 + \[Lambda]2^2*\[Lambda]3^2 + \
```

```
\[Lambda]3^2*\[Lambda]1^2}

Upoly1 = Upoly /. PolyRules /. UniRules

(*Stress from  Energy Density Function)
T11 = FullSimplify[Expand[\[Lambda]*D[Upoly1, \[Lambda]]]]
(*Write stress in term of infinitesimalstrain*)
T11e = T11 /. \[Lambda] -> (1 + x)

(*Polynomial Fit*)

PolyFit1    =
  FindFit[RespTableMM, T11e, {C10, C20, C11, C01, C02}, x,
   MaxIterations -> \[Infinity], WorkingPrecision -> 4];
(*Convert fit to model*)

PolyModelFunction1 = Function[{x}, Evaluate[T11e /. PolyFit1]];
(*Convert to expression to plot*)
PlotM1 = {PolyModelFunction1[x]};

(*Shear and Young's Modulus)
Mu = 2*(C01 + C10) /. PolyFit1;
Em = 2*Mu*(1 + .5);

(*Plot the original data and curve fit*)
FitPlot =
 Plot[{PlotM1}, {x, .2, -.8},
  Epilog -> {PointSize[Medium], Map[Point, RespTableMM]},
  PlotStyle -> Directive[Red], Frame -> True,
```

```
FrameLabel -> {"\[Epsilon]", "\[Sigma]"},
LabelStyle ->
 Directive[Black, FontFamily -> "Times", FontSize -> 12],
ImageSize -> 450]
```

D MANUFACTURING PROCESS OF EXTENDEDχ STRUCTURES

This appendix details the manufacturing of the χ structure. The process begins by determining desired dimensions for the extended χ. Then a negative mold is created in a CAD software, e.g. Solidworks. The mold is manufactured by a 3D printer. Figure I.2 shows the mold in gray color. Next a two agent silicon rubber is mixed equally and poured into the mold. The silicon rubber is shown with green color. After a determined curing time, the extended χ structure is pulled out from the mold as it is shown in the Fig. I.2.

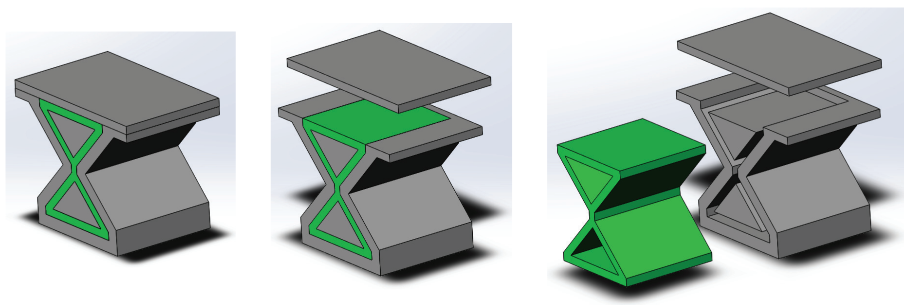

Figure I.2. The schematic extended χ during solidification and demolding

E MATLAB IMPLEMENTATION OF BUCKLING ANALYSIS

This appendix details the numerical implementation of the buckling model presented in Chapter 4.

```
clc
clear
close all
% This the no sway solution
FS = 14; % Font Size
fprintf(['\n\n\nStarting file >>' mfilename '<< at ' datestr(
    now,0) '\n\n']);
format long
close all

nel = 7; % Number of Members
nen = 2; % Number of Nodes

d         = 0.02;
thetadeg  = 36.0;
theta     = thetadeg*pi/180.0;
L         = 0.0123605131;  %Lac       d/(2*cos(theta));
alpha     = 0.007469716/L; %0.008/L;%d/L-2*sin(theta);
b         = 0.020;
h         = 0.0022;

Lcell = 2*L*cos(theta);
Hcell = 2*L*sin(theta)+alpha*L;

% Geometric Parameters
```

```
Im          = 1/12*b*h^3; % Moment of Inertia
Emod        = 432200; %Mpa
EI          = Emod*Im; %Flexural Stiffness

%Nodal Coordinates
x1 = 0;
y1 = 0;
x2 = 2*L*cos(theta);
y2 = 0;
x3 = L*cos(theta);
y3 = L*sin(theta);
x4 = x3;
y4 = y3 + alpha*L;
x5 = x1;
y5 = y4+L*sin(theta);
x6 = x2;
y6 = y5;

%coordinates
coord = [x1 x2 x3 x4 x5 x6; y1 y2 y3 y4 y5 y6];
%connectivity
le = [ 1 2; 1 3; 2 3; 3 4;  4 5  ;  4 6; 5 6]';
%plot shapes
DefPlot=figure;
for e = 1:nel
    line(coord(1,le(:,e)),coord(2,le(:,e)), 'Linestyle','-',
        'color',[0.65 0.65 0.65],'Linewidth',4)
end
```

```
line(coord(1,:),coord(2,:), 'Linestyle','none', 'Marker','o',
    'MarkerSize', 8,  'MarkerEdgeColor' , 'k' , '
    MarkerFaceColor' , 'r')
hold on
axis square
axis off

% Plot of phi1 and phi2 functions
num        = 2*10^6; %2
NNN        = 3*pi;
LambdaV1 = linspace(0.01, NNN, num); %3,5,
LambdaV2 = linspace(NNN, 2*NNN, num);
LambdaV   = [LambdaV1 LambdaV2];
num        = 2*num;

for i = 1:num
    Lambda = LambdaV(i);
    [DetM, DetM1, DetM2, Theta] = characteristic_eqn(Lambda,
        theta, alpha, L);
    CE2(i) = DetM2;
    CE1(i) = DetM1;
    CE(i)  = DetM;
end

[Val2 loc2] = find(abs(diff(sign(CE2)))==2);
[Val1 loc1] = find(abs(diff(sign(CE1)))==2);

figure
```

```
line(LambdaV,CE1, 'linestyle','-','Marker','none','linewidth',1,'color','k')
line(LambdaV, zeros(size(LambdaV)),'linewidth',3,'color','r')
P1 = line(LambdaV(loc1),zeros(size(loc1)),'marker','o');
set(P1, 'Marker','o', 'Linestyle','-', 'Color','k','MarkerSize', 8, 'MarkerEdgeColor' , 'k' , 'MarkerFaceColor' , [.65 .65 1] );
ylabel('$\phi_1(\lambda)$', 'Interpreter','latex','FontSize', FS);
xlabel({' $\lambda$';'(a)'}, 'Interpreter','latex','FontSize', FS);
set( gca , 'FontName' , 'Times', 'FontSize', FS );
box on
axis([4 NNN -200 200])
axis square

figure
line(LambdaV,CE2,'linestyle','-','Marker','none','linewidth',1,'color','k')
line(LambdaV, zeros(size(LambdaV)),'linewidth',3,'color','r')
P2 = line(LambdaV(loc2),zeros(size(loc2)),'marker','o');
set(P2, 'Marker','o', 'Linestyle','-', 'Color','k','MarkerSize', 8, 'MarkerEdgeColor' , 'k' , 'MarkerFaceColor' , [.65 .65 1] );
ylabel('$\phi_2(\lambda)$', 'Interpreter','latex','FontSize', FS);
xlabel({' $\lambda$';'(b)'}, 'Interpreter','latex','FontSize', FS);
set( gca , 'FontName' , 'Times', 'FontSize', FS );
```

```
box on
axis([4 NNN -200 200])
axis square

% Initial Conditions
Lambda_CE1_IG = LambdaV(loc1);
Lambda_CE2_IG = LambdaV(loc2);

% Choose Modes 1 for AS, 0 for SM
MODE = 0;
ROOT = 2;
if MODE == 0 % Symmetric Modes
      CEsolve = 0;
      Lambda0 = Lambda_CE1_IG(ROOT);
else % Anit-symmetric Modes
      CEsolve = 1;
      Lambda0 = Lambda_CE2_IG(ROOT);
end
%Run Optimization
Lambda   = fzero(@(Lambda)objfunc(Lambda,theta, alpha, L,
    CEsolve), Lambda0);

%Check for Spurious Mode
[DetM, DetM1, DetM2, M, Theta, RankM] = characteristic_eqn(
    Lambda, theta, alpha, L)
while RankM==6
      RankM
      Lambda0
      Mode
```

```
        fprintf('Spurious Mode Detected \n')
        ROOT = ROOT +1; %Move to next root
        if MODE == 0 % Symmetric Modes
            CEsolve = 0;
            Lambda0 = Lambda_CE1_IG(ROOT);
        else % Anit-symmetric Modes
            CEsolve = 1;
            Lambda0 = Lambda_CE2_IG(ROOT);
        end
        % Run Optimization again and check
        Lambda  = fzero(@(Lambda)objfunc(Lambda,theta, alpha, L,
            CEsolve), Lambda0);
       [DetM, DetM1, DetM2, M, Theta, RankM] = characteristic_eqn
           (Lambda, theta, alpha, L);


end
fprintf('True mode detected\n')
fprintf('The optimal lambda %11.4e. \n', Lambda)

%%
% Post Processing
% Wave Number
k    = Lambda/L;
kac = k; %(compression)
kbc = k; %(compression)
kab = sqrt(cot(theta)/csc(theta))*k; %(tension)
kcd = sqrt(2/csc(theta))*k; %(compression)
kde = k; %(compression)
```

```
kdf = k; %(compression)
kef = sqrt(cot(theta)/csc(theta))*k; %(tension)

%Geometry
Lac = L;
Lbc = L;
Lab = 2*L*cos(theta);
Lcd = alpha*L;
Lde = L;
Ldf = L;
Lef = 2*L*cos(theta);

fprintf('The optimal k is %11.4e. \n', k)

[DetM, DetM1, DetM2, M, Theta, RankM] = characteristic_eqn(
    Lambda, theta, alpha, L);

%Normalized Buckling Mode
Theta  = Theta/norm(Theta);
ThetaA = Theta(1);
ThetaB = Theta(2);
ThetaC = Theta(3);
ThetaD = Theta(4);
ThetaE = Theta(5);
ThetaF = Theta(6);

fprintf('The Rank of M is %11.1e. \n', RankM)

[MAB, MBA] = moment_tens(kab, Lab, ThetaA, ThetaB, EI);
```

```
[MAC, MCA] = moment_comp(kac, Lac, ThetaA, ThetaC, EI);
[MBC, MCB] = moment_comp(kbc, Lbc, ThetaB, ThetaC, EI);
[MCD, MDC] = moment_comp(kcd, Lcd, ThetaC, ThetaD, EI);
[MDE, MED] = moment_comp(kde, Lde, ThetaD, ThetaE, EI);
[MDF, MFD] = moment_comp(kdf, Ldf, ThetaD, ThetaF, EI);
[MEF, MFE] = moment_tens(kef, Lef, ThetaE, ThetaF, EI);

% Check Equilibrium
Node_A = MAB + MAC;
Node_B = MBA + MBC;
Node_C = MCA + MCB + MCD;
Node_D = MDC + MDE + MDF;
Node_E = MED + MEF;
Node_F = MFD + MFE;

% Recover Compressive Force
Pab    = kab^2*EI;
Pac    = kac^2*EI;
Pbc    = kbc^2*EI;
Pcd    = kcd^2*EI;
Pde    = kde^2*EI;
Pdf    = kdf^2*EI;
Pef    = kef^2*EI;

% Check  Equilibrium !
f1       = Pcd/2;
f2       = Pab/cot(theta);
f3       = Pac/csc(theta);
% Critical Load
```

```
Fc1     = 2*f1;
Fc2     = 2*f2;
Fc3     = 2*f3;
% Buckling Eigenvalue from Abaqus
BucklingLambda = sqrt(Fc1/(Emod*Im));

fprintf('......................... \n');
fprintf('The height and width are %11.4e. x %11.4e.  \n',
    Hcell, Lcell)
fprintf('......................... \n');
fprintf('Equilibrium analysis..... \n');
fprintf('The critical force from 3 calculations %11.4e. %11.4
    e. %11.4e. \n', Fc1, Fc2, Fc3)
fprintf('......................... \n');
fprintf('The buckling eigenvalue %11.4e. \n', BucklingLambda)
fprintf('......................... \n');

numd        = 100;
[wab, xab] = deformation_tens(kab, Lab, MAB, MBA, Pab, numd);
[wac, xac] = deformation_comp(kac, Lac, MAC, MCA, Pac, numd);
[wbc, xbc] = deformation_comp(kbc, Lbc, MBC, MCB, Pbc, numd);
[wcd, xcd] = deformation_comp(kcd, Lcd, MCD, MDC, Pcd, numd);
[wde, xde] = deformation_comp(kde, Lde, MDE, MED, Pde, numd);
[wdf, xdf] = deformation_comp(kdf, Ldf, MDF, MFD, Pdf, numd);
[wef, xef] = deformation_tens(kef, Lef, MEF, MFE, Pef, numd);

% Degeneracy Test
[sac, cac] = flexibilitycomp(kac, Lac);
[sab, cab] = flexibilitytens(kab, Lab);
```

```
[scd, ccd] = flexibilitycomp(kcd, Lcd);

%DG1 = cos(theta)
%DG2 = (sab*(cab-1))/(2*sac)

% Rearrange
wef = wef;
wed = fliplr(wde);
wfd = fliplr(wdf);
wdc = fliplr(wcd);
wca = fliplr(wac);
wcb = fliplr(wbc);
wab = wab;

xef = xef;
xed = fliplr(xde);
xfd = fliplr(xdf);
xdc = fliplr(xcd);
xca = fliplr(xac);
xcb = fliplr(xbc);
xab = xab;

def_x = [xef;xed;xfd;xdc;xca;xcb;xab];
def_y = [wef;wed;wfd;wdc;wca;wcb;wab];

%Plot individual deformations
figure
subplot(7,2,1)
line(xab,wab,'linewidth',2)
```

```
axis tight
axis off
title('w_{ab}')
subplot(7,2,3)
line(xac,wac,'linewidth',2)
axis tight
axis off
title('w_{ac}')
subplot(7,2,5)
line(xbc,wbc,'linewidth',2)
axis tight
axis off
title('w_{bc}')
subplot(7,2,7)
line(xcd,wcd,'linewidth',2)
axis tight
axis off
title('w_{cd}')
subplot(7,2,9)
line(xde,wde,'linewidth',2)
axis tight
axis off
title('w_{de}')
subplot(7,2,11)
line(xdf,wdf,'linewidth',2)
axis tight
axis off
title(['w_{df}'])
subplot(7,2,13)
```

```
line(xef,wef,'linewidth',2)
axis tight
axis off
title('w_{ef}')


% Plot the Deformed Shape
figure(DefPlot)
for e = 1:nel
    coord_local = coord(:,le(:,e));
    [angle, T]  = getangle(coord_local);
    Dof         = [def_x(e,:); def_y(e,:)];
    Dof         = T*Dof;
    line(coord_local(1,1)+Dof(1,:), coord_local(2,1)+Dof(2,:)
        , 'linewidth', 2, 'color', 'k')
end
axis tight
title(['\lambda = ', num2str(Lambda), ', \alpha = ',num2str(
    alpha), ', \theta = ',num2str(thetadeg), char(176), ', F_{
    crit} = ', num2str(Fc1) ' N'
    ])

%% No Sway Characteristic Equation
function [DetM, DetM1, DetM2, M, Theta, RankM] =
    characteristic_eqn(Lambda, theta, alpha, L)
% Geometric Properties
Lac = L;
Lbc = L;
Lab = 2*L*cos(theta);
```

```
Lcd = alpha*L;
Lde = L;
Ldf = L;
Lef = 2*L*cos(theta);

k   = Lambda/L;
kac = k; %(compression)
kbc = k; %(compression)
kab = sqrt(cot(theta)/csc(theta))*k; %(tension)
kcd = sqrt(2/csc(theta))*k; %(compression)
kde = k; %(compression)
kdf = k; %(compression)
kef = sqrt(cot(theta)/csc(theta))*k; %(tension)

[sac, cac] = flexibilitycomp(kac, Lac);
[sbc, cbc] = flexibilitycomp(kbc, Lbc);
[sab, cab] = flexibilitytens(kab, Lab);
[scd, ccd] = flexibilitycomp(kcd, Lcd);
[sde, cde] = flexibilitycomp(kde, Lde);
[sdf, cdf] = flexibilitycomp(kdf, Ldf);
[sef, cef] = flexibilitytens(kef, Lef);

M      = zeros(6,6);
M(1,1) = sab/Lab + sac/Lac;
M(1,2) = cab*sab/Lab;
M(1,3) = cac*sac/Lac;
M(2,1) = M(1,2);
M(2,2) = sab/Lab + sbc/Lbc;
M(2,3) = cbc*sbc/Lbc;
```

```
M(3,1) = M(1,3);
M(3,2) = M(2,3);
M(3,3) = sac/Lac + sbc/Lbc + scd/Lcd;
M(3,4) = ccd*scd/Lcd;
M(4,3) = M(3,4);
M(4,4) = scd/Lcd + sde/Lde + sdf/Ldf;
M(4,5) = cde*sde/Lde;
M(4,6) = cdf*sdf/Ldf;
M(5,4) = M(4,5);
M(5,5) = sde/Lde + sef/Lef;
M(5,6) = cef*sef/Lef;
M(6,4) = M(4,6);
M(6,5) = M(5,6);
M(6,6) = sdf/Ldf + sef/Lef;

DetM  =  det(M)*L^6;
DetM1 = (sab-cab*sab+2*sac*cos(theta));% should be squared
DetM2 = (-(1 + cab)^2*sab^2*((-1 + ccd)*scd - 2*sac*alpha)*(
    scd + ccd*scd + 2*sac*alpha) - ...
           2*sac^2*((1 + ccd)*scd - 2*(-1 + cac^2)*sac*alpha)
               *((-1 + ccd)*scd + ...
           2*(-1 + cac^2)*sac*alpha) - ...
           4*(1 + cab)*sab*sac*((-1 + ccd^2)*scd^2 + ...
           2*(-2 + cac^2)*sac*scd*alpha + ...
           4*(-1 + cac^2)*sac^2*alpha^2)*cos(theta) - ...
           2*sac^2*((1 + ccd)*scd - ...
           2*(-1 + cac^2)*sac*alpha)*((-1 + ccd)*scd +  ...
           2*(-1 + cac^2)*sac*alpha)*cos(2*theta))*sec(theta)
               ^4;
```

```
RankM = rank(M);

 if RankM == 5 %one free angle
      Theta  = [-1 0 0 0 0 0]';
      BucklingForce  = M*Theta;
      Theta(2:6)      = M(2:6,2:6)\-BucklingForce(2:6);
 elseif RankM == 4% two free angles
      Theta = [ 1 0 0 0 0 1]';
      BucklingForce  = M*Theta;
      Theta(2:5)      = M(2:5,2:5)\-BucklingForce(2:5);
%       DG1 = cos(theta)
%       DG2 = (sab*(cab-1))/(2*sac)
%       keyboard
 elseif RankM == 6 %only the trivial solutions exist
      Theta  = [ 0 0 0 0 0 0]';
 end


end

% Flexibility Constants Compression
function [s, c] = flexibilitycomp(k, L)
lambda = k*L;
s       = lambda*(sin(lambda)-lambda*cos(lambda))/(2-2*cos(
    lambda)-lambda*sin(lambda));
c       = (lambda - sin(lambda))/(sin(lambda)-lambda*cos(
    lambda));
end
```

```
% Flexibility Constants Tension
function [s, c] = flexibilitytens(k, L)
lambda = k*L;
s      = lambda*(lambda*cosh(lambda)-sinh(lambda))/(2-2*cosh(
    lambda)+lambda*sinh(lambda));
c      = (sinh(lambda)-lambda)/(lambda*cosh(lambda)-sinh(
    lambda));
end
%
function [w, x] = deformation_comp(k, L, Ma, Mb, P, num)
x = linspace(0, L, num);
A = -Ma/P*cot(k*L) - Mb/P*csc(k*L);
B =  Ma/P;
w =  A*sin(k*x)+ B*cos(k*x) - Ma/P*(1 -x/L) + Mb/P*(x/L);
end
%
function [w,x] = deformation_tens(k, L, Ma, Mb, P, num)
% Deformation of tension for beam
x = linspace(0, L, num);
A = -Ma/P*coth(k*L) - Mb/P*csch(k*L);
B =  Ma/P;
w = A*sinh(k*x)+ B*cosh(k*x) - Ma/P*(1 -x/L) + Mb/P*(x/L);
end
%
function [Ma, Mb] = moment_comp(k, L, Theta_a, Theta_b, EI)
% Moment angle relationship for compression
[s, c] = flexibilitycomp(k, L);
Ma     = s*Theta_a   + s*c*Theta_b;
Mb     = s*c*Theta_a + s*Theta_b;
```

```
Ma       = Ma*EI/L;
Mb       = Mb*EI/L;
end
%
function [Ma, Mb] = moment_tens(k, L, Theta_a, Theta_b, EI)
% Moment angle relationship for tension
[s, c] = flexibilitytens(k, L);
Ma       = s*Theta_a   + s*c*Theta_b;
Mb       = s*c*Theta_a + s*Theta_b;
Ma       = Ma*EI/L;
Mb       = Mb*EI/L;
end
function [F] = objfunc(Lambda, theta, alpha, L, CESolve)
% Characteristic Poynomial
[DetM, DetM1, DetM2, M, Theta, RankM] = characteristic_eqn(
    Lambda, theta, alpha, L);

if CESolve == 0
    F = DetM1;
elseif CESolve == 1
    F = DetM2;
else
    F = DetM;
end

end

function [angle, T]= getangle(coord_local)
% Cooordinate  Generation
```

```
xcoord = coord_local(1,:);
ycoord = coord_local(2,:);
dx     = xcoord(1,2) - xcoord(1,1);
dy     = ycoord(1,2) - ycoord(1,1);
angle  = atan2(dy, dx);
c      = cos(angle);
s      = sin(angle);
T      = [c -s; s c];

end
```

F FEM MESH CONVERGENCE

This appendix provides the details of a mesh convergence study. The finite element analysis was performed in the ABAQUS analysis package. The structure was simulated in ABAQUS using a Dynamic-Implicit analysis with a CPS4R element with hyperelastic material behavior that is described by the polynomial strain energy functional. The material properties are directly imported from experimental stress-strain results. Using the imported data and hyperelastic model in Material module in ABAQUS, the coefficients are obtained automatically for polynomial type of hyperelasticity. The extended χ structure was seeded to have an element length of 0.1 mm/side, 0.5 mm/side, and 0.2 mm/side (Fig. I.3).

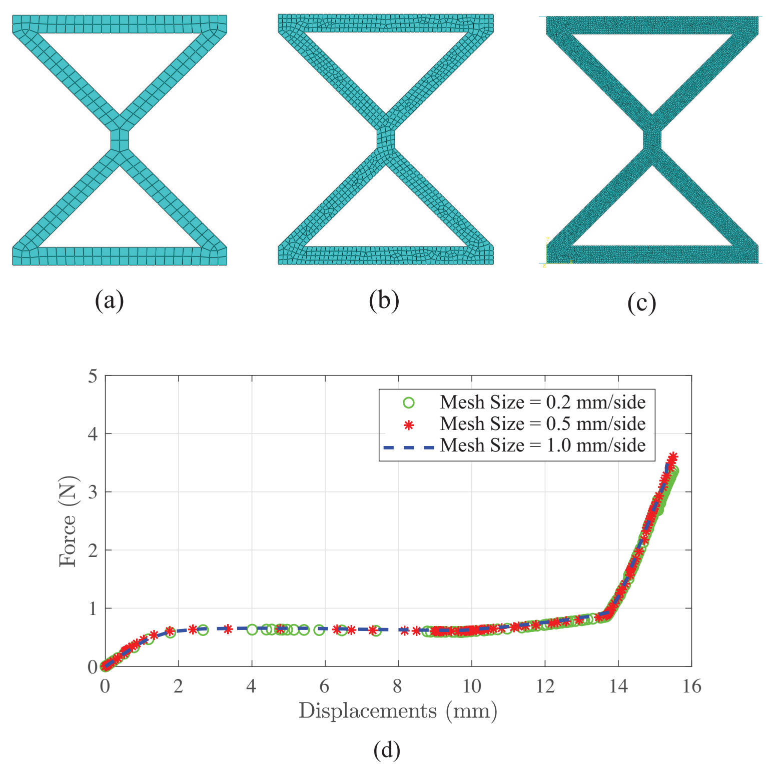

Figure I.3. Effect of mesh size on FEM results for the Extended χ (a) 1 mm/side, (b) 0.5 mm /side, and (c) 0.2 mm/side. The results from all three meshes are closely in agreement as shown in plot (d).

G FINITE ELEMENT MODE SHAPES OF EXTENDED χ STRUCTURE

This appendix contains the lowest four buckling mode shapes from ABAQUS. The results are obtained using a linear perturbation buckling analysis. The element is designated as a B21 wire beam, the modulus of elasticity (E) is 432.2 MPa , and a poisson's ratio (ν) of 0.49. The structure is constrained from translating on the bottom legs and the top legs is subject to points loads f on both ends. The buckling eigenvalue from ABAQUS is given as $\lambda_p = \sqrt{2f/(EI)}$.

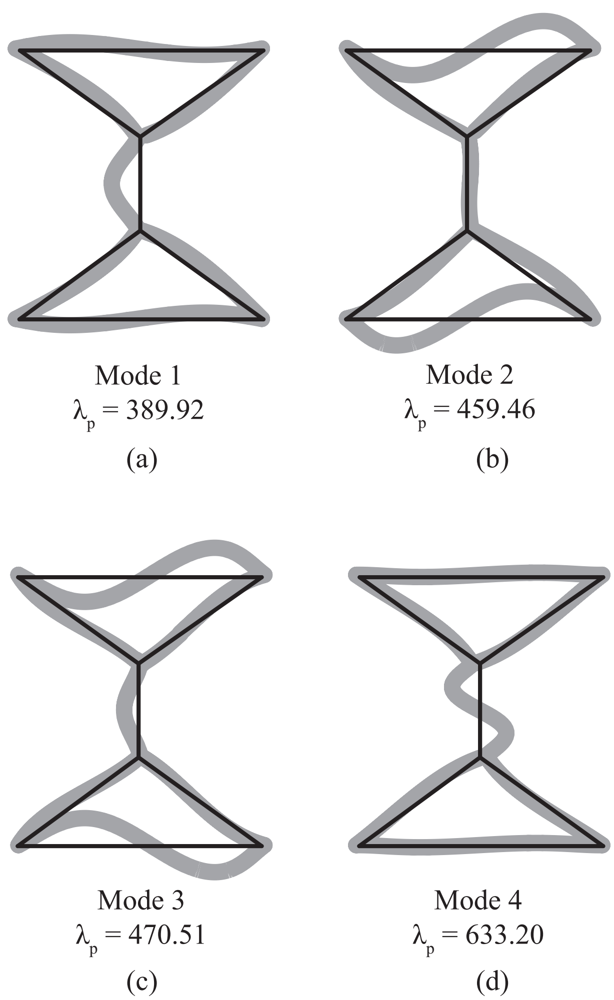

Figure I.4. Finite element buckling mode shapes: (a) mode 1, (b) mode 2, (c) mode 3, and (d) mode 4. The dark black lines indicate the undeformed shape and the grey lines indicate the buckling mode.